HARVARD UNIVERSITY
Graduate School of Arts and Sciences

DISSERTATION ACCEPTANCE CERTIFICATE

The undersigned, appointed by the

Committee on Higher Degrees in Biophysics

have examined a dissertation entitled

Microscopic Image Guidance: Real-time Thermal Therapy Monitoring for Epithelial Lesions

presented by **William Chun Yip Lo**

candidate for the degree of Doctor of Philosophy and hereby certify that it is worthy of acceptance.

Signature _____

Typed name: Prof. David A. Boas

Signature _____

Typed name: Prof. Conor L. Evans

Signature _____

Typed name: Prof. Norman S. Nishioka

Signature _____

Typed name: Prof. James M. Hogle

Date: December 21, 2016

Microscopic Image Guidance: Real-time Thermal Therapy Monitoring for Epithelial Lesions

A DISSERTATION PRESENTED
BY
William Chun Yip Lo
TO
The Committee on Higher Degrees in Biophysics

IN PARTIAL FULFILLMENT OF THE REQUIREMENTS
FOR THE DEGREE OF
Doctor of Philosophy
IN THE SUBJECT OF
Biophysics (Harvard-MIT Medical Engineering and Medical Physics)

Harvard University
Cambridge, Massachusetts
December 2016

Thesis advisors: Professors Brett E. Bouma & Benjamin J. Vakoc William Chun Yip Lo

Microscopic Image Guidance: Real-time Thermal Therapy Monitoring for Epithelial Lesions

Abstract

Conventional image guidance is typically based on *macroscopic* clinical imaging modalities, such as magnetic resonance imaging, computed tomography and ultrasound imaging, which are limited in their ability to guide therapeutic interventions for epithelial lesions due to constraints on spatial resolution. Here, the notion of *microscopic image guidance* is introduced. The overall goal of this dissertation is to develop a framework for real-time guidance and monitoring of thermal therapy in epithelial lesions that seamlessly integrates optical frequency domain imaging (OFDI), which is a high-resolution ($\sim$ 10 μm), volumetric diagnostic imaging tool now used clinically in Barrett's esophagus patients. The first part of this dissertation investigates an approach to integrate OFDI into the conventional endoscopy workflow using a machine learning scheme after enriching the endoscopic scene with navigational landmarks through a noninvasive *laser painting* paradigm. The second part discusses an integrated approach that combines imaging, radiofrequency ablation (RFA), and monitoring in a single OFDI-RFA balloon catheter configuration. A label-free, noninvasive technique to monitor the thermal coagulation process at high resolution, based on complex difference variance, is first presented in a thulium laser benchtop setup. With proper noise calibration and non-uniform rotation distortion artifact correction, the precise delineation of the thermal coagulation zone is demonstrated in porcine esophagus *ex vivo* using the integrated OFDI-RFA catheter, as validated by NBTC histology. The ability to directly and accurately visualize the thermal coagulation process at high resolution is critical to the precise delivery of thermal energy to epithelial lesions and opens up the possibility of performing microscopic image-guided procedures in a vast array of epithelial applications beyond Barrett's esophagus in the future.

Contents

Listing of figures

Acknowledgments

This PhD thesis has been a wonderful journey because of all the people I have met. I would like to begin by sincerely acknowledging my PhD advisors, Professors Brett Bouma and Benjamin Vakoc, for their mentorship and support throughout my entire PhD journey. When I started my first day at the Wellman Center for Photomedicine, I had little technical background in optical coherence tomography and Professors Brett Bouma and Benjamin Vakoc launched me into an angiography project that really sparked my interests in OCT and allowed me to see the beauty of OCT imaging. I am also extremely grateful for the friendship and mentorship from a number of individuals in the Bouma and Vakoc labs, especially Martin Villiger who I met since my first day at the Wellman Center and Néstor Uribe-Patarroyo who has been an incredible mentor throughout. Both Martin and Néstor have been very generous with their time. In particular, I would like to acknowledge Martin's spectral binning algorithm used in the reconstruction of the polarization-sensitive OFDI datasets and assistance with the thulium laser therapy setup. I was also very fortunate to be offered the opportunity to join a collaborative research effort on exploring the use of PS-OFDI for hypertrophic scar monitoring between the Center for Biomedical OCT Research and Translation, Center for Engineering in Medicine at Massachusetts General Hospital and Shriners Burn Hospital (Professors Alex Golberg and Martin Yarmush), Division of Plastic and Reconstructive Surgery at MGH (Dr. Felix Broelsch, Dr. Saiqa Khan, and Dr. William Austen), and Program in Dermatopathology at Brigham and Women's Hospital (Dr. Christine Lian). In the second phase of my PhD, I was very fortunate to be mentored by Néstor Uribe-Patarroyo who provided incredible insights in the critical NURD artifacts central to the final success of the implementation in a clinical catheter-based setting. I would also like to acknowledge the assistance from Katharina Höbel (a medical school student from Germany who I mentored) in the initial construction of our Comsol RF models. In addition, Milen Shishkov's assistance with the clinical catheter and fabrication of the custom RF electrodes, Sahar Kassani's assistance with the

Fabry-Pérot laser, Kathy Beaudette's assistance with the rotary junction, and Stephanie Nam's insights into the CDV algorithm are all much appreciated.

This journey would not have been complete without the joy of mentoring 3 classes of Harvard College freshmen in Matthews 4 as both their proctor and academic advisor. They have been a part of my extended family away from home and a big part of my life throughout my PhD. In particular, I would like to thank my peer advising fellows (PAFs) — Emma Kantor, Angelina Massa, and Jamie Stewart — for their support to the students in the final phase of my PhD. Their support, enthusiasm, and dedication have really been instrumental during this critical phase of my PhD journey. In addition, I would like to acknowledge a lucky bamboo from Aldís Elfarsdóttir for some potential element of luck instilled in the last part of my PhD journey.

The Harvard Biophysics program would not be complete without Prof. Jim Hogle and Michele Jakoulov. Their enthusiasm and dedication to the program have simply been phenomenal (as evidenced, for example, by the elaborate retreat theme every year!) They were the main reason why I chose to complete the Harvard-MIT MEMP program through Harvard Biophysics as my home department. Similarly, Dr. Loren Walensky and Amy Cohen's enthusiasm and leadership in the MD/PhD program have really transformed the program during my time in the program. I would also like to thank Dr. Roger Mark and Dr. Carl Rosow for providing me with the teaching experience at MIT and Harvard Medical School so that I can keep my clinical knowledge mostly intact during my PhD as I make my transition back to the final years of my MD.

This work would not be possible without a number of funding sources as well, including the generous support from the Canadian Institutes of Health Research (CIHR) through the Doctoral Foreign Study Award and the National Institutes of Health (NIH) P41 Center grant funding.

Finally, I would like to acknowledge the support from my parents, brother (Raymond), and sister (Carol) throughout my time in the MD/PhD program, my HST MD advisor Prof. Rox Anderson, my MD/PhD advisor Prof. Jacquin Niles, my HST PhD advisor Prof. Richard Cohen, as well as my incredible early mentors in my life from the University of Toronto, especially Professors Lothar Lilge and Jonathan Rose, who sparked my interests in research and medicine.

1

Microscopic Image Guidance

1.1 *Precision medicine* as the future of medicine

Perhaps it has always been a dream for me to envision a future in medicine where we can diagnose and treat diseases such as cancer at an unprecedented level of precision. With the recent announcement of the NIH precision medicine initiative[*], there has been a resurgence of interest in innovative approaches to patient care that take into account individual variability to better tailor different therapeutic interventions, particularly in cancer treatments. While the concept of precision medicine itself is not particularly new (indeed, the term *personalized medicine* has been used for many years), recent technological advancements such as our ability to sequence the entire human genome have propelled

[*]NIH Precision Medicine Initiative. https://www.nih.gov/precision-medicine-initiative-cohort-program

this vision forward, thereby enabling more targeted therapies through molecular approaches that take into account the genetic heterogeneity of patients. However, in the new era of precision medicine, what is becoming clear is that we need to take a more holistic, interdisciplinary approach to the treatment of diseases as complex as cancer.

> "Tonight, I'm launching a new Precision Medicine Initiative to bring us closer to curing diseases like cancer and diabetes — and to give all of us access to the personalized information we need to keep ourselves and our families healthier."
>
> — President Barack Obama, State of the Union Address, January 20, 2015[16]

In particular, in the first part of this dissertation, I will literally "paint" a picture of a possible future framework of precision medicine where disease diagnosis and treatment can be performed at *microscopic* resolution by combining optical microscopy *in vivo* with machine learning and a noninvasive *laser printing/painting* technique (thereby enabling localization and targeted biopsy/therapy delivery). In the second part of this dissertation, I will describe another embodiment of this new form of image guidance, termed *microscopic image guidance*, which is capable of precisely targeting lesions in different parts of the body using an integrated thermal therapy monitoring approach to disease diagnosis and therapy delivery.

1.2 Conventional image guidance

The term "image-guided therapy" (or more broadly "image guidance") has traditionally been confined to predominantly *macroscopic* clinical imaging modalities such as computed tomography, magnetic resonance imaging, and ultrasound imaging, which offer limited spatial resolution, especially for guiding therapeutic interventions in epithelial lesions where a high precision is required. A typical image depicting an operating suite with conventional image guidance is shown in Figure 1.1. Indeed, it is *macroscopic* both in the sense of the instrumentation and the ability to resolve the object being imaged.

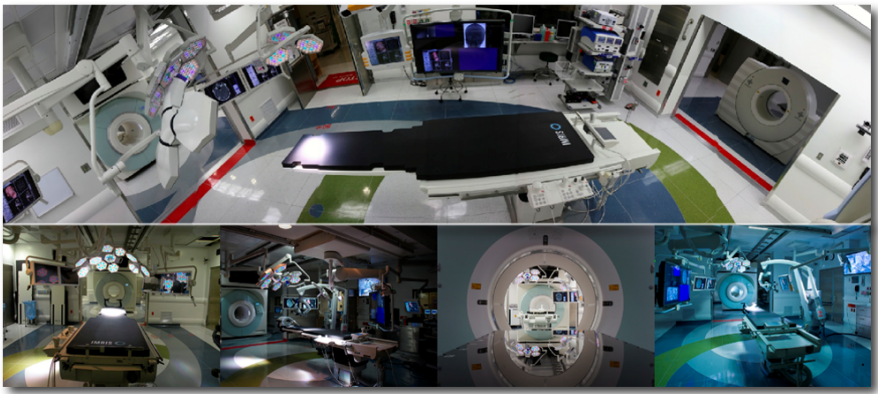

Figure 1.1: An example of an operating suite with *macroscopic* image guidance tools such as computed tomography (CT), magnetic resonance imaging (MRI), or positron emission tomography (PET) machines. Image credit: Advanced multi-modal image-guided operating (AMIGO) suite at Brigham and Women's Hospital - http://ncigt.org/amigo

Here, we introduce the notion of *microscopic image guidance* that differs in two important ways: 1) the imaging device is significantly miniaturized, through the construction of small optical imaging probes, which enable access to many disease sites that were traditionally impossible to reach, 2) the resolution is significantly improved to the level of enabling microscopic examination of tissue in living patients.

1.3 Microscopic image guidance

The enabling optical imaging technology is called optical frequency domain imaging (OFDI), which is a second-generation optical coherence tomography (OCT) technique that offers high-speed, high-resolution volumetric imaging ($\sim$10 μm). Our earlier clinical studies using OFDI have demonstrated its potential to identify early precancerous changes in the esophagus, called Barrett's esophagus (BE), which arises from chronic acid reflux from the stomach[78,80,87]. Chronic acid reflux or gastroesophageal reflux disease (GERD) — a condition that commonly presents as heartburn — is very prevalent in the US and affects $\sim$10-20% of the US population[24]. Over time, chronic acid reflux transforms the top layer of the esophagus — the epithelium — into a more protective type of tissue seen in the intestine; this transformation is called intestinal metaplasia — an important pathological feature of Barrett's

esophagus. Unfortunately, Barrett's esophagus, in the late stage, becomes a highly lethal cancer called esophageal adenocarcinoma with a dismal 5-year survival of ∼15%[94]. The current gold standard for the clinical diagnosis of BE is random four-quadrant biopsy through a longitudinal endoscopic surveillance program, which is prone to sampling error. In cases where high-grade dysplasia (the high-risk, pathological stage preceding cancer) is identified, physicians typically perform ablation therapies such as radiofrequency ablation (RFA). While RFA is an established treatment modality that leads to the regression of disease and regrowth of the squamous epithelium if performed successfully, it is typically guided only by *macroscopic* surface features through endoscopy. Conventional endoscopy, however, can lead to missed buried BE regions or overtreatment of healthy regions resulting in complications such as stricture formation in up to 8% of patients (which prevents patients from swallowing and requires immediate interventions)[75]. Therefore, there is a strong need for both better screening tools for early diagnosis and early treatment when the treatment outcome remains highly favorable. Indeed, clinical studies have shown that the complete response rate is >90% with RFA treatment for low-grade dysplasia and nondysplastic BE (the early stages)[76].

While the OFDI imaging technology has recently enabled the comprehensive, 3D examination of the esophagus at high resolution to identify suspicious Barrett's esophagus regions for more targeted biopsy[79,78], there still exists a large gap between diagnosis and treatment that can be bridged through a more holistic, integrated image guidance approach. Two potential frameworks are illustrated as follows.

The first framework, as depicted in Fig. 1.2 and discussed in detail in Chapter 2, outlines a laser painting and machine learning approach that enables targeted biopsy and treatment with microscopic image guidance in the challenging endoscopic setting. The endoscopic environment in the esophagus is probably one of the most challenging for image registration due to viewpoint changes, partial occlusion, and deformation of the esophagus. Therefore, two important innovations are proposed here. First, using a noninvasive laser painting paradigm with a customized biodegradable spray-on substrate,

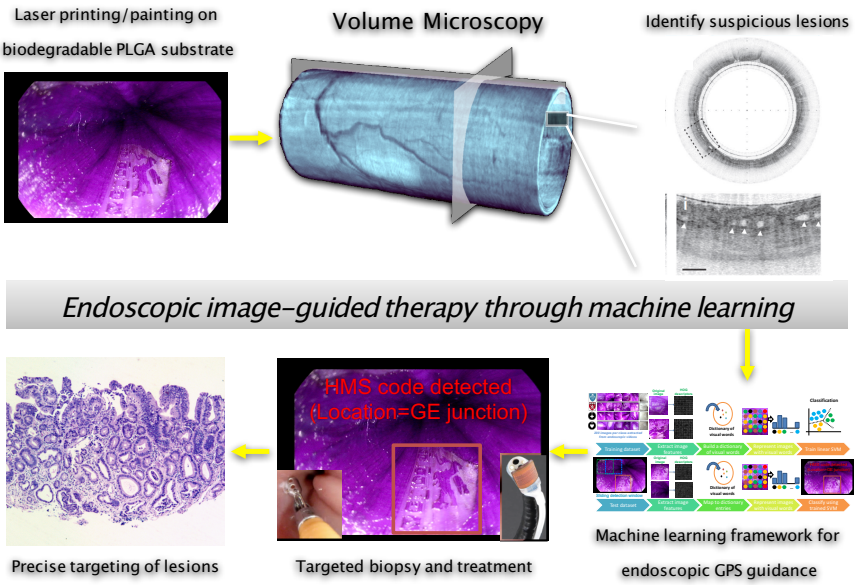

Figure 1.2: A new form of microscopic image guided therapy using a combination of laser painting with a biodegradable spray-on substrate and machine learning to co-register two very distinct modalities (endoscopic images and OFDI images), thereby enabling navigational and treatment guidance in the extremely challenging endoscopic environment.

a set of navigational landmarks are painted on the surface of the esophagus through photobleaching of a light-sensitive dye with a laser beam. Then, comprehensive, 3D microscopy is performed using the balloon OFDI catheter in the esophagus, which enables the identification of suspicious lesions (i.e. Barrett's esophagus regions). To overcome the significant challenges in the endoscopic environment, a machine learning approach was developed to identify these landmarks, thereby essentially decoding a set of endoscopic GPS coordinates. By overlaying this virtual endoscopic GPS map during the endoscopic procedure, a distinct frame corresponding to the OFDI dataset can be identified - a process called co-registration - so that we can see beneath the surface and analyze the underlying disease region at the same time. The key is that these navigational landmarks must be highly visible on both conventional endoscopy and on OFDI imaging, such that co-registration (or co-localization) of both datasets is possible.

The second framework, as illustrated in Fig. 1.3 and discussed in detail in Chapters 3 through 6, out-

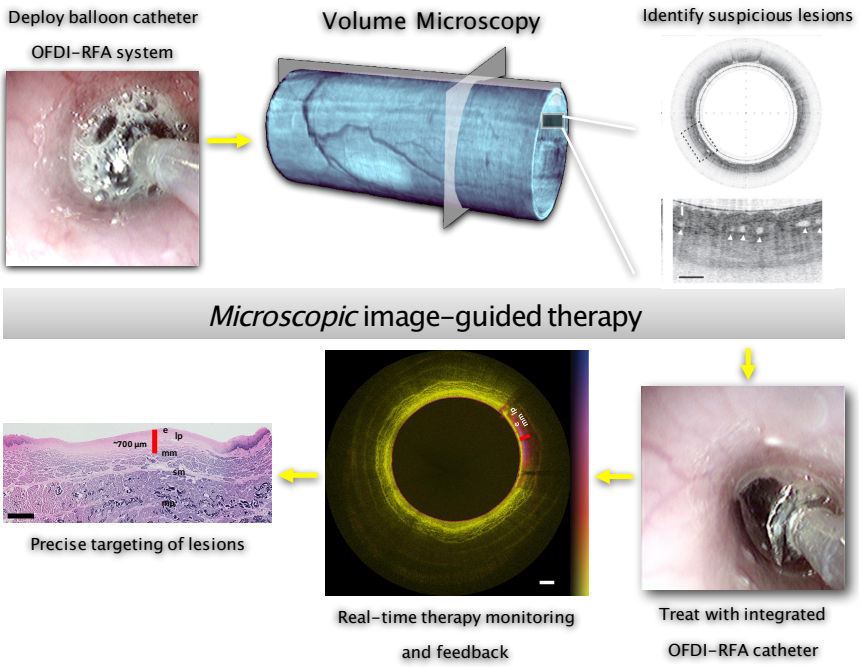

Figure 1.3: Integrated microscopic image-guided therapy platform: imaging, thermal therapy delivery, and monitoring are performed using a single balloon catheter which has a flexible radiofrequency electrode array around the balloon. Real-time therapy monitoring using OFDI ensures that the target lesion is treated at precisely the desired depth with feedback to achieve optimal outcome and minimize complications in patients.

lines another approach that directly integrates imaging, therapy delivery, and monitoring in a single balloon catheter. While this approach is less flexible, it is an elegant approach to stabilize the deformation of the esophagus and ensure that energy delivery to the precancerous lesion is precisely tailored based on real-time imaging.

1.4 Thermal therapy monitoring

While the proposed frameworks described above can be applied to many types of epithelial lesions, our immediate focus is Barrett's esophagus given it is an easily accessible target by endoscopic intervention with an existing surveillance program and a treatment protocol involving thermal therapy. It is also a

target with high clinical significance given it is a precursor lesion to esophageal adenocarcinoma which is associated with a high mortality and morbidity rate. The goal of this work is the development of an OFDI-guided and OFDI-monitored ablation therapy platform that provides pre-operative OFDI image guidance to assist with targeted biopsy and focal treatment (through framework 1 illustrated in Fig. 1.2) or peri-operative OFDI guidance and real-time monitoring of therapy depth (through framework 2 illustrated in Fig. 1.3) to assist with thermal therapy treatment in larger segments. In this section, we will focus on a specific thermal therapy modality — radiofrequency ablation — in Barrett's esophagus given its widespread clinical adoption.

Radiofrequency ablation (RFA) is currently an approved and widely adopted treatment modality for Barrett's esophagus patients with dysplasia. While the use of RFA in high-grade dysplasia is clear, its current use in early, premalignant stages (such as low-grade dysplasia [LGD] and non-dysplastic BE) is controversial due to the potential risk of complications and cost of treatment due to repeated sessions, despite the higher complete response rate. For example, the risk of stricture formation, which results from overtreatment, ranges from 2% to 8%[75], and multiple treatment sessions (up to 4-6 sessions for >8cm segments[53]) are typically required to achieve complete response. A major limitation of the current treatment paradigm is that a standardized energy setting is used by assuming a uniform lesion depth and no real-time monitoring tool is available for RFA in BE patients to ensure that the desired target lesion depth is actually achieved. Therefore, a real-time monitoring tool that provides an accurate measure of treatment depth will greatly increase single-procedure efficacy and reduce complication rate, thereby potentially opening up the possibility of using RFA in treating BE with LGD and non-dysplastic BE, when the complete response rate remains very high (>90%)[76].

While RFA monitoring is not routine in BE treatment, it is typically used for other sites such as liver tumor ablation. However, current state-of-the-art techniques[73,20,58,57,36,43] for monitoring thermal ablation often rely on bulk tissue property measurements (such as temperature at relatively low spatial resolution), and hence lack the sensitivity for precise spatiotemporal control of the therapy. A major

limitation of temperature measurement using conventional thermocouples is that they only permit point sampling, while emerging magnetic resonance thermometry[73,20] techniques are very expensive and are limited by the low spatiotemporal resolution. The large size of the imaging equipment is also not very practical for the endoscopy suite setting. Photoacoustic thermography of tissue has recently been demonstrated for the assessment of myocardial RF ablation lesions *in vitro*[43], but the spatial resolution (∼1 mm) remains low for epithelial applications such as BE treatment.

Within the domain of OCT imaging, there is currently only a limited number of related studies on thermal therapy monitoring. One of the early ideas involved the use of polarization-sensitive (PS) OCT to assess thermal damage through reduced tissue birefringence caused by denaturation of collagen in porcine tendon and skin[19]. This is analogous to techniques based on polarized light microscopy. However, PS-based measurements cannot be generally applied to all tissue types given that not every tissue type exhibits high birefringence at baseline (which is the primary contrast mechanism here). In terms of other approaches, Prof. Rollins' group investigated the use of a forward-imaging OCT catheter for monitoring cardiac RF ablation lesion using conventional intensity OCT images and noticed the increased signal intensity with ablated lesions in a swine heart both *in vitro* and *in vivo*[26], but it was difficult to delineate the ablation zone boundary using only an intensity-based technique. In terms of using OCT for imaging ablation therapy in BE, the most relevant work only investigated the characterization of buried glands before and after RF ablation or cryoablation, but not during ablation[101]. In fact, this previous work demonstrated the potential of using volumetric OCT for detecting buried glands which evade detection and lead to recurrence/dysplastic progression. For these reasons, the use of OCT in the clinical environment could be greatly facilitated by the development of a comprehensive real-time RFA monitoring method with potential for clinical translation. Additionally, RFA therapy is currently performed unguided: apart from visual inspection during video endoscopy, there is no pre-arranged therapy plan that describes the areas requiring treatment and at which depth level (which is further complicated by the lack of a monitoring technique to ensure that the desired

treatment depth is achieved). OCT can be used to prepare the therapy plan and to create a map of the regions that require treatment. It would be very valuable to present this information during video endoscopy to enable real-time OCT guidance of RFA therapy, complemented by real-time OCT injury depth monitoring.

1.5 Organization of dissertation

In the next chapter, we discuss in detail the endoscopic image-guided framework, illustrated in Fig. 1.2, based on machine learning and laser painting in the esophagus. In Chapters 3 and 4, we investigate the use of polarization-sensitive optical frequency domain imaging (PS-OFDI), specifically using a combination of local retardation and degree of polarization, for monitoring laser thermal therapy and hypertrophic scar remodeling *in vivo*. While PS-OFDI offers the ability to delineate the coagulation zone accurately in the skin, these two chapters motivate the development of a more generic framework in Chapter 5, based on complex differential variance, to enable thermal therapy monitoring in diverse tissue types. Chapter 6 demonstrates the translation of the CDV-based technique to a clinical catheter-based setting, which poses a series of additional challenges including non-uniform rotation distortion artifacts, and illustrates the implementation of the microscopic image guidance platform outlined in Fig. 1.3.

Future clinical translation of the microscopic image guidance platform will lead to a real-time, OCT-based monitoring and guidance platform for RFA that offers the ability to tailor the treatment depth to the geometry of the target lesion. This is expected to reduce variability and cost in repeated treatment and improve outcomes, which can potentially enable the broader use of RFA for treating earlier stages of BE in order to achieve a higher complete response rate and a lower morbidity rate.

2

Endoscopic image-guided therapy and diagnosis

Recent advances in subsurface imaging techniques, such as optical coherence tomography (OCT) and endoscopic ultrasound (EUS), have enabled their use as valuable clinical diagnostic and therapeutic guidance tools by enabling detailed examination of underlying tissue architecture non-invasively in numerous organ systems[78,80,87,11,68,37,95,14]. However, in many clinical applications such as Barrett's esophagus screening, colorectal cancer screening, or radiofrequency ablation for dysplasia, endoscopy remains the routine procedure for disease diagnosis/surveillance and therapeutic guidance. Unfortunately, conventional endoscopic examination alone provides limited information beyond surface mor-

phology and superficial structures, necessitating routine biopsy for diagnosis and broadly limiting its ability to accurately guide therapeutic interventions.

While subsurface imaging techniques such as OCT or EUS provide valuable complementary information, they are often difficult to interpret without context (e.g., without exact anatomical location and surface morphology/features). In addition, for longitudinal disease surveillance, it can be difficult to relocate the same suspicious region examined months to years apart, which prevents the accurate assessment of the progression of disease and limits the current diagnostic utility of endoscopic surveillance procedures. Hence, strategies to enable robust navigational guidance in endoscopy and the seamless integration of subsurface imaging modalities with endoscopy (through the co-registration of these two modalities both spatially and temporally across multiple sessions for longitudinal assessment) would significantly broaden their current use models and potentially facilitate greater adoption of these novel imaging techniques.

While there is a plethora of previous work in conventional multi-modality co-registration (such as PET/CT or CT/MRI)[54,55,39], co-registration between endoscopy and subsurface imaging modalities is hindered by a number of unique challenges. These challenges include: 1) the lack of a common coordinate system for image generation (e.g., forward viewing camera in endoscopy and circumferential balloon catheter in OCT); 2) the presence of significant motion artifacts, deformation, and variations in imaging/lighting conditions (induced by both the physician and the patient, inherent to endoscopic procedures); and 3) the lack of a rich set of robust intrinsic landmarks beyond basic anatomical ones. Strategies to overcome these obstacles would enable the integration of subsurface imaging modalities with endoscopy for such novel applications as a true virtual biopsy (detailed examination of tissue microstructure non-invasively at a given location without physically removing tissue) during endoscopy as well as highly targeted image-guided therapeutic interventions, leading to earlier diagnosis and more comprehensive disease management.

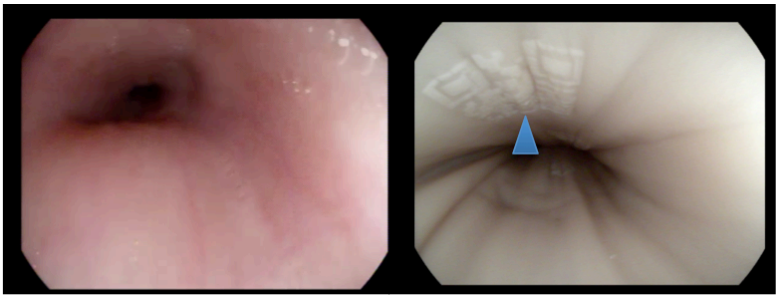

Figure 2.1: Left: A typical scene in endoscopy during longitudinal surveillance of suspicious lesions. Right: An example of an enriched endoscopic scene with a navigational landmark. In this case, a QR code (blue arrowhead) — a special barcode — was generated with a high-power thulium fiber laser.

2.1 Navigation through *laser painting* and machine learning

Figure 2.1 shows a typical endoscopic scene in the esophagus, which illustrates clearly the challenges in the endoscopic environment. The endoscopic environment in the esophagus is possibly the most extreme and most challenging setting for image guidance. Not only is this body organ highly deformable, but the endoscopic scene does not typically contain a rich set of robust intrinsic features that can be easily tracked. This poses a very significant challenge to the implementation of a robust image registration algorithm and accurate localization scheme to enable image guidance, especially if one requires sub-millimeter accuracy for the realization of the concept of microscopic image guidance.

However, a moment of inspiration came one day – what if we could develop a technique to print or *paint* some navigational landmarks directly on the esophagus noninvasively? If this could be achieved, what should these landmarks look like? Could we encode information somehow, such as in the form of a QR code (or Quick Response code, which is a special type of barcode to efficiently encode information, such as in electronic boarding passes)? An example of an enriched scene with a QR code placed on the tissue surface is shown on the right side of Fig. 2.1.

Here, a novel technique for *laser printing* or *laser painting* on esophageal tissue, discussed in further details in the next section, was developed to generate a set of robust navigational landmarks to

encode location. The ideal technique should be noninvasive (i.e., it should not destroy the region being examined), but should, at the same time, be persistent (given the need to insert an endoscopic probe). These represent two paradoxically opposite requirements. For example, the most persistent method to generate a landmark is to tattoo a mark (e.g., with a high power laser) which clearly cannot be considered completely noninvasive.

In addition, to tackle the challenging environment in endoscopy including significant viewpoint changes (given the endoscopist can maneuver the camera in any direction), partial occlusion (potentially caused by mucus in the esophagus), and deformation (due to the natural distention and motion in living patients), conventional approaches to image registration will not suffice. Therefore, two machine learning schemes were investigated to distinguish between navigational landmarks robustly in this very challenging setting. The first model is known as a bag-of-words or bag-of-keypoints model[17], which involves constructing a dictionary of visual words to efficiently represent images in histogram of image patterns (in an orderless collection). This computationally efficient model is intrinsically robust to background clutter, affine transformation as well as variations in viewpoint, lighting, occlusion typical in real-world generic visual categorization of objects. To augment with the geometric relations between neighboring image patterns, an extension of the bag-of-words model called spatial pyramid image representation was investigated. In the spatial pyramid representation, an image is partitioned in different levels of resolution and histograms of local features are computed in each subregion at each level[49]. In addition, a simpler approach involving vectorizing histogram of oriented gradients (HOG) descriptor[18] and classification using linear support vector machine (SVM) was investigated for baseline performance comparison. Interestingly, the HOG descriptor, a feature descriptor that is used to represent an image, was shown to be very useful for pedestrian detection. Using the average precision as the performance metric and a manually generated dataset of over 1000 images, various designs of navigational landmarks were assessed and the feasibility of localization through the classification of a navigational landmark was demonstrated.

2.2 *Laser painting* in an endoscopic setting

In this section, the general conceptual framework for *laser painting* is introduced. Two general embodiments of possible tissue patterning or painting models are summarized in this section and a particularly promising approach will be investigated in subsequent sections.

The first embodiment involves the *selective dye transfer* model. Here, the tissue surface is selectively modified or primed through physical, chemical and/or biological means (which can be used in isolation or in combination) for subsequent application of dye for staining. Physical means include selective ablation, micropore generation, or other thermal/non-thermal methods to disrupt the surface. Chemical means include the application of chemical constructs that bind well to the tissue surface and the desirable dye (the affinity may be further modulated). Biological means include modifications of the cell surface, activation of biological pathways or selective activation of epithelial cells that increase permeability, binding affinity, or the absorption of dyes.

The second embodiment involves the *selective dye removal* model. Here, a dye is first uniformly deposited on the tissue surface. Subsequent selective removal of the dye, accomplished through physical, chemical or biological means, enables the creation of highly customizable patterns. For example, biocompatible tissue dyes or stains, such as those currently used in chromoendoscopy (including absorptive stains such as methylene blue, toluidine blue, Lugol's solution, crystal violet; contrast stains such as indigo carmine; reactive stains such as phenol red or congo red), photocrosslinkable dyes such as Rose Bengal, food colors, or the like, can be deposited uniformly on the tissue surface. Subsequent application of an electromagnetic radiation at a suitable wavelength (such as visible light matching the absorption peak of the dye) can be exploited for the selective excitation, conversion, or deactivation (e.g. photobleaching) of the dye.

In this chapter, we will focus on the *selective dye removal* model. In particular, chromoendoscopy dyes commonly used in Barrett's esophagus patients (including crystal violet, toluidine blue and methy-

lene blue) are deposited on the tissue surface followed by selective photobleaching to achieve different design patterns. A particularly promising approach that integrates a Poly(Lactide-co-Glycolic Acid) (PLGA) substrate to generate a water-resistant film (to prevent the dye from smearing and preserve the pattern after photobleaching) was developed and tested in porcine esophagus *ex vivo*. A potential clinical patterning probe design that can enable high-speed, high-resolution patterning *in vivo* is discussed in Section 2.7.1.

Finally, Fig. 2.2 shows a clinical flowchart to further illustrate a particular use model of the present framework. First, a patterning probe is placed via endoscopic guidance around a region of interest (ROI) in step 1. Next, a tracking pattern is generated in the ROI in step 2, and the entire ROI is comprehensively imaged with a subsurface imaging probe in step 3. Note that steps 1 through 3 can be completed in one step with an integrated probe. Using the tracking pattern, the subsurface imaging dataset is spatially co-localized (or co-registered) with the real-time endoscopic image stream in step 4. In all subsequent assessments of tissues within the ROI, real-time navigational guidance is realized by decoding the location represented by the tracking pattern in step 5. Virtual biopsy can be performed in step 6 for detailed examination. The term virtual biopsy refers to the ability to assess the tissue microstructures below the surface to identify suspicious lesions without physically extracting tissue samples. Finally, the endoscopic procedure of interest, from a routine biopsy to more sophisticated interventions such as radiofrequency ablation, can be performed using this image-guided framework in step 6. Note that another attractive use model involves placing a tracking pattern for navigational guidance in longitudinal surveillance (to enable the accurate and efficient longitudinal assessment of suspicious lesions).

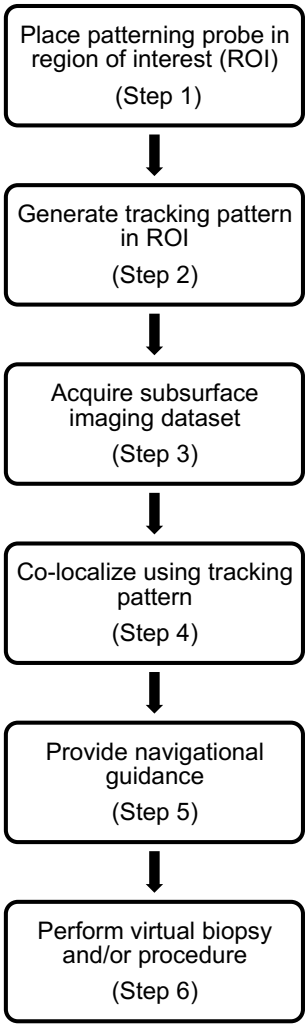

Figure 2.2: Clinical workflow illustrating how pattern generation, tracking/co-localization, and navigational guidance can be incorporated to enable endoscopic image-guided procedures.

2.3 Introduction to endoscopic scene understanding

Scene categorization and understanding is one of the most fundamental challenges that physicians face in the endoscopy suite on a daily basis. For example, to make a diagnosis, physicians need to efficiently analyze a large sequence of endoscopic images in real-time and categorize them as either normal or abnormal lesions. In longitudinal surveillance programs, such as Barrett's esophagus screening or colon cancer screening, it is often necessary to accurately identify suspicious areas and relocate them (to assess progression) months to years later. Therefore, a computer-assisted method to provide navigational guidance that enables rapid re-identification of suspicious lesions and subsurface examination of the disease region simultaneously would be extremely beneficial for: 1) the accurate assessment of disease progression, and 2) the reduction of procedure time.

Here, we propose the notion of enriching endoscopic scenes as a first step towards scene understanding in endoscopy. In particular, navigational landmarks are generated using a laser-based tissue painting strategy (either through *laser marking* where permanent landmarks are created or *laser printing/painting* where landmarks are created noninvasively through photobleaching of a light-sensitive dye) and are subsequently classified for localization. Figure 2.3 demonstrates such a laser printing/painting approach using clinically approved chromoendoscopy dyes (these dyes have been investigated for enhancing contrast to better identify suspicious lesions for disease diagnosis). First, three different chromoendoscopy dyes were painted on the tissue surface. Using a focused red laser beam, the MGH logo was then printed/painted on the surface of the esophagus. The laser painting technique is a very interesting approach since navigational landmarks can be painted/printed noninvasively if the dye is combined with a biodegradable, nontoxic substrate in the esophagus. Furthermore, the low power requirements associated with photobleaching of a light-sensitive dye, compared to laser marking, means that a low-cost diode laser can be used and that the procedure can be performed very safely.

Figure 2.4 further depicts the proposed endoscopic image-guided therapy platform, which co-registers

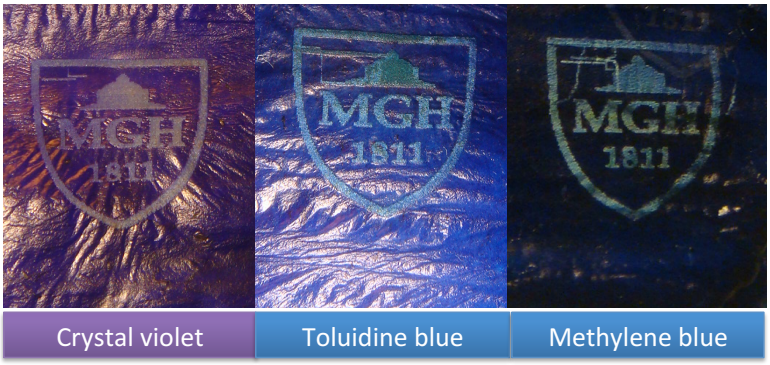

Figure 2.3: Laser printing with three chromoendoscopy dyes commonly used in Barrett's esophagus patients (crystal violet, methylene blue, and toluidine blue). The chromoendoscopy dyes were applied evenly on porcine esophagus *ex vivo* and laser printing was performed using a 635 nm diode laser.

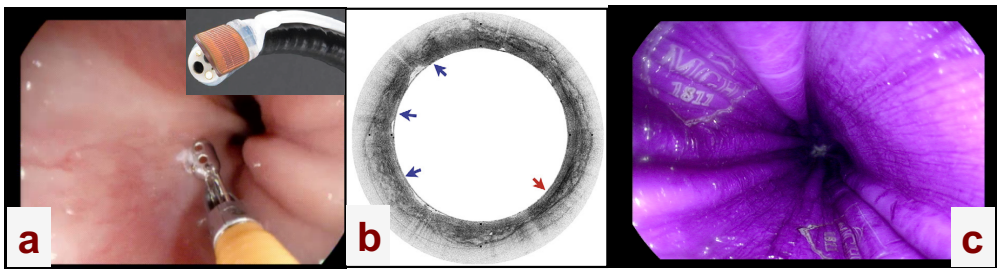

Figure 2.4: Proposed endoscopic image-guided therapy framework, where an OFDI dataset is co-registered using navigational landmarks visible in both endoscopy and OFDI. (a) Typical scene in an endoscopic procedure (e.g., biopsy or focal ablation of lesions), (b) Representative OFDI dataset from a Barrett's esophagus patient [80], (c) *Laser-printed* endoscopic GPS coordinates (in this case, the MGH logo) for co-registration.

the OFDI volumetric imaging datasets with endoscopic images through the use of custom navigational landmarks visible in both modalities. Notice that in this case, the endoscopic image (Fig. 2.4c) shows a laser-printed MGH logo on a biodegradable PLGA substrate/film (hence the glossy surface since this is water-resistant) that was sprayed on the esophagus prior to photobleaching.

2.4 Previous work on navigational guidance in endoscopy

Previous studies in computer-aided navigational guidance in endoscopy primarily focused on using expensive additional instrumentation for tracking. For example, one approach involves directly plac-

ing radiofrequency (RF), wireless trackers on the endoscopic tip in laparoscopic surgery[46] or optical tracking devices to spatially register CT scans to endoscopic images for improved navigation within a body cavity, such as surgery through the sinus[13]. Another body of work has been devoted to the concept of simultaneous localization and mapping (SLAM) by identifying tracking features and building a 3D map[22] in endoscopy, particularly in minimally invasive surgery[60]. However, this approach will be challenging to apply in the case of endoscopy in the esophagus given the lack of distinct features that can be robustly tracked. Therefore, the ability to provide tracking capability within the esophagus without external instrumentation, using fudicial markers painted on the surface of the esophagus, will be very appealing. Furthermore, this will establish the basis for a more general framework for computer-vision based scene understanding (for example, as applied to the more general classification of suspicious lesions, beyond specific navigational landmarks), which would be very exciting and useful in longitudinal surveillance programs potentially.

2.5 Datasets and Methodology

The first step to begin the process of exploring the idea of navigational guidance through laser-printed landmarks involves generating image datasets representative of the realistic endoscopic setting. In addition, different design patterns were assessed to measure the performance of a classification algorithm, using a metric known as average precision which is commonly used in computer vision for benchmarking the performance of classification algorithms.

2.5.1 Generation of datasets

To generate the required training and testing datasets, multiple endoscopy sessions were performed inside porcine esophagus in an ex-vivo setting. For the laser marking approach, customized patterns were created using a high-power thulium continuous wave fiber laser. The wavelength of light was

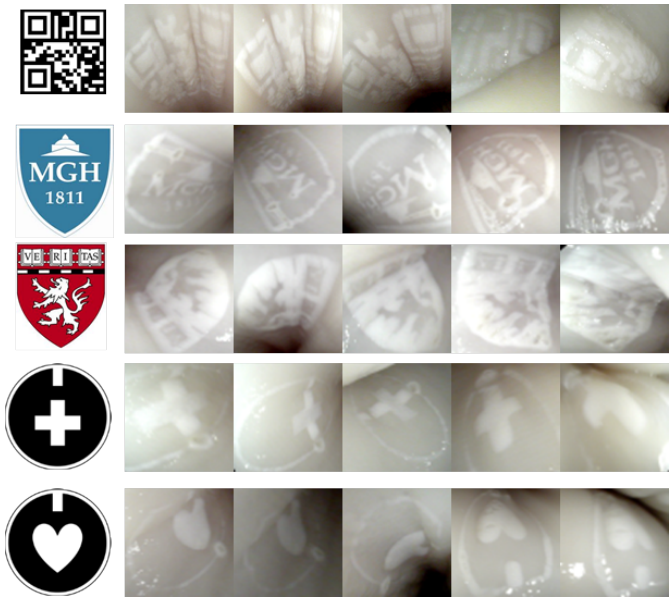

Figure 2.5: Representative examples of endoscopic image datasets for 5 different navigational landmarks generated using a thulium fiber laser.

tuned to match the absorption peak of water in tissue (at 1890 nm) for efficient tissue coagulation and the power was adjusted to enable superficial coagulation of the tissue. Five different landmarks of varying degrees of complexities were investigated including the QR code presented earlier, as shown in Fig. 2.5. Representative images were extracted from endoscopy video streams to capture the common scenarios and challenges seen in endoscopy, such as viewpoint changes, partial occlusion, and deformation. For each class, 200 images were generated from multiple endoscopy sessions from multiple tissue specimens. A dataset of 1000 images with class labels was generated.

The same procedure was repeated for the laser printing/painting approach (see Fig. 2.6 described earlier, where a chromoendoscopy dye embedded in a biodegradable PLGA solution is sprayed on the esophagus to generate a water-resistant film), which shows the dramatic improvement in the contrast of the images obtained. The four landmarks were chosen to represent 2 pairs of very similar landmarks to assess the performance of the algorithm.

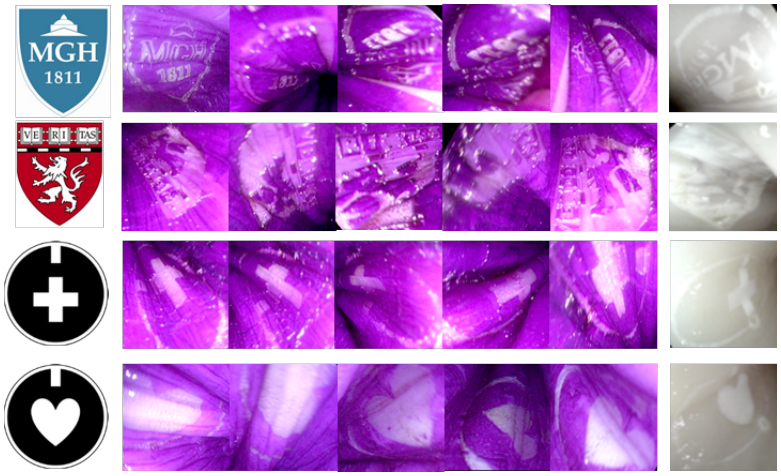

Figure 2.6: Representative examples of endoscopic image datasets for 4 different navigational landmarks generated using a laser printing approach with a chromoendoscopy dye (crystal violet).

2.5.2 Overview of algorithms

Figure 2.7 shows an overview of the proposed endoscopic navigational guidance algorithm based on the concept of classifying unique landmarks representing different locations. This machine learning framework consists of a training stage and a testing stage. Within the training stage, a series of representative images for each landmark (100 per landmark for training, 100 for testing) were used as the input to teach the computer what each landmark looks like under all kinds of challenging endoscopic scenarios, including deformation, partial occlusion, and viewpoint changes. This involves building a dictionary of visual words based on the image features extracted from each landmark and re-encoding each image with this dictionary of visual words to train the machine learning algorithm. Visual words can be thought of as essentially the fundamental elements (salient image features) that can compress the representation of each image. This machine learning model is known as the bag of words model[17], which has also been applied to face recognition and the general object recognition problem, but it has not been applied to endoscopic feature recognition. Once the training stage has been completed, the real-time endoscopic video stream is analyzed using the trained algorithm. A similar set of stages are

used to extract image features in a sliding window to detect the presence of different landmarks, which are then mapped to dictionary entries of visual words for more compact representation and classification using the algorithm. The final result from the classification is used to determine the encoded location.

The first version implemented is an orderless bag of words model using the VLFeat library[89]. The histogram of oriented gradient (HOG) descriptor[18], an image descriptor that has shown great promise for pedestrian detection, is used for feature extraction. A dictionary of visual words is constructed using k-means clustering. Finally, a linear support vector machine — a commonly used machine learning and classification engine — is used for classification.

The second version implemented is a bag of words pipeline that incorporates spatial pyramid matching[49] and locality-constrained linear coding[93] – techniques that were shown to be beneficial in certain classification problems where the objects have typically well defined structures. The feature extraction toolbox created by Khosla et al. [44] was used for this experiment.

Finally, for baseline comparison, we implemented a highly simplified pipeline that completely eliminates the use of a dictionary and the representation of images using such dictionary of visual words. In this pipeline, each image is normalized to a standard size (50 x 50 pixels) and HOG features were extracted. The HOG descriptor was simply vectorized for classification using linear SVM. The rationale for implementing this model is to investigate the performance gain (or loss), in terms of average precision, achieved with a more sophisticated bag of words model. The simpler model is also attractive if it yields acceptable classification performance as it is highly efficient for future real-time implementation (which might be useful for the broader detection problem).

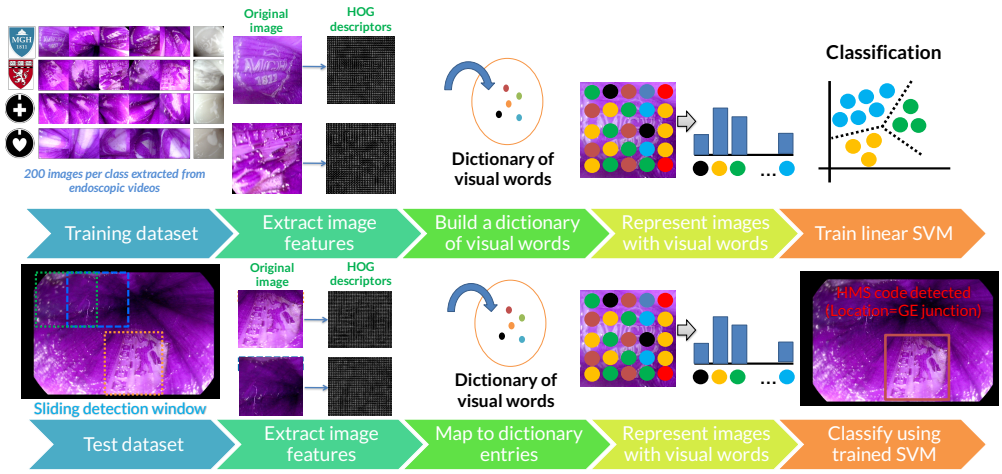

Figure 2.7: Overview of proposed endoscopic, machine learning based navigational framework. Recognition of laser-printed navigational landmarks is performed through object classification and machine learning. Top panel: Overview of major training stages (a representative dataset consisting of 200 images per class was extracted from endoscopic videos; 100 for training, 100 for testing). Bottom panel: real-time identification of navigational landmarks in the esophagus for localization.

2.6 Results

2.6.1 Pairwise classification

Figure 2.8 shows the relative performance of two variants of the bag of words (BOW) model compared to the baseline algorithm for a representative pair of landmarks - the MGH logo vs. a customized tracking symbol with a heart in the center. A training dataset of 100 images was used for each class and the trained algorithm was tested against 100 images per class taken at a different endoscopy session with a different tissue specimen. A dictionary size of 10 visual words was chosen for both the orderless BOW model and the BOW with spatial pyramid model. Interestingly, the baseline algorithm achieves an average precision (93%) comparable to that of the orderless BOW approach (94%). In addition, both models slightly outperform the more sophisticated BOW model with spatial pyramid.

To confirm this finding, another pair of landmarks (heart vs. cross) was tested (Fig. 2.9). Again, the bag of words models show average precision values similar to the baseline. As expected, the average

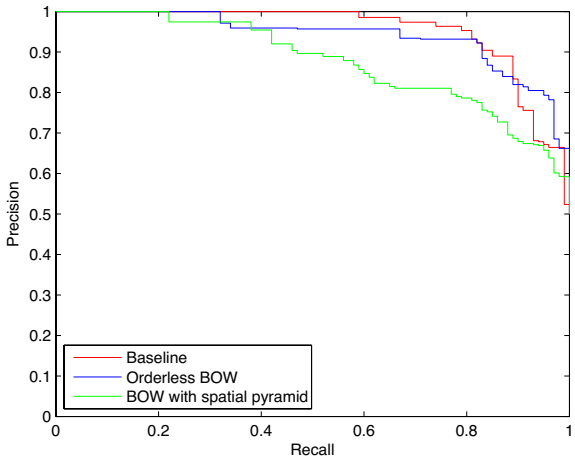

Figure 2.8: Precision-recall curves for a representative pair (mgh vs. heart) illustrating the relative performance of each algorithm (average precision: Baseline = 93%, Orderless Bag of Words [BOW] model = 94%, Bag of Words [BOW] with spatial pyramid model = 87%).

precision dropped dramatically for all models tested, due to the similarity between the two landmarks.

To find a proper subset of landmarks that can be easily classified for navigational guidance, a more comprehensive study was performed, as shown in Fig. 2.10. Here, it is particularly interesting to see how the results follow one's intuition. For example, one would expect that pairs of landmarks with significant similarities (such as the heart vs. cross symbols or the MGH vs. HMS logos) should be more difficult for a machine to classify. Indeed, this is the case, as suggested by the low average precision value for the heart vs. cross pair compared to most other pairs. This interesting finding suggests that a subset of navigational landmarks can be designed and tested quantitatively for compatibility with one another to achieve optimal classification results. Another interesting observation is that in most cases, the bag of words model only provides a small performance boost compared to the baseline algorithm.

Finally, the benefit of using the laser printing approach was evaluated (Fig. 2.11), highlighting the fact that the dramatically improved contrast of the images provided by the chromoendoscopy dye improved the performance of the classification algorithm, as intuition would also suggest.

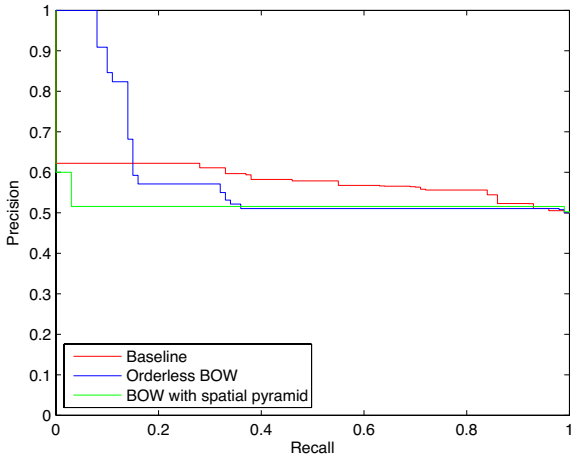

Figure 2.9: Precision-recall curves for another representative, worst-case pair (cross vs. heart) illustrating the relative performance of each algorithm (average precision: Baseline = 61%, Orderless Bag of Words [BOW] model = 60%, Bag of Words [BOW] with spatial pyramid model = 56%).

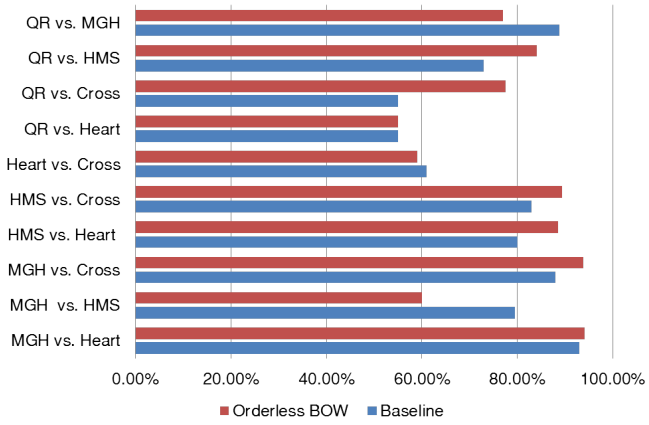

Figure 2.10: Average precision for the pairwise classification of different navigational landmarks using the baseline algorithm and the orderless bag of words (BOW) model.

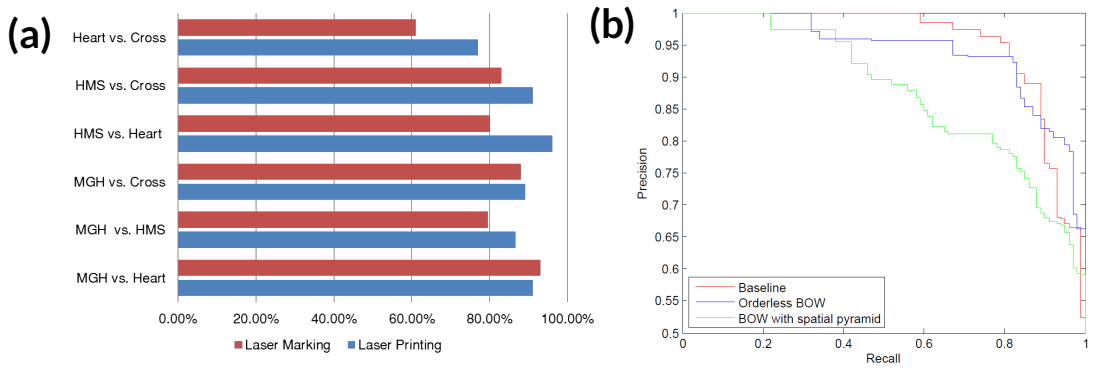

Figure 2.11: (a) Average precision for the pairwise classification of navigational pairs generated using laser marking (with the thulium fiber laser) vs. laser printing (with chromoendoscopy dyes). (b) Precision-recall curves for a representative pair (MGH vs. heart): average precision using baseline algorithm = 93%, orderless bag of words (BOW) model = 94%, bag of words (BOW) with spatial pyramid = 87%.

2.6.2 Localization of landmarks

Finally, to demonstrate the possibility of enabling navigational guidance using the approach discussed thus far, Fig. 2.12 demonstrates the localization of one of the navigational landmarks (in this case, the HMS logo) during an endoscopy session. This landmark was generated with the laser printing approach using crystal violet in a biodegradable PLGA film painted on the surface of the esophagus *ex vivo*. In particular, an overlapping scanning window of 128 x 128 pixels was specified as the detection window and each window was subsequently classified as either the HMS logo or the background. The green rectangular window indicates the location of the detected landmark in each frame. The results demonstrate the robust identification of the HMS landmark under a series of challenging scenarios typically seen in endoscopy, including significant viewpoint changes and deformation.

2.7 Translation to clinical setting

The translation of the proposed laser painting and machine learning framework to a clinical setting requires solving a number of important challenges. First, the design of a patterning probe to perform

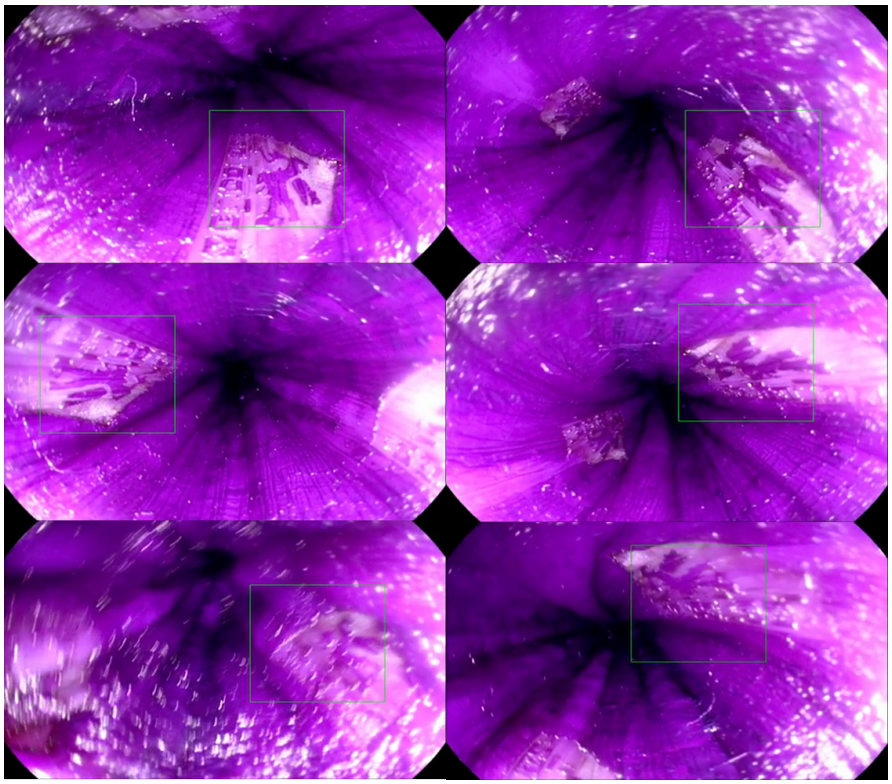

Figure 2.12: Localization of a *laser-printed* navigational landmark (HMS logo). The green rectangular window highlights the detected location of the identified landmark, showing the ability to correctly find the landmark despite viewpoint changes, different magnification and deformation with the machine learning approach.

laser painting *in vivo* is needed. Second, while the results demonstrate the feasibility of using a machine learning framework to classify landmarks and guide navigation, a more compact encoding scheme is needed to increase the number of distinct landmarks that can be painted in the small area of the esophagus and be recognized with high accuracy. This section discusses potential solutions to address both problems.

2.7.1 Laser painting *in vivo*

One interesting approach to realize laser painting *in vivo* is presented in Fig. 2.13. This approach enables rapid, high-resolution, mask-free patterning. This configuration illustrates 2 inflatable balloons to create a sufficient supply of air, although this can be simplified to a single balloon should the oxygen level *in vivo* be sufficient or with the use of a dye that is less oxygen-dependent. First, a tissue dye is directly deposited on the tissue surface and photobleached (or photoactivated or photoconverted) using a focused light beam that rotates around the flexible shaft to create a high-resolution custom pattern. A rotary junction (coupled to a light source) that enables rotation and translation (with an optional shutter) can be used to enable high-speed, computer-controlled micropatterning. This micropatterning procedure relies on a stable catheter rotation mechanism, which may be problematic due to the instability resulting from the proximal scanning scheme in clinical OFDI catheters. Therefore, a more stable distal micromotor design[83] may be necessary to achieve this. In addition, a dual clad fiber approach can be used to enable simultaneous imaging and laser painting in a single catheter configuration[9].

Another simpler design that does not require exquisite stability of the catheter is shown in Fig. 2.14, where a patterning film or mask makes direct contact with the tissue surface upon expansion of a probe. A colored pattern can be generated by selective photobleaching of exposed regions in the mask provided each mask contains a different color dye. In addition, a photoactivatable chemical construct can be uniformly deposited on the patterning film. Upon selective photoactivation, such a construct

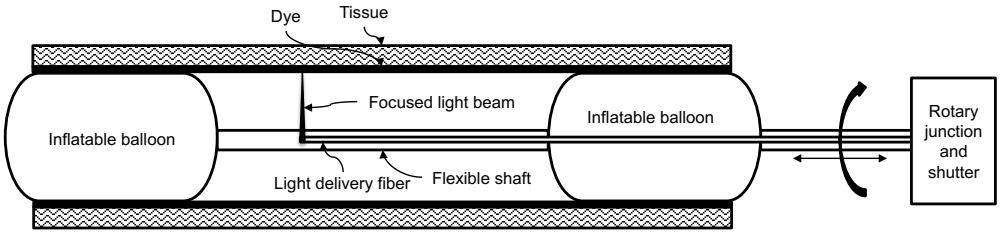

Figure 2.13: A double ballon catheter design to enable high speed, high-resolution laser printing *in vivo* . A focused light beam is delivered to the tissue which has been sprayed with a light-sensitive dye. Through the use of a rotary junction and shutter, laser printing *in vivo* can be performed across the surface of the tissue at high speed and at high resolution.

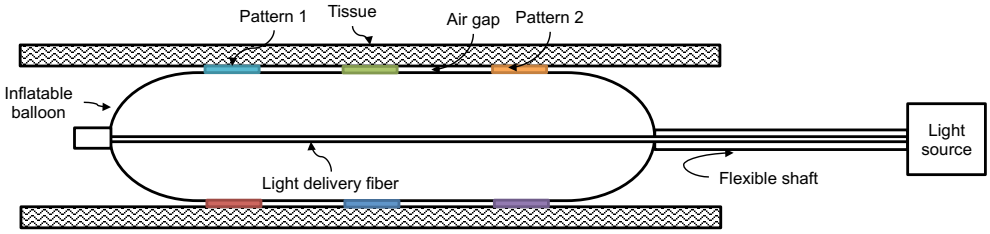

Figure 2.14: Overview of a particular patterning probe design which incorporates a series of patterning films on the outside of an inflatable balloon and a light delivery fiber that photoactivates or photobleaches a light-sensitive dye to create the desirable pattern.

preferentially adheres to the tissue surface, thereby transferring a customized pattern onto the tissue.

An extension of this concept involves a hybrid of the design in Fig. 2.14 and Fig. 2.13, in which a focused light beam is directed towards special dyes on a patterning film, which preferentially adheres to the tissue upon photoactivation. For example, a dye that photocrosslinks to tissue (e.g. Rose Bengal) upon irradiation[97] may be evaluated (in isolation or in conjunction with another dye) for this purpose. Yet another extension of this design involves the creation of microchannels or pores within the tissue using a focused laser beam (with a wavelength matching the absorption peak of water in the tissue or the dye) delivered through the light delivery fiber. Subsequent application of dyes such as methylene blue or the like (e.g., with a conventional spray catheter) would then preferentially seep into the microchannels, creating a custom pattern upon flushing the surface with water. Laser tattoos, which can be used repeatedly in longitudinal surveillance, can be created using this method. Similarly,

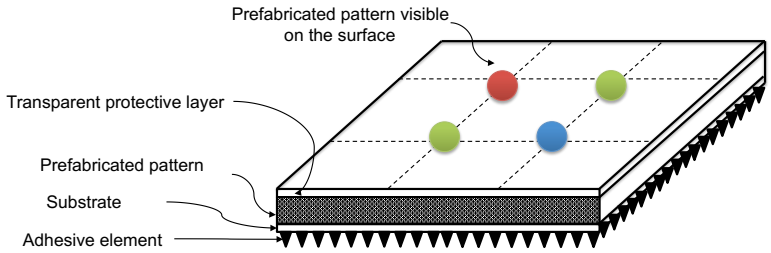

Figure 2.15: An example of a prefabricated pattern on a tissue adhesive film that is protected by a transparent layer and adheres to the tissue through adhesive elements such as microneedles.

the use of virtual chromoendoscopy techniques, such as narrow band imaging (NBI) and hyperspectral imaging, to enhance the contrast of the laser-marked patterns can be employed to avoid the use of stains, further decreasing the procedure time. Overall, the particular embodiment shown in Fig. 2.13 has the unique advantages of significantly reducing the power requirements for the light source, thereby enabling the use of a low-cost diode laser system, while enabling highly sophisticated patterns to be printed on the tissue surface.

In addition, the position-tracking pattern can be fabricated in advance on a flexible biocompatible substrate that provides strong adhesion to wet tissue surfaces (Fig. 2.15). This flexible substrate may contain an array of adhesive elements (such as soft, swellable microneedles[98]) that enable strong adhesion to wet tissue surfaces. The construct may further contain a series of windows or slots that enable tissue imaging and interventions (such as biopsy). The advantages of this embodiment include: 1) the ability to create a highly customized, multi-colored, high-resolution position-tracking pattern on a dry substrate; 2) the flexibility in the choice of suitable dyes and materials for the substrate; 3) the ability to further tailor the device to function as a durable construct for repeated, long-term use or a biodegradable construct for easy disposal in a single-use (or limited multi-session) setting.

2.7.2 Compact encoding scheme

One of the limitations observed in the evaluation of the current machine learning framework is that a better design of navigational landmarks is required. Figure 2.16 shows a potential solution to the design of a position tracking pattern that addresses several major challenges in endoscopy, including surface deformation, orientation and viewpoint changes. This tracking pattern employs a combination of a spatial encoding scheme and a color encoding scheme. In one of the simplest embodiments, a series of dots with different colors can form the corners of a grid. Each color represents a different location. This approach should suffice if the ROI is sufficiently limited in scope. In the more versatile embodiment, a spatial encoding scheme can be used, which comprises a location code (and optionally an orientation indicator to increase the number of combinations of possible location codes), inside a bounding element, which is surrounded by a set of calibration markers. The bounding element (or other elements of the tracking pattern) can be created with a different color to enable robust detection from a noisy background. Also, the calibration markers enable the correction of deformation or affine transformation, thereby improving the robustness in the location decoding process. The location code can comprise a set of elements that can serve as binary bit encoding (which greatly increases the number of combinations possible) or collectively as shape-based encoding. The neighboring patterns can further serve as error correction. In addition, the redundancy that can be achieved by combining the color encoding and spatial encoding schemes can improve the robustness of the algorithm.

2.8 Summary

In this chapter, we introduced the notion of enriching scenes in endoscopy through the generation of laser-marked or laser-printed navigational landmarks, as a first step towards general scene understanding in endoscopy. In particular, we investigated the problem of robust classification of artificially generated landmarks for navigational guidance in an endoscopic setting, which poses a set of unique chal-

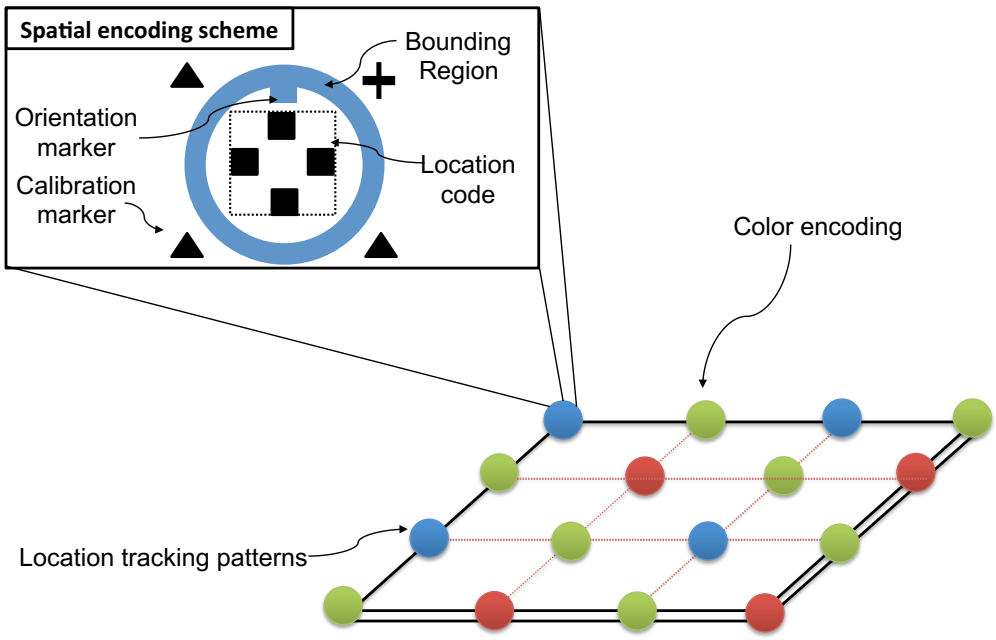

Figure 2.16: Spatial encoding pattern for navigational guidance and localization, which includes a location code inside a bounding region as well as orientation marker (and an optional calibration marker).

lenges including significant viewpoint changes, partial occlusion, deformation, and motion artifacts. To overcome these challenges, two variants of the bag of words model (orderless bag of words model vs. an ordered bag of words model using spatial pyramid representation) were explored. Surprisingly, a simpler approach based on the use of vectorized HOG descriptors and linear SVM demonstrated comparable performance to the more sophisticated bag of words models.

There are several limitations to the current framework as well as interesting possibilities for future work, including novel patterning catheter designs to enable laser painting *in vivo* as well as innovations in compact encoding schemes to address the specific challenges in endoscopy, as discussed in the previous section. The quantitative approach presented here serves as a framework for assessing the feasibility of new landmarks. In addition, strategies to further miniaturize these landmarks, while maintaining the accuracy for classification, would be beneficial. Finally, once the new compact encoding scheme is tested and optimized, a comprehensive localization algorithm is needed to solve the

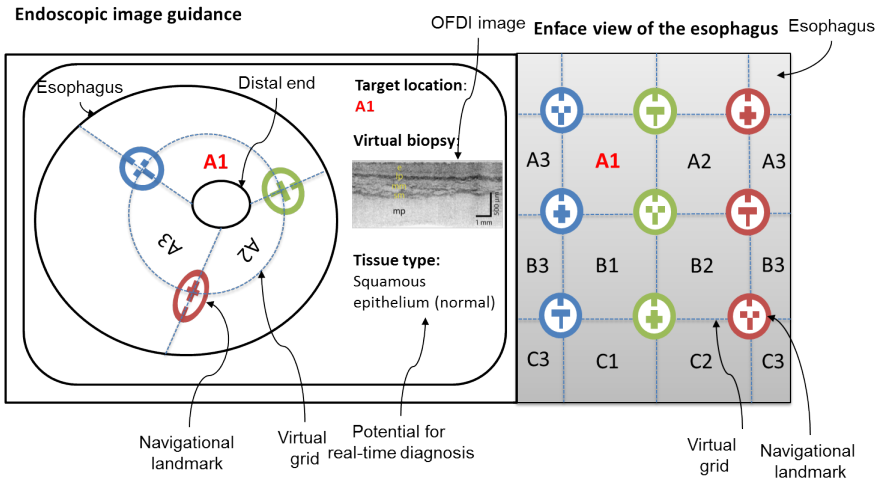

Figure 2.17: Endoscopic image guidance using laser-printed/painted navigational landmarks. Target locations can be identified by building a virtual grid from carefully laid out navigational landmarks, each of which encodes a specific location on the grid. The same grid of navigational landmarks is reconstructed in an enface view of the OFDI dataset to derive the OFDI image associated with a particular target location.

general navigational guidance problem. A potential scheme is illustrated in Fig. 2.17, which provides a comprehensive endoscopic image guidance system to accurately co-register the two modalities together.

While this work has focused primarily on artificially generated navigational landmarks, another interesting extension of this work is to investigate ways to reveal hidden intrinsic landmarks in endoscopy, potentially through the underlying blood vessel network that may be revealed through narrow band imaging. In addition, computer-assisted characterization and identification of common lesions would greatly facilitate the accurate assessment of disease progression through rapid re-identification of suspicious lesions in longitudinal surveillance program, which may benefit from a similar machine learning approach.

3

Laser thermal therapy monitoring using polarization-sensitive optical frequency domain imaging

In this chapter, we explore the feasibility and limitations of monitoring laser thermal therapy using polarization-sensitive optical frequency domain imaging (PS-OFDI). Specifically, we demonstrate the use of two metrics — local retardation and degree of polarization — for the delineation of the coagulation zone in the skin following thulium laser therapy and fractional ablation therapy, which is used as a common cosmetic laser procedure for rejuvenating photoaged skin and treating hypertrophic scars[5].

3.1 Background

Within the domain of optical coherence tomography (OCT), several early studies explored the use of polarization-sensitive OCT (PS-OCT) for the assessment of thermal damage directly[19,72]. In particular, reduced tissue birefringence was observed with PS-OCT in thermally damaged porcine skin or tendon due to the denaturation of collagen, which is consistent with earlier studies in thermally damaged myocardium[81] and rat tail tendon[56] using polarized light microscopy. PS-OCT was also shown to be useful for burn assessment in patients[66,45]. In addition, catheter-based PS-OCT was demonstrated for radiofrequency ablation monitoring in porcine myocardium *ex vivo*[29], following earlier observation of changes in birefringence bands between untreated and ablated myocardial tissue with intensity-based OCT[26,27,28]. Recently, depolarization (in addition to linear retardance) was investigated to visualize radiofrequency-ablated myocardial tissue *ex vivo* using Mueller matrix polarimetry in a backscattered geometry[2]. In this chapter, we focus on the use of local retardation (which is a much more intuitive metric to interpret than cumulative retardation typically used in the literature) and degree of polarization to delineate the coagulation zone. The information is merged with intensity OCT images to provide intuitive visualization of the coagulation process.

3.2 Experimental Setup and Reconstruction of PS Data

Figure 3.1 provides an overview of the polarization-sensitive optical frequency domain imaging system used in this study, which modulates the polarization state of the light between linear and circular polarization in consecutive A-lines through the use of an electro-optic modulator.

Reconstruction of the PS-OFDI data using the spectral binning algorithm[91] yields the local retardation and degree of polarization, respectively. Local retardation expresses the rate of change of the

measured polarization states with depth z and is a direct, local measure of tissue birefringence:

$$s(z+\delta z) = \mathcal{M}_{loc}(z)s_{in}(z-\delta z) \tag{3.1}$$

where $s_{in}(z-\delta z)$ is the input Stokes vector at a depth $z-\delta z$, $\mathcal{M}_{loc}(z)$ is the Mueller matrix at depth z containing the local phase retardation, and $s(z+\delta z)$ is the Stokes vector at depth $z+\delta z$. It is a more intuitive metric for visualizing the local changes in tissue birefringence as a function of depth, compared to the more commonly used cumulative retardation metric in the literature.

Degree of polarization (DOP) is a measure related to the randomness of the detected polarization states of light. It scales from zero for completely random to unity for perfectly uniform polarization states. Unlike local retardation, DOP captures the cumulative effect of the tissue from the surface to a given depth on the polarization states of light.

Reconstruction of the DOP is performed with the spectral binning algorithm[91] as follows:

$$DOP = \frac{1}{2N}\sum_{p=1}^{2}\sum_{n=1}^{N}\frac{\sqrt{Q_{p,n}^2+U_{p,n}^2+V_{p,n}^2}}{I_{p,n}} \tag{3.2}$$

where Q,U,V, and I are the spatially averaged, but unnormalized components of the Stokes vector, p denotes the input polarization states, and n denotes the spectral bin.

3.3 Thulium laser therapy monitoring

Figure 3.2 depicts the use of polarization-sensitive optical frequency domain imaging (PS-OFDI) to monitor the thermal coagulation process during laser thermal therapy in the skin. In this experiment, a wavelength-tunable thulium laser therapy beam (tuned to the water absorption peak at 1890 nm) was incident on a piece of porcine skin *ex vivo* at a 45 degree angle and PS-OFDI imaging was performed across the center of the beam longitudinally for 10 s. In particular, the thermal coagulation zone is

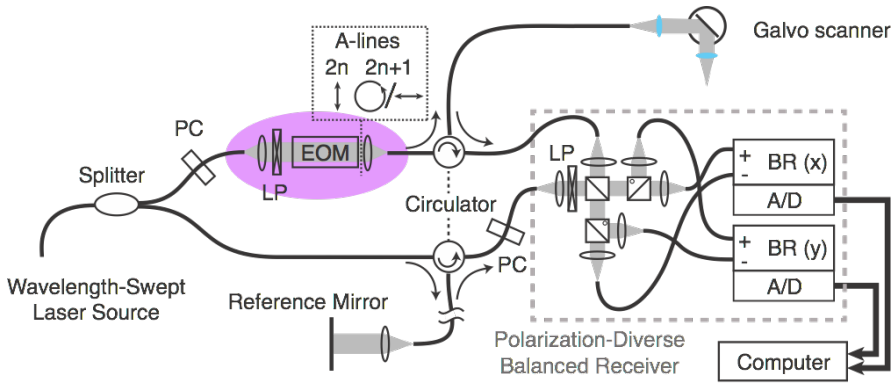

Figure 3.1: Overview of polarization-sensitive optical frequency domain imaging (PS-OFDI) system [91]. The polarization state of the light is modulated between A-lines (linear and circular polarization) using an electro-optic modulator (EOM). PC, polarization controller; LP, linear polarizer; AOM, acousto-optic modulator.

clearly demarcated by a region with decreased local retardation (low LR, yellow) and increased degree of polarization (high DOP, purple), in a background with heterogeneous LR and low DOP in the dermis of normal, uncoagulated skin. Histologically, the decreased LR corresponds very well with the denaturation of collagen (as shown in Fig. 3.3 in a different specimen where ink marks were placed around the thermal lesion for co-registration), which decreases the tissue birefringence measured given the loss of the fibrillar architecture of collagen upon coagulation. This provides intrinsic, contrast-free visualization of the coagulation process to precisely tailor the therapy depth in numerous dermatology applications.

3.4 Fractional ablation therapy monitoring

To test the utility of PS-OFDI for monitoring laser therapy in dermatology applications further, a series of thermal lesions, with increasing pulse energy from 10 mJ/pulse to 50 mJ/pulse (at a density of 10%), were created using a clinical fractional ablation system, which is commonly used in the treatment of photoaged skin and hypertrophic scars[5]. In particular, the feasibility of using PS-OFDI to evaluate the microchannel depth during fractional laser ablation was demonstrated (Figure 3.4). With increas-

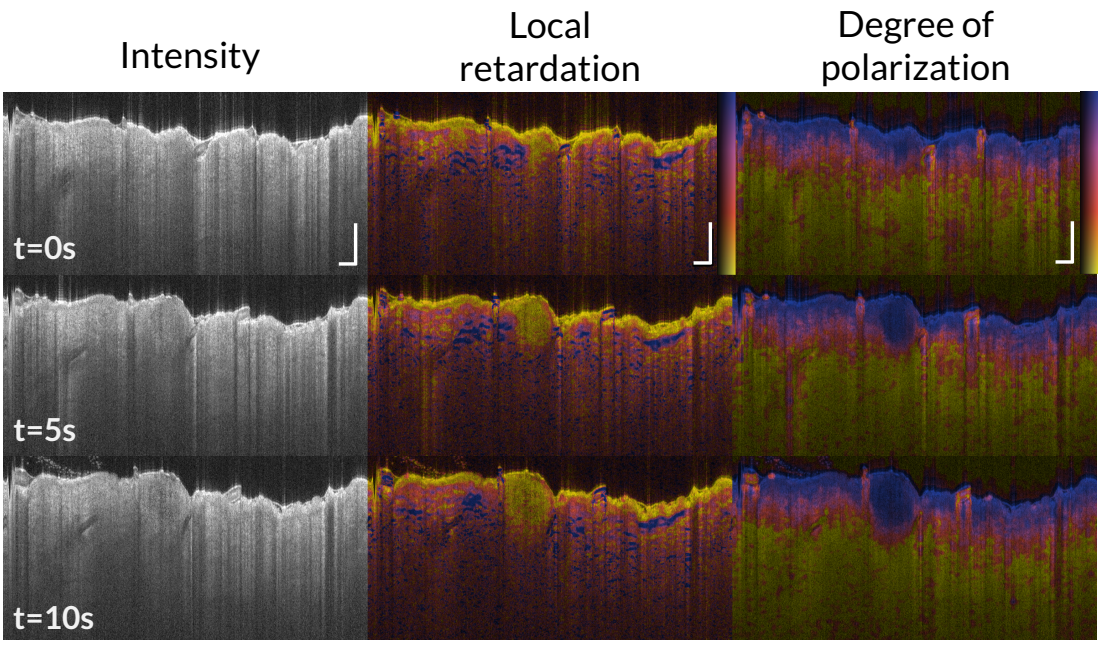

Figure 3.2: Cross-sectional (2-D) monitoring of laser therapy in porcine skin *ex vivo* using PS-OFDI. A therapy beam (300 mW, 1890 nm thulium fiber laser) was incident on the skin surface and cross-sectional PS-OFDI imaging was performed at the same location for 10 seconds. Colorbars range from 0-1.2 deg/μm for PS-LR and 0.5-1 for PS-DOP images, respectively. Scale bars = 500 μm.

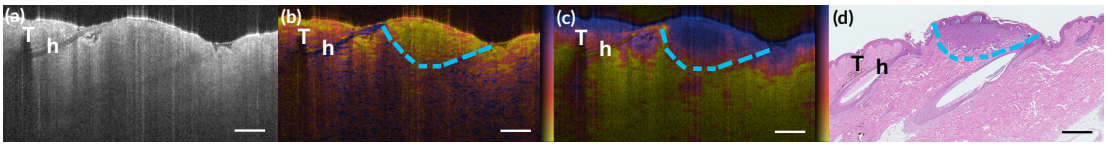

Figure 3.3: Histological validation of PS local retardation (PS-LR) image (b) and PS degree of polarization (PS-DOP) image (c) with H&E histology (d) in porcine skin (300mW, 1890nm, 10s), demonstrating that the region with reduced LR and increased DOP corresponds very well with the region with denatured collagen in H&E. The intensity OCT image (a) is provided for comparison. T, tattoo ink marks for co-registration of histology; h, hair. Dotted blue line, coagulation zone. Colorbars range from 0-1.2 deg/μm for PS-LR and 0.5-1 for PS-DOP images, respectively. Scale bars = 500 μm.

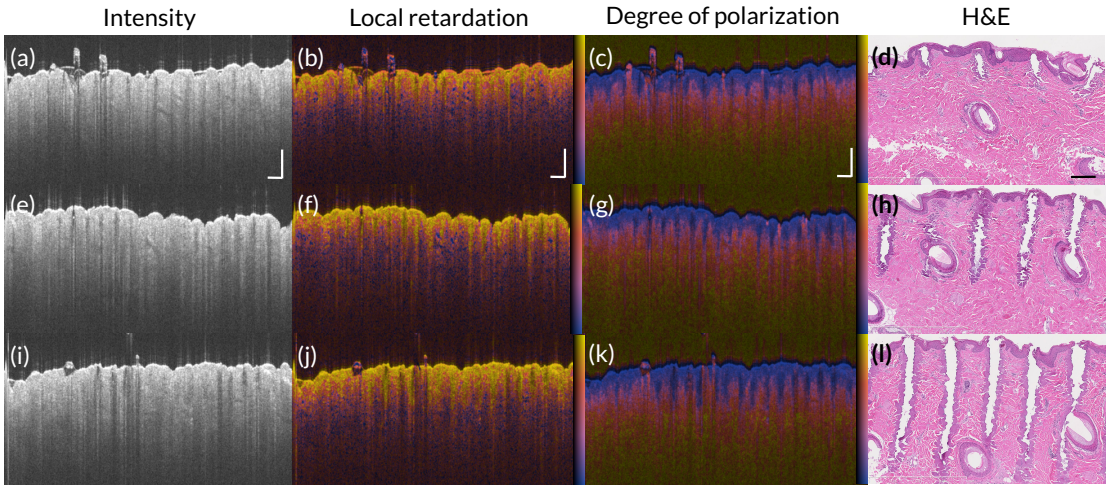

Figure 3.4: Fractional laser ablation monitoring using PS-OFDI and histological validation of microchannel depth in porcine skin *ex vivo*. While conventional intensity OFDI images (a, e, i) do not clearly delineate the microchannels, the local retardation (d, f, j) and degree of polarization (c, g, k) images clearly demarcate the depth of the microchannels, as validated with H&E histology (d, h,l). 10mJ/pulse, 10% density (a, b, c, d); 25mJ/pulse, 10% density (e, f, g, h); 50mJ/pulse, 10% density (i, j, k, l). Colorbars range from 0-1.2 deg/μm for PS-LR and 0.5-1 for PS-DOP images, respectively. Scale bars = 500 μm (a,b,c,e,f,g,i,j,k), 250 μm (d,h,l).

ing pulse energy, there were growing regions (microchannels) with reduced LR and increased DOP, which were not evident in intensity OCT. These regions corresponded well with the microchannels seen in H&E histology (Note the different scales in these images). Such observations suggest a potential role for using PS-OFDI in the treatment of different skin lesions with fractional ablation by optimizing the treatment parameters to better conform to the geometry of the lesion and visualizing the achieved treatment depth noninvasively in patients.

3.5 Limitations of the PS-based approach

Finally, we test the limitations of the PS-based approach for monitoring thermal coagulation in other tissues types with low birefringence at baseline. Figure 3.5 demonstrates cross-sectional monitoring of the laser thermal therapy zone in porcine esophagus *ex vivo*. In this case, the evolution of the thermal coagulation process was not readily visible due to the low baseline tissue birefringence (low LR in

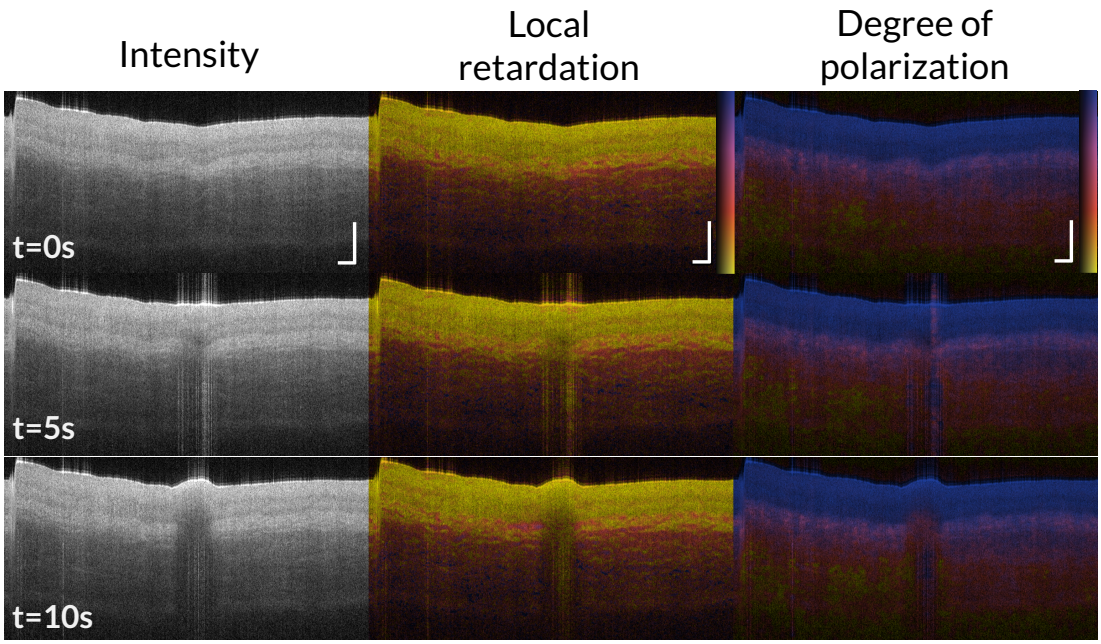

Figure 3.5: Cross-sectional (2-D) monitoring of laser therapy in porcine esophagus *ex vivo* (300mW) using PS-OFDI. A therapy beam (300 mW, 1890 nm thulium fiber laser) was incident on the surface of the esophagus and cross-sectional PS-OFDI imaging was performed at the same location for 10 seconds. Colorbars range from 0-1.2 deg/μm for PS-LR and 0.5-1 for PS-DOP images, respectively. Scale bars = 500 μm.

yellow) in the epithelium of the esophagus. The DOP is also quite high in the epithelium , preventing the use of either metric for the clear delineation of the thermal coagulation zone, unlike in the case of the skin where either metric provides a good estimate of the thermal coagulation boundary.

3.6 Summary

In this chapter, we demonstrated the utility of the PS-based approach for monitoring the evolution of the thermal coagulation zone during laser thermal therapy. In particular, the growing thermal coagulation zone is characterized by its decreased local retardation (due to the loss of tissue birefringence upon thermal coagulation) and increased degree of polarization, which provides a means to monitor lesions in the skin given its relatively high tissue birefringence induced by the abundance of fibrillar

collagen in the dermis at baseline. The ability to clearly delineate the coagulation zone at high resolution in the skin enables treatment monitoring in numerous laser procedures, including ablative or nonablative fractional laser therapy, which is commonly used in the treatment of various skin lesions such as hypertrophic scars. The primary advantage of the PS-based approach is the ability to monitor the treatment progress either in real-time (during the procedure) or postoperatively (before and after the procedure given the persistence of the PS signals upon thermal coagulation). In addition, we demonstrated the limitations of this approach for other tissue types such as the esophagus which exhibits relatively low tissue birefrigence especially in the epithelium. This major limitation prevents the use of PS-based approaches for determining injury depth accurately in diverse tissue types, which motivates the development of a generic framework for thermal therapy monitoring as discussed in detail in Chapter 5.

In the next chapter, we will further explore the use of PS-OFDI for the longitudinal, 3D monitoring of hypertrophic scars *in vivo* given its ability to probe the collagen remodeling process noninvasively. Together with the laser therapy monitoring approach discussed in this chapter and Chapter 5, we envision the possibility of more integrated therapy monitoring and longitudinal assessment of scars to improve treatment outcomes in patients.

4

Longitudinal, 3D imaging of hypertrophic scars *in vivo* using PS-OFDI

Hypertrophic scars (HTS), frequently seen after traumatic injuries and surgery, remain a major clinical challenge due to the limited success of existing therapies. A significant obstacle to understanding HTS etiology is the lack of tools to monitor scar remodeling longitudinally and non-invasively. In this chapter, we present a label-free technique, using polarization-sensitive optical frequency domain imaging (PS-OFDI), for the 3D, longitudinal assessment of collagen remodeling *in vivo* in a murine HTS model. In this study, HTS was induced with a mechanical tension device for 4 to 10 days on incisional wounds and imaged up to one month after device removal; an excisional HTS model was also

imaged at 6 months after injury to investigate deeper and more mature scars. We showed that local retardation (LR) and degree of polarization (DOP) provide a robust signature for HTS. Compared to normal skin with heterogeneous LR and low DOP, HTS was characterized by an initially low LR, which increased as collagen fibers remodeled, and a persistently high DOP. This study demonstrates that PS-OFDI offers a powerful tool to gain significant biological insights into HTS remodeling by enabling longitudinal assessment of collagen *in vivo*, which is critical to elucidating HTS etiology and developing more effective HTS therapies.

4.1 Introduction

Hypertrophic scars (HTS) are conspicuous, potentially disfiguring lesions that remain a major therapeutic challenge. In fact, its incidence following surgery in burn injury is particularly high (>90%)[31]. Apart from the cosmetic disfigurement, HTS frequently recur and can cause pruritus, pain, functional impairment, and profound psychological effects.

The pathogenesis of HTS is not fully understood. Its formation typically involves an abnormal wound healing response to trauma, such as burns, inflammation, or surgery, especially when the wound crosses joints or skin creases at right angles[96]. Among other factors, tension is known to be critical to the formation of HTS and indeed, the well-established surgical treatment — Z-plasty or W-plasty[25] — works by relieving tension along the scar. Decreased cellular apoptosis was observed in murine models in which mechanical stress was applied to healing wounds[1]. In addition, overproduction of TGF-β and PDGF suggest the pathologic persistence of wound healing signals (TGF-β1 and β2 stimulate collagen synthesis) in HTS[31]. Histologically, hypertrophic scars are characterized by the presence of nodular structures with fine, randomly organized collagen bundles[23].

To understand scar etiology and assess treatment outcome, imaging is needed. Several imaging techniques have been investigated to assess collagen *ex vivo* and *in vivo*. Historically, picrosirius red

staining with polarization microscopy, which enhances tissue birefringence[42], has been used to visualize collagen *ex vivo*. More recently, second-harmonic generation and two-photon excited fluorescence techniques have been used to analyze collagen and elastin, respectively, in HTS and keloid specimens *ex vivo*[15,92]. Unfortunately, these techniques only offer a limited field of view and are challenging to use *in vivo*. Optical coherence tomography (OCT) offers fast imaging speed and increased field of view and imaging depth at a spatial resolution suitable for biological applications, which makes it particularly amenable to imaging *in vivo*. OCT has been investigated for the imaging of skin[3,30], and in particular for the imaging of burn scars[33] and skin cancer[59].

Polarization-sensitive OCT (PS-OCT) is an extension of OCT that measures the polarization state as well as the intensity of the light backscattered by the sample. It enables the measurement of tissue birefringence, primarily caused by fibrillar collagen, in the skin. PS-OCT has been shown to provide intrinsic contrast in thermally damaged tissue, thereby providing a tool for burn depth assessment[19,64,67,66] and mapping of dermal birefringence in photoaged skin[71] *in vivo*.

In this study, we present the use of polarization-sensitive optical frequency domain imaging (PS-OFDI), a variant of PS-OCT which offers improved imaging speed and sensitivity[91], for the 3D imaging of a rat model of surgical HTS *in vivo*. This animal model employs a mechanical tension device placed on healing incisional wounds, which enables the systematic study of HTS formation[1]. To validate PS-OFDI in imaging deeper scars, we also investigated an excisional wound scar placed under autologous tension, imaged at 6 months after injury. We evaluate both local retardation (LR) and degree of polarization (DOP), computed using our spectral binning algorithm[91], for enhancing the contrast of HTS, which, to the best of our knowledge, has not been reported previously. Compared to cumulative retardation, LR expresses the rate of change of the measured polarization states with depth, and is a direct, more intuitive measure of tissue birefringence. DOP is a quantity related to the randomness of the detected polarization states of light, which scales from zero for completely random to unity for perfectly uniform polarization states. Unlike local retardation, DOP captures the cumu-

lative effect of the tissue from the surface to a given depth. We observed that the combination of LR and DOP provides a robust optical signature to differentiate HTS given the presence of fine, densely packed collagen bundles in HTS compared to thicker collagen bundles in normal skin.

In addition, we demonstrate the use of PS-OFDI for studying HTS remodeling by imaging the incisional wound model longitudinally for 1 month and the excisional model at 6 months. Interestingly, we observed a progressive increase in LR and a persistently high DOP within the scar region over time, which corresponded well with the remodeling and thickening of collagen fibers histologically. Normalization of the scar was associated with an increased LR and decreased DOP back to baseline levels in normal skin. Our findings suggest that PS-OFDI can serve as a valuable 3D imaging tool for the non-invasive, longitudinal assessment of HTS *in vivo*, by providing significant biological insights into collagen remodeling central to understanding HTS etiology and monitoring therapeutic response to improve current therapies and investigate novel approaches.

4.2 Materials and Methods

4.2.1 Animals

6-week old female Sprague-Dawley rats (~200g, N=18) were purchased from Charles River Laboratories (Wilmington, MA). The animals were housed in individual cages with access to food and water ad libitum, and were maintained on a 12-hour light/dark cycle in a temperature-controlled room. All animal procedures were approved by the Subcommittee on Research Animal Care (IACUC) of the Massachusetts General Hospital (protocol number 2012N000077) and were in accordance with the guidelines of the National Institutes of Health (NIH).

Tension-induced surgical HTS model in rat

A biomechanical loading device was constructed from 22-mm expansion screws and metal supports, which allows the device to be placed over a healing incision without contacting the wound. The procedure was developed based on a previous report from Aarabi et al[1]. After the induction of anesthesia with isoflurane, two 2 cm linear full-thickness incisions were made on the dorsum (5 cm apart; one at the cranial end and another at the caudal end) and then reapproximated with three 4-0 vicryl sutures. On post-incision day 4, the sutures were removed from the healing incisions, and the loading device was carefully secured with 6-0 nylon sutures on one of the incisions. The second incision served as a control. Tension on the wound was created by translating the expansion screws by 2 mm at the time of securing the loading device, and 2 mm every day thereafter. This was necessary to prevent stress relaxation due to the natural elongation of the skin resulting in a decrease in the tension on wounds. At the end of the loading period (4 days, 6 days, 8 days or 10 days), the device was removed and the scar was imaged 1 month later (or at 1-week intervals for the longitudinal study).

Excisional HTS model in rat

A 2.5cm x 2cm full-thickness excisional wound was created on the mid dorsum. The lax skin flanking the wound was gathered with a running 4-0 vicryl suture to create tension. On each side of the wound, excess skin was gathered in a running fashion starting at the cephelic aspect, down to the caudal aspect, and back up to the cephalic end. The length of the gathered skin was the length of the wound created (2.5cm). The small ridge of skin produced was tacked down laterally. This was performed on each side of the wound to secure the tension. A small piece of gauze and Tegaderm were placed over the wound. The sutures were left until reabsorbed ($\sim$2 weeks after excision). 0.05 mg/kg of buprenorphine was administered subcutaneously every 12h up to 72h after excision.

4.2.2 Immunohistochemistry

Ki67/SMA double staining was achieved by an indirect sequential immunoenzymatic technique. Heat-induced antigen retrieval was performed on 5-μm thick formalin-fixed paraffin-embedded tissue sections after deparaffinization with Borg Decloaker (BioCare Medical, Concord, CA) for 15 min, followed by Dual Endogenous Enzyme Block (DAKO, Glostrup, Denmark) for 5 min. The tissue sections were incubated with monoclonal mouse anti-rat Ki-67 antibody (Clone MIB-5, dilution 1:50; DAKO, Glostrup, Denmark) overnight at 4 °C. Biotinylated rabbit anti-mouse IgG1 (dilution 1:200, Vector Laboratories, Burlingame, CA) was applied for 35 min, followed by detection using Streptavidin/HRP and DAB. Next, after double stain block (DAKO, Glostrup, Denmark), the tissue sections were incubated with monoclonal mouse alpha smooth muscle actin antibody (Clone 1A4, dilution 1:100; DAKO, Glostrup, Denmark) overnight at 4 °C. Biotinylated horse anti-mouse IgG (rat adsorbed, dilution 1:200; Vector Laboratories, Burlingame, CA) was applied for 35 min, followed by detection using the VectaStain ABC-AP and Vector Blue AP kits (Vector Laboratories, Burlingame, CA).

4.2.3 Herovici's staining

Herovici's picropolychrome staining[38] was performed on 5-μm thick formalin-fixed paraffin-embedded tissue sections, which stains more mature, highly cross-linked collagen red/purple, and newly formed, fine fibrillar collagen or extracellular matrix components blue. Briefly, tissue sections were deparaffinized with Xylene and hydrated with ethanol, followed by Weigert's iron hematoxylin for 10 min. After rinsing with tap water, slides were placed in 50mL van Gieson's solution, 50mL 0.05% methyl blue, 10 mL 100% glycerol, and 0.5 mL lithium carbonate solution for 2 min, followed by 1% acetic acid for 2 min. The slides were then dehydrated with ethanol, cleared with xylene, and mounted with permanent mounting media.

4.2.4 PS-OFDI System

The PS-OFDI system used in this study has been reported in detail previously[91]. A wavelength-swept laser source operating at a center wavelength of 1320nm with an axial resolution of 9.4 μm in air was used. The A-line rate was 54 kHz (1536 samples per A-line) and the signal was digitized at 85 MHz. In the reference arm, an acousto-optic modulator was used to remove depth-degeneracy[100]. An imaging window of 10 x 5 mm, consisting of 2048 A-lines/image x 256 images, was scanned with a focused beam featuring a $1/e^2$ intensity diameter of 15 μm. The skin was apposed against a glass slide with ultrasound gel as immersion medium to center the superficial layers in focus. The polarization state of the input light was modulated between circular and linear polarization between adjacent A-lines, and the signal was detected with a polarization diverse receiver.

Reconstruction of the PS data was performed with spectral binning[91], using 1/5th of the original spectral bandwidth (i.e. 9 overlapping spectral bins), a lateral Gaussian filter of a full width at half maximum (FWHM) equal to 12 adjacent A-lines, and an axial offset of 48 μm to derive the local retardation. The DOP was evaluated independently for each spectral bin and input polarization state over the same lateral Gaussian kernel, and then averaged:

$$DOP = \frac{1}{2N}\sum_{p=1}^{2}\sum_{n=1}^{N}\frac{\sqrt{Q_{p,n}^2 + U_{p,n}^2 + V_{p,n}^2}}{I_{p,n}} \tag{4.1}$$

where Q,U,V and I are the spatially averaged, but un-normalized components of the Stokes vector, p denotes the input polarization states and n the spectral bin.

4.3 Results

4.3.1 Imaging aberrant collagen organization in hypertrophic scars using PS-OFDI

Figure 4.1 shows the cross-sectional PS-OFDI images of a mechanical tension-induced hypertrophic scar (HTS) after 10 days of loading (imaged 1 month later) compared to normal rat skin. For intuitive visualization, the LR and DOP signals were merged with the intensity image (as a brightness channel) and displayed using an isoluminant colormap[32]. While conventional intensity images show minimal contrast (only slightly increased back-scattering), the local retardation (PS-LR) and degree of polarization (PS-DOP) images demonstrate significant differences in HTS compared to normal skin. HTS shows significantly reduced LR and increased DOP deep inside the dermis, compared to heterogeneous LR and low DOP beyond the epidermis in normal skin. This optical signature (reduced LR and high DOP) corresponds histologically to thin, less organized collagen bundles in HTS (Fig. 4.1d), compared to thicker collagen bundles in normal skin (Fig. 4.1h). These abnormal collagen bundles are cigar-shaped and orientated parallel to the surface of the skin along the tension lines of the scar tissue (Fig. 4.1d). In addition, there is an increased cellularity of fibroblasts in HTS compared to normal skin (Fig. 4.1d and 4.1h).

4.3.2 Histological correlation

We further analyzed the histological correlation of the PS-OFDI images in each animal group with varying duration of tension (Fig. 4.2). In all cases, the scar region shows reduced LR and increased DOP. Overall, the PS-DOP images correlate well with the extent and shape of the scar as confirmed by H&E histology (Fig. 4.2c, f, i, l), while the PS-LR images show more variability. The size of HTS also increased with the duration of tension, as expected, from a barely noticeable scar with minimal

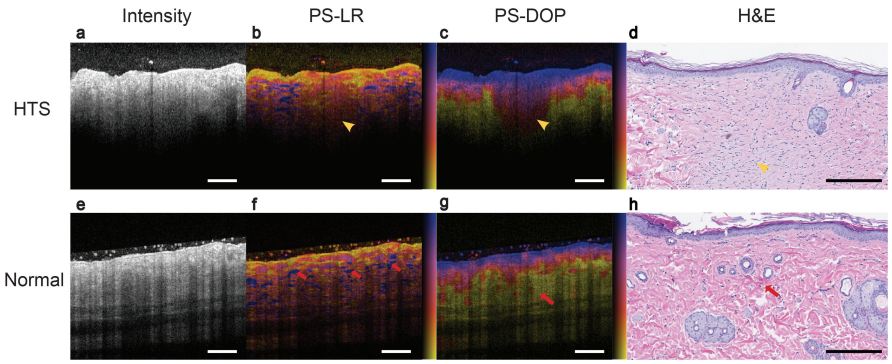

Figure 4.1: Visualization of tension-induced HTS and normal skin *in vivo* using PS-OFDI (10-day group). Intensity (a,e), local retardation (LR) (b,f), degree of polarization (DOP) (c,g) images and corresponding H&E histology (d,h) are shown for HTS (a-d) and normal skin (e-h). HTS exhibits reduced LR ($\sim$0.3 deg/μm in the region indicated by yellow arrowheads) and high DOP (1.0) corresponding to thin, densely packed collagen fibers (d), while normal skin contains islands of high LR ($\sim$0.8 deg/μm in regions indicated by red arrows) and generally low DOP ($\sim$0.3-0.5) in the dermis corresponding to thick, mature, more loosely distributed collagen (h). Color bars range from 0-1.2 deg/μm for PS-LR and 0.5-1 for PS-DOP images, respectively. Scale bars = 500 μm (a-c, e-g), 250 μm (d,h).

deposition of collagen in the 4-day group (Fig. 4.2c) to a significantly larger scar extending all the way through the dermis that is characterized by aberrant collagen bundles and increased cellularity of dermal fibroblasts in the 10-day group (Fig. 4.2l).

4.3.3 Longitudinal, 3D imaging of HTS *in vivo*

A major advantage of using PS-OFDI, compared to conventional histology processing, is the ability to assess HTS longitudinally and comprehensively *in vivo* (Fig. 4.3), which is particularly important for studying HTS etiology and assessing response. By imaging the incisional HTS model (6-day group) at 1-week intervals post device removal, we observed rapid contraction of the scar in the first week, as indicated by the normalization of DOP and LR around the boundary of the scar to baseline levels in normal skin (increased LR and decreased DOP). From weeks 1 to 4, the scar continued to remodel progressively, leading to further reduction in scar size and an interesting increase in LR, particularly in deeper regions. The DOP remained persistently high within the scar region. To investigate the evolution of the LR and DOP signals further, we analyzed the PS-LR and PS-DOP images at three major

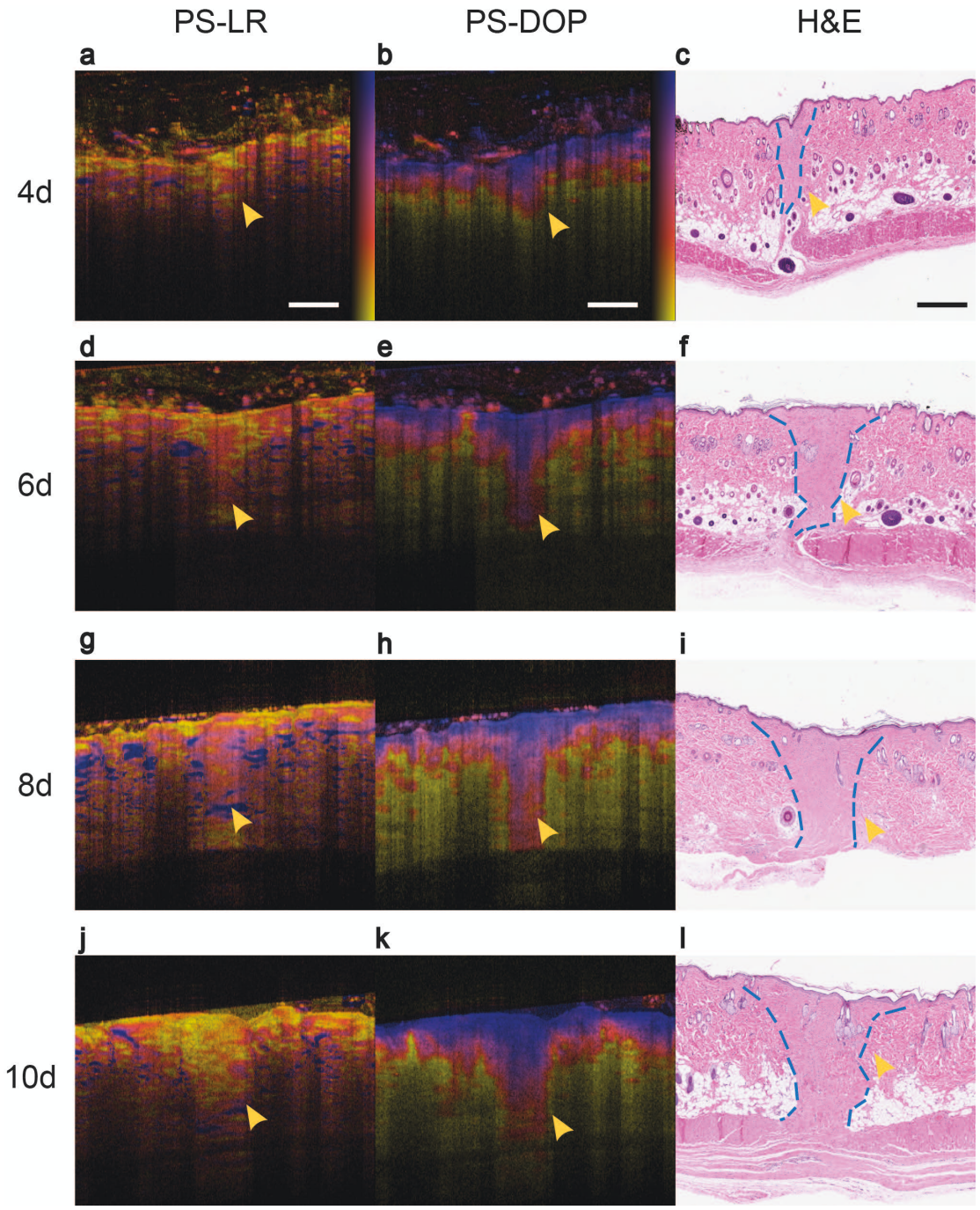

Figure 4.2: Histological correlation of PS-OFDI images in 4 day (a, b, c), 6 day (d, e, f), 8 day (g, h, i), and 10 day (j,k,l) groups. (a,d,g,j) PS-LR images, (b,e,h,k) PS-DOP images, and (c,f,i,l) H&E histology. Each animal was tattooed with a set of ink marks around the scar for co-registration. Yellow arrowheads, scar region. Dotted blue lines, scar area on H&E. Color bars range from 0-1.2 deg/μm for PS-LR and 0.5-1 for PS-DOP images, respectively. Scale bars = 500 μm.

time points (Fig. 4.4). After the initial incision (and prior to the application of tension), the fresh incisional wound (at day 2) was marked by a small region with very low LR and high DOP (Fig. 4.4a, b), which expanded significantly after loading the healing incision for 8 days (Fig. 4.4c, d). As the tension-induced wound continued to remodel over the 1-month period, LR increased significantly while DOP remained high (Fig. 4.4e, f). Finally, we analyzed the relative maturity of the collagen using Herovici's method[38], which has been shown and used to distinguish young, newly formed collagen (blue) from more mature, highly cross-linked collagen (purple/red) in previous studies[47,50,63,84]. As shown by Herovici's staining and Ki67/SMA staining, the change in LR over the 1-month period corresponded well with the transition from a scar with thin, newly formed (blue) collagen and myofibroblasts at week 0 to thicker, more mature (purple) collagen bundles with decreased cellularity at week 4 (Fig. 4.5).

4.3.4 Imaging a mature excisional HTS model *in vivo*

To demonstrate the clinical utility of our approach in imaging deeper full-thickness scars, we performed our imaging experiments in an excisional wound 6 months after the injury. Interestingly, we observed a much more prominent increase in LR deep in the dermis at 6 months (Fig. 4.6a), which corresponds well with more organized, thicker collagen fibers deep in the dermis with decreased cellularity (Fig. 4.6e), compared to thinner and less organized collagen fibers surrounded by a high density of fibroblasts in the HTS region closer to the epidermis with a lower LR (Fig. 4.6d). In both cases, the DOP within the scar remained significantly higher than in normal skin (Fig. 4.6b).

4.4 Discussion

This study demonstrated the use of PS-OFDI for 3D, label-free imaging of murine models of HTS, thereby enabling non-invasive, quantitative evaluation of scar remodeling longitudinally. Interest-

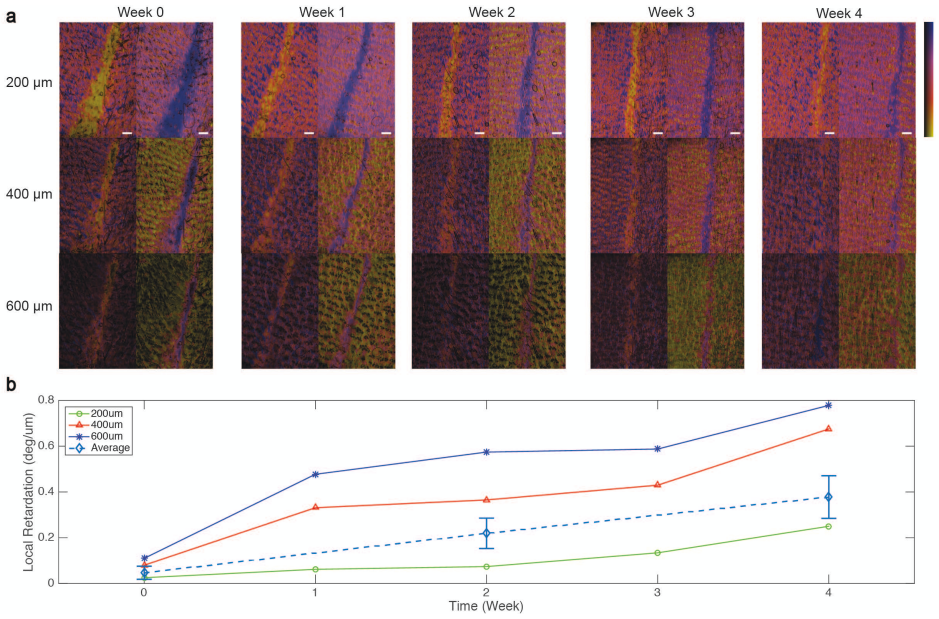

Figure 4.3: Longitudinal imaging of tension-induced HTS model for 1 month post tension device removal, showing rapid scar remodeling from weeks 0 to 1, followed by a more progressive phase from weeks 1 to 4. (a) Left column: PS-LR images, Right column: PS-DOP images at each time point. Images represent enface average intensity projection across a 100 μm section at indicated depths. Color bars range from 0-1.2 deg/μm for PS-LR and 0.5-1 for PS-DOP images, respectively. Scale bars = 500 μm. (b) As the collagen fibers remodeled, LR increased progressively at each depth, particularly in deeper regions, while DOP remained high. The average local retardation (n=3 animals), computed in cross-sectional slices covering the entire scar, showed a similar trend. Values represent the mean +/- SD.

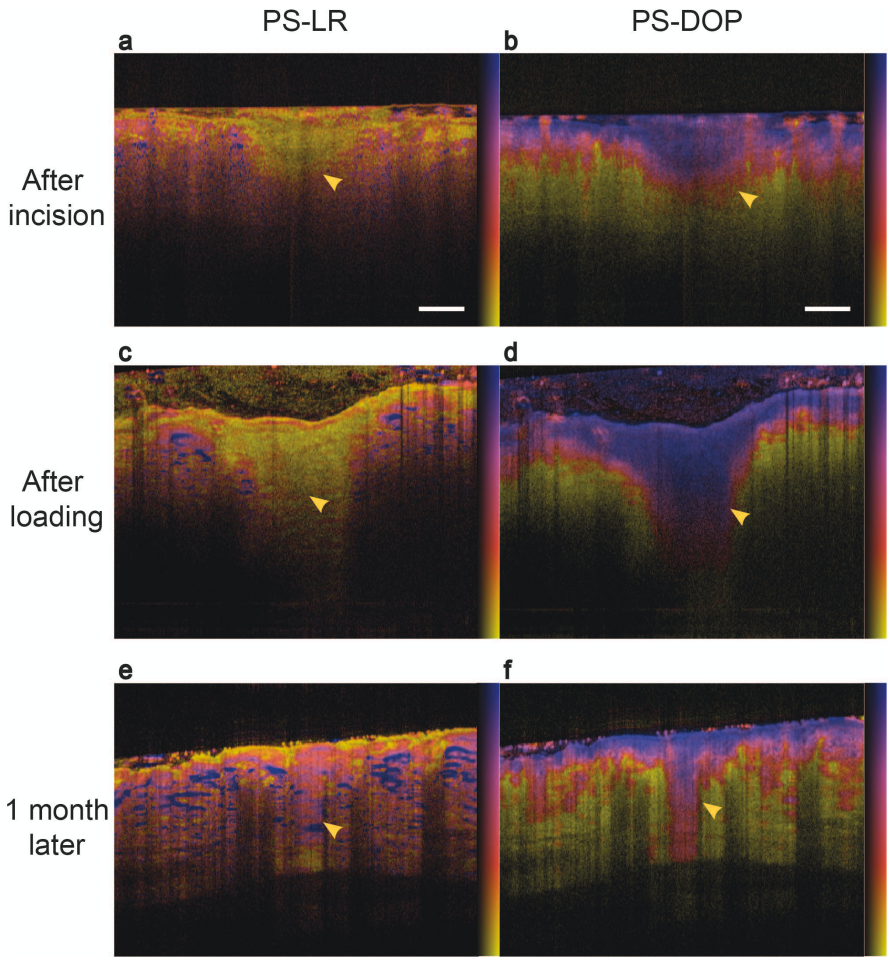

Figure 4.4: Cross-sectional PS-LR and PS-DOP images at major time points providing insights into collagen remodeling during wound healing: before tension loading (a, b), after tension loading (c, d), and 1 month after tension device removal (e, f). Tension loading led to rapid expansion of scar compared to the initial unloaded incisional wound, as revealed by the region (yellow arrowheads) with extremely low LR and high DOP (After incision: LR=0.03 deg/μm, DOP=1.0; after loading: LR=0.08 deg/μm, DOP=1.0). As the tension-loaded incisional wound healed over the 1-month period, the scar region was marked by increased LR ($\sim$0.4 deg/μm) and high DOP (0.98). Color bars range from 0-1.2 deg/μm for PS-LR and 0.5-1 for PS-DOP images, respectively. Scale bars = 500 μm.

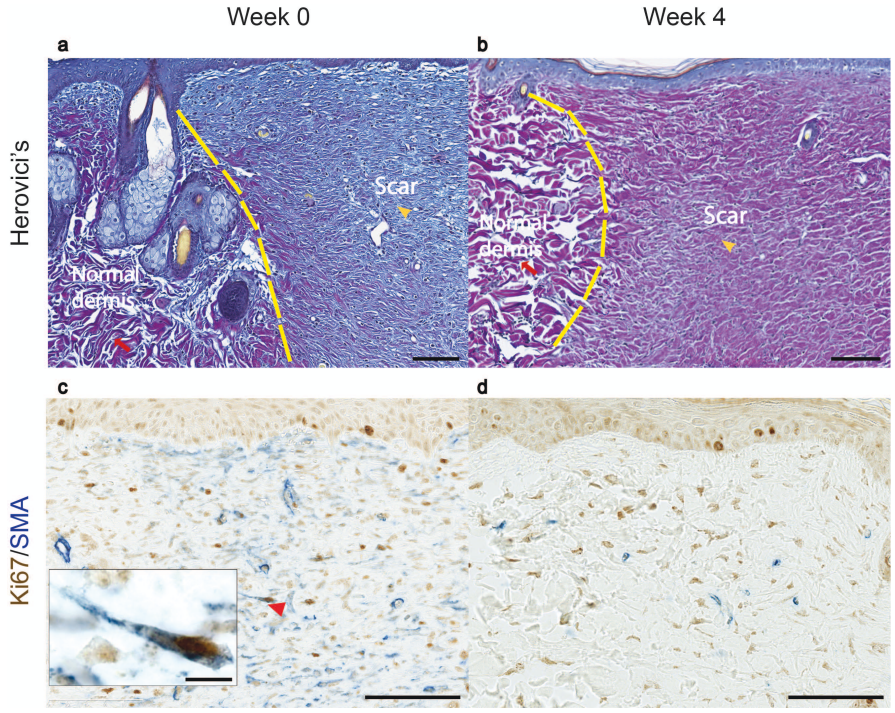

Figure 4.5: Histology of HTS immediately after tension loading (a, c) and 1 month after device removal (b, d), showing significant collagen remodeling within the scar tissue. At week 0, immediately after tension loading, the incisional wound contained an abundance of thin, newly formed collagen (blue), compared to surrounding normal skin with thicker, more mature collagen (purple), as indicated by Herovici's staining (a), as well as proliferating myofibroblasts (Ki67/SMA+, see insert) (c), indicating a phase of acute tissue reaction. At week 4, the scar region transitioned to more mature, thicker collagen (b), and a significantly lower density of fibroblasts (with decreased SMA and Ki67 positivity) (d). A representative section is shown at each time point. Scale bars = 100 μm (10 μm in insert). Yellow arrowheads, scar region; red arrows, normal dermis (a, b). Red arrowhead, Ki67/SMA+ myofibroblast shown in insert (c). Ki67, brown; SMA, blue (c, d).

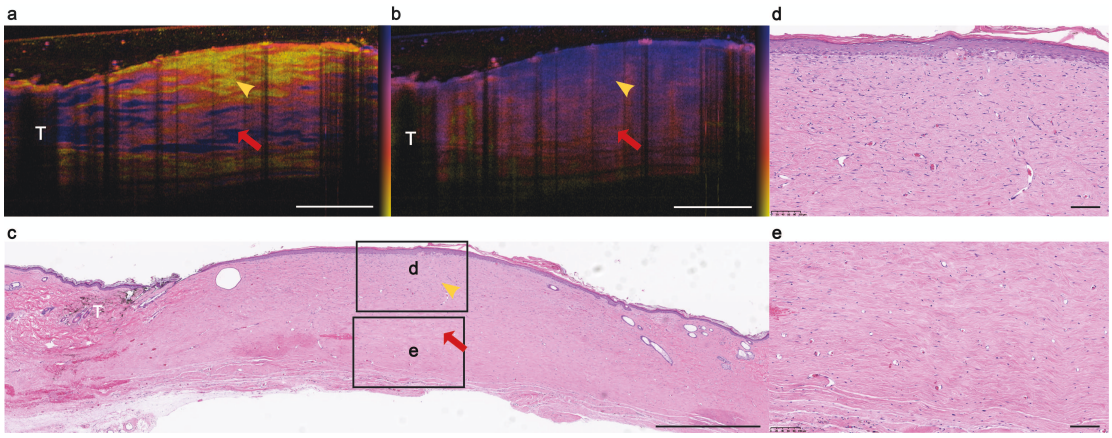

Figure 4.6: Excisional HTS model imaged 6 months after injury with PS-OFDI, demonstrating the ability to probe collagen remodeling non-invasively over long periods of time in deeper scars. The top region with low LR [0.2 deg/μm] (yellow arrowhead) in the PS-LR image (a) and high DOP [1.00] in the PS-DOP image (b) corresponds histologically to the scar region with an abundance of fibroblasts and relatively thin, disorganized collagen bundles (d), while the region with higher LR [0.9 deg/μm] (red arrow) and high DOP [0.96] corresponds to thicker, more organized collagen bundles in the dermis and relatively few fibroblasts (e). T=Tattoo mark. Color bars range from 0-1.2 deg/μm for PS-LR and 0.5-1 for PS-DOP images, respectively. Scale bars = 1 mm (a-c), 100 μm (d, e).

ingly, we observed that the remodeling of collagen is correlated with a significant increase in LR in both the incisional and excisional HTS models. This ability to probe HTS *in vivo* allows us to gain significant biological insights into collagen remodeling, which plays a central role in wound healing. While the excisional wound model provides a convenient approach to study deeper scars which are more difficult to treat clinically, the incisional wound model with a tension device provides an elegant way to control the size of the scar systematically (e.g., by varying duration of tension placement) as shown here.

Unlike previous studies employing PS-OCT for the characterization of skin and scar tissue[19,64,66,69,71], we reconstructed the local retardation (instead of cumulative retardation), which reflects tissue birefringence more closely and is much more intuitive to interpret. Local retardation expresses how much the birefringence of the tissue rotates the polarization states at each depth, while cumulative retardation compares the polarization states at a given depth with respect to the surface (resulting in increasing

values even in uniform tissue with constant birefringence). In addition, we computed DOP, which provides a useful metric to identify and measure HTS. Our expression of DOP is similar to the degree of polarization uniformity established by Gotzinger et al[34]; however, here we employ a spectral binning algorithm and spatial averaging to reduce noise[91]. DOP captures the uniformity of the measured polarization states in a small region of interest. In a homogeneous tissue, the polarization states of neighboring pixels are expected to be very similar. In heterogeneous tissues, where two adjacent image pixels potentially interrogate two differently oriented collagen bundles, they are more likely to differ and reduce the measured DOP.

Using LR and DOP, we were able to clearly differentiate normal skin from HTS due to the very different collagen architecture in each case. In normal skin, the heterogeneous, mesh-like organization of highly organized collagen bundles give rise to islands of high dermal birefringence in PS-LR images, alternating with areas of low birefringence due to the varying alignment of the bundles with respect to the optical imaging axis. Furthermore, the spatial dimensions of the region of interest required for the generation of the PS-LR and PS-DOP images frequently include several bundles, accentuating the heterogeneous appearance of normal skin. This heterogeneity also explains the rapid decrease of DOP beyond the epidermis. In contrast, HTS are characterized by finer, and microscopically less organized collagen that exhibits lower dermal birefringence, increasing over time as the fibers remodel and thicken. HTS are optically more homogenous and preserve the polarization state of the incident light, resulting in high DOP values deep within the dermis. In addition, the epidermis and papillary dermis typically showed reduced local retardation values and also preserved the polarization state of the incident light, leading to a high DOP.

In our validation study, the HTS area measured with PS-OFDI showed the expected dependence with the duration of tension and matched well with histological assessment of the same region. DOP provides a measure of the HTS area in the dermis and LR tends to be more variable particularly as the collagen fibers mature. In contrast, DOP typically remains high throughout scar remodeling. One lim-

itation of DOP is that superficial layers normally exhibit high DOP values, which can make it difficult to assess the lateral extent of the scar on the surface.

Our histological analysis confirmed that there is significant hypertrophic scar formation after placing the device for 8 to 10 days. Although the area of scar formation was increased in the 4-day and 6-day groups compared to the control group, histological features of hypertrophic scar were not as evident. This is consistent with an earlier report suggesting that the duration of tension was critical to HTS formation and that at least 7 days of continuous loading was required in a mouse model[1]. It is fascinating that our rat model showed not only significantly increased area of scar in the 10-day group, but also similar histopathological features of HTS in human tissue including increased cellularity of fibroblasts and a dermal nodule with haphazard orientation of collagen bundles.

Finally, this study demonstrated 3D, longitudinal assessment of an HTS model *in vivo* at high-resolution. We observed rapid remodeling of scars in the first week after tension device removal, followed by a more progressive remodeling phase, including the emergence of a region with increased birefringence but high DOP deep within the scar. Interestingly, the increase in local retardation corresponded well with the transition from a highly cellular, immature scar with thin collagen fibers at week 0 to a less cellular, more mature scar with thicker collagen fibers at week 4. Our excisional HTS study at 6 months further suggests that LR can be used as a surrogate for collagen remodeling, while DOP can be used to monitor the size of HTS during the remodeling process.

Currently, there is a lack of high-resolution imaging tools to study wound healing and scar formation systematically and longitudinally *in vivo*. Given that collagen plays a critical role in the pathogenesis of abnormal wound healing, it is an important target for imaging. Increased collagen synthesis by fibroblasts with the expression of TGF-β and PDGF, and decreased collagen degradation with reduced MMP activity, are hallmarks of this process[96]. In fact, a study demonstrated the use of TGF-β1 and 2 neutralizing antibodies in rats to prevent scar formation in dermal wounds[74]. Therefore, our label-free, high-resolution imaging technique can serve as a promising tool to gain significant insights

into wound healing by monitoring both scar size (using DOP) and collagen remodeling (using LR) longitudinally. For example, healing of the scar increases the LR signal and decreases the DOP back to values observed in normal skin.

4.5 Summary

In this chapter, we demonstrated the use of PS-OFDI for the 3D, longitudinal monitoring of collagen remodeling in murine HTS *in vivo*. We further showed that the combination of local retardation and DOP provide a robust optical signature for assessing HTS in both an incisional model for up to 1 month and excisional model with a deeper, more mature scar for up to 6 months. Indeed, most of our current therapeutic approaches for treating HTS rely on targeting or reversing the abnormal collagen deposited during wound healing. For example, intralesional injection of corticosteroids is thought to decrease fibroblast proliferation and collagen synthesis, while pulsed dye laser treatment is thought to favor collagen degradation and fibroblast apoptosis[86,48]. However, the lack of non-invasive scar imaging techniques in well-established animal models for HTS has hindered the study of HTS formation *in vivo*, especially at earlier time points since most studies relied on surgical scar specimens harvested months after their formation. Therefore, the ability to assess collagen *in vivo* in an animal model of HTS, as demonstrated in this chapter, enables further investigation to explore novel, targeted therapeutic approaches for HTS, such as partial electroporation. In addition, the PS-OFDI technique can be directly applied to imaging human HTS *in vivo* as we expect a similar optical signature (decreased local retardation and increased DOP) given the similarity in collagen organization, namely the presence of fine collagen fibers with haphazard orientation in a dermal nodule. Clinically, this non-invasive, high-resolution 3D scar imaging capability can be exploited to improve the management of HTS, including the initial assessment and longitudinal monitoring of treatment response in patients.

5

A generic framework for laser thermal therapy monitoring using complex differential variance

Conventional thermal therapy monitoring techniques based on temperature are often invasive, limited by point sampling, and are indirect measures of tissue injury, while techniques such as magnetic resonance and ultrasound thermometry are limited by their spatial resolution. The visualization of the thermal coagulation zone at high spatial resolution is particularly critical to the precise delivery of thermal energy to epithelial lesions. In this chapter, we present an integrated thulium laser ther-

mal therapy monitoring system based on complex differential variance (CDV), which enables the 2D visualization of the dynamics of the thermal coagulation process at high spatial and temporal resolution with an optical frequency domain imaging system. With proper calibration to correct for noise, the CDV-based technique was shown to accurately delineate the thermal coagulation zone, which is marked by the transition from high CDV upon heating to a significantly reduced CDV once the tissue is coagulated, in 3 different tissue types *ex vivo*: skin, retina, and esophagus. The ability to delineate thermal lesions in multiple tissue types at high resolution opens up the possibility of performing microscopic image-guided procedures in a vast array of epithelial applications ranging from dermatology and ophthalmology to gastroenterology and beyond.

5.1 Introduction

The current state-of-the-art techniques for clinical thermal therapy monitoring typically involve the use of temperature as part of the treatment feedback loop. Unfortunately, temperature measurements using thermocouples only permit point sampling, while emerging magnetic resonance thermometry techniques[73,20] and ^{15}O-water PET imaging[7] are limited by low spatiotemporal resolution and are expensive to use. More recently, photoacoustic thermography of tissue was also investigated for the assessment of myocardial ablation lesions[43]. However, these temperature-based monitoring techniques can only provide an indirect estimate of tissue injury and the spatial resolution remains low for epithelial applications.

In Chapter 2, we presented the feasibility of monitoring thermal therapy in the skin using polarization-sensitive optical frequency domain imaging. However, PS-based approaches are limited to tissue with high birefringence at baseline (e.g., muscle, skin, or tendon) and their broad application to real-time monitoring of thermal therapy in diverse tissue types, such as the esophagus, remains challenging. As an alternative approach, we previously demonstrated the feasibility of visualizing injury depth in

laser thermal therapy of porcine esophagus based on phase variations in OCT; however, this requires careful phase calibration or a highly phase-stable OCT system and was demonstrated in an M-mode imaging configuration, enabling only 1-D, single-point monitoring without structural information [88].

In this work, we developed a 2-D thermal therapy monitoring algorithm (with potential extension to 3-D) using complex differential variance [61], which exploits the phase and intensity fluctuations during thermal therapy but does not require a highly phase-stable OCT system. The algorithm is applied to the OCT data directly, so visualization of structural information simultaneously during therapy monitoring is not inhibited. To assess the feasibility of this approach for monitoring laser thermal therapy, a wavelength tunable thulium fiber laser (1860-1895 nm) was used, which takes advantage of a strong water absorption peak for thermal coagulation in biological tissue. Using the integrated thulium laser and OCT imaging setup, we demonstrate the ability of the CDV-based technique to accurately delineate the thermal coagulation boundary in 3 different tissue types: retina, skin, and esophagus, which opens up the possibility of performing microscopic image-guided interventions at high spatiotemporal resolution in numerous clinical applications.

5.2 Materials and Methods

5.2.1 Laser thermal therapy experimental setup

Figure 5.1 shows the experimental setup used for the laser thermal therapy study. A detailed description of the optical frequency domain imaging system was reported previously [41]. Briefly, the system features a fiber ring wavelength-swept laser operating at 240 kHz with 4-fold interleaving, a center wavelength of 1310 nm and a 125 nm sweep range. An acousto-optic modulator was used in the reference arm to remove depth-degeneracy [100]. An imaging window of 10 mm, consisting of 1024 A-lines/B-scan, was scanned with a focused beam resulting in a $1/e^2$ radius of 32 μm of the lateral point spread function in the squared norm of the complex-valued tomogram.

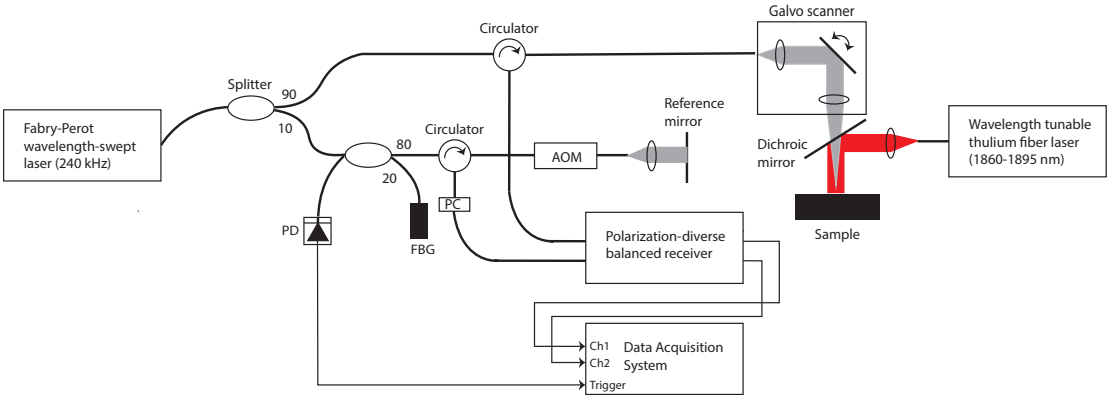

Figure 5.1: Schematics of the laser thermal therapy monitoring setup integrating an optical frequency domain imaging system with a wavelength tunable thulium fiber laser. Simultaneous OCT imaging and laser therapy with a thulium fiber laser is achieved using a dichroic mirror and programmable shutter to synchronize the timing of therapy. AOM, acousto-optic modulator; PC, polarization controller; PD, photodiode; FBG, fiber Bragg grating.

A wavelength tunable thulium fiber laser (IPG Photonics), which provides single-mode output from 1860 nm to 1895 nm, was used for laser thermal therapy. The benchtop setup integrated the thulium laser into the OCT optical path using a dichroic mirror. The collimated beam with a $1/e^2$ diameter of 800 μm, measured with the WinCamD UCD12 beam profiler (DataRay, Redding, CA), was aligned to the center of the imaging plane on the tissue surface and the wavelength was set to 1890 nm to match the water absorption peak. Output power was varied from 300 mW to 500 mW (60 W/cm^2 to 100 W/cm^2) to investigate the technique at various fluence rates, including those reaching tissue vaporization threshold[90].

5.2.2 Processing algorithm

Figure 5.2 provides an overview of the processing algorithm developed for laser thermal therapy monitoring and coagulation zone visualization in this study. We employed complex differential variance (CDV)[61], which exploits both intensity and phase variations, to map the dynamic fluctuations in the complex OCT signal during the thermal coagulation process and extended this implementation to calibrate for noise and to enable the intuitive visualization of the coagulation zone. For a pair of A-lines

acquired at times t and $t+1$ (in M consecutive B-scans), CDV is computed as follows:

$$f_{CDV}(z) = \sqrt{1 - \frac{\sum_{t=0}^{M-1} \left| \sum_{l=-L}^{L} w(l)\, R(z-l,t)\, R^*(z-l,t+1) \right|}{\sum_{t=0}^{M-1} \sum_{l=-L}^{L} w(l)\, \frac{1}{2} \left[|R(z-l,t)|^2 + |R(z-l,t+1)|^2 \right]}}, \tag{5.1}$$

where $R(z,t)$ is the complex OCT signal, $R^*(z,t)$ its complex conjugate, $w(k)$ is a depth window function with length $2L+1$, and M indicates the number of consecutive B-scans used for averaging. Here, a Hanning window with a length of 11 depth pixels ($L=5$) was used and M was set to 10 B-scans (which results in an effective frame rate of 23 fps with 1024 A-lines/B-scan at a 240 kHz A-line rate). While this algorithm intrinsically rejects phase noise induced by small axial bulk tissue motion and synchronization errors, we observed an SNR-dependent increase in CDV in static regions resulting in a non-zero baseline CDV in deeper regions due to decreased SNR. Hence, we performed an SNR-dependent calibration of the CDV using a static region within the tissue next to the therapy zone (calibration window size: 20 x 10 pixels after downsampling by 10x in both the intensity image and raw CDV image, each with an original size of 1024 x 1024 pixels). The SNR-dependent CDV was fitted to an exponential decay and subtracted from the raw CDV to derive the calibrated CDV values (CDV_{cal}). The calibrated CDV was mapped onto the intensity OCT images for simultaneous visualization of underlying structures. Finally, the coagulation zone was visualized by highlighting regions that have reached a cumulative CDV threshold ξ and returned to a low CDV below ε upon coagulation, where the cumulative CDV as a function of time t is defined as

$$cCDV_{cal}(t) = \sum_{\tau=0}^{t} CDV_{cal}(\tau), \tag{5.2}$$

and the coagulation zone $c(t)$, which is a binary mask that evolves as a function of time t, is determined as follows:

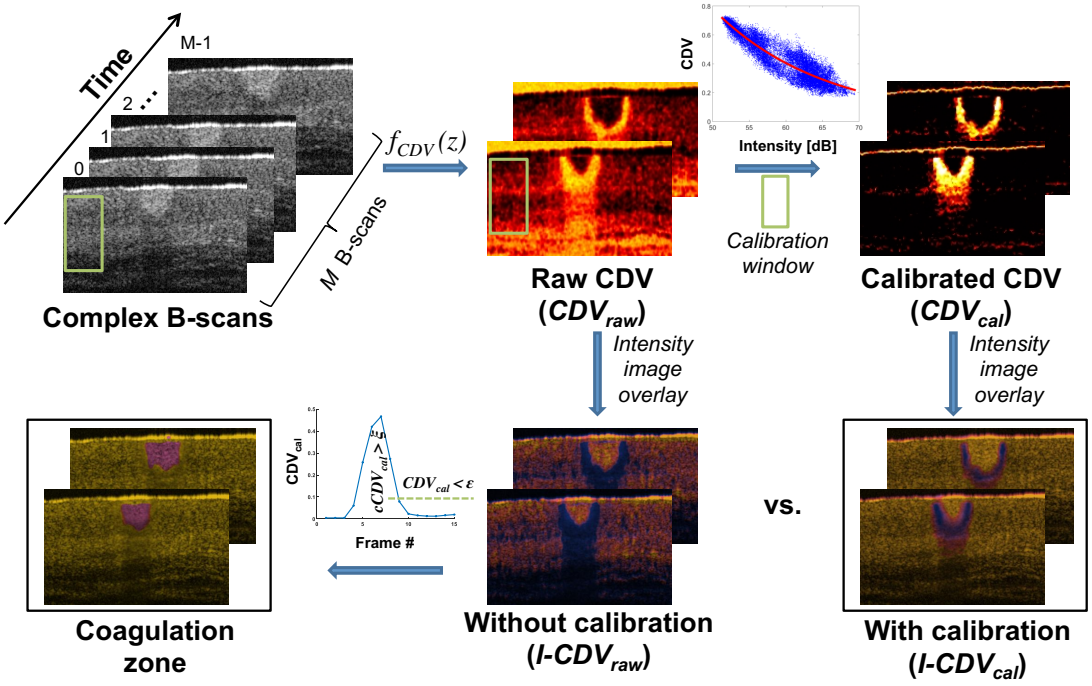

Figure 5.2: Overview of processing algorithm for laser thermal therapy monitoring and coagulation zone visualization. Complex B-scans are processed in batches of M B-scans to produce raw CDV (CDV_{raw}) frames. Using a calibration window in a static region within the tissue, a calibration curve for the SNR dependence is estimated and applied to produce the calibrated CDV frames (CDV_{cal}). The final image is produced by overlaying the intensity image on top ($I - CDV_{raw}$ vs. $I - CDV_{cal}$), showing significant improvements with calibration. The coagulation zone is visualized by detecting regions that have reached the cumulative CDV threshold (ξ) and returned to a low instantaneous CDV upon coagulation (ε).

$$c(t) = \{cCDV_{cal}(t) > \xi\} \cap \{CDV_{cal}(t) < \varepsilon\} \tag{5.3}$$

5.2.3 Histological Analysis

Tissue samples (bovine eye, porcine skin, and porcine esophagus) were harvested immediately after sacrifice and laser thermal therapy was performed *ex vivo* at room temperature. Tissue marking dyes were placed on each side of the laser therapy spot for co-registration of OCT images with histology. Tissue

samples were trimmed and sectioned for either routine H&E histology or nitroblue tetrazolium chloride (NBTC) histology (with eosin counterstain) after embedding in optimum cutting temperature compound for frozen sections at 10 μm. NBTC stains for the activity of NADH-diaphorase, which subsides upon thermal coagulation and cell death[62].

5.3 Results

Figure 5.3 shows an example of monitoring laser therapy in bovine retina *ex vivo* using the CDV-based approach, demonstrating the ability to clearly visualize the dynamics of the laser-induced heating and coagulation process. The center therapy zone exhibits a rapid rise in CDV (purple) extending from the retina into the sclera upon the initiation of laser therapy at 300 mW (60 W/cm^2). A growing zone with reduced CDV (yellow), surrounded by a rim of high CDV (purple/red), was observed as the process continued. This growing zone (marked by the blue dotted lines on each image) corresponds well histologically to the thermal coagulation zone marked by the denaturation of the collagen in the fibrous sclera layer in H&E. Figure 5.4 shows the impact of averaging on the visualization of the coagulation process. While 10 consecutive B-scans (M=10) were used for all subsequent processing given the high A-line rate of the Fabry-Perot based system used (240 kHz), a lower number (M=2 to 5) can be chosen for conventional, swept source OCT systems currently used in several clinical systems to provide a similar assessment of the coagulation process.

Figure 5.5 shows a similar thermal coagulation signature in the rapidly expanding zone with reduced CDV surrounded by high CDV for the case of porcine skin *ex vivo* at the same power setting of 300 mW (60 W/cm^2). The panel clearly reveals the early dynamics of the coagulation process for the first 1.5 s. Lesion formation appeared slightly faster in this case compared to the retina, most likely due to differences in tissue properties and the presence of a small layer of aqueous humor on top of the retina which absorbed part of the thermal energy delivered. NBTC histology was performed to confirm

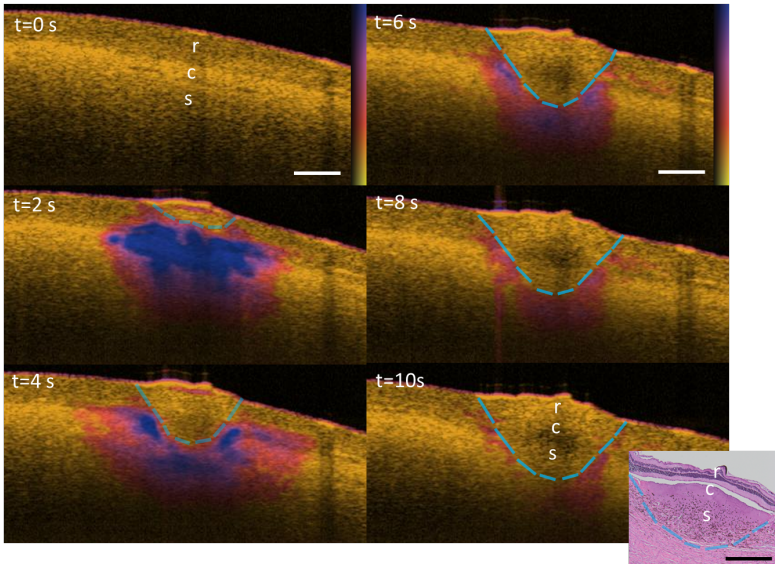

Figure 5.3: Laser thermal therapy monitoring in bovine retina *ex vivo* using calibrated complex differential variance (CDV_{cal}). Images represent cross-sectional slices at the center of the thulium laser therapy beam (300 mW or 60 W/cm^2) every 2 s for 10 s, where CDV_{cal} was overlaid on intensity images. H&E histology (inset) reveals a coagulation zone extending into the sclera that corresponds with the region with reduced CDV (yellow) at the center delineated by an expanding boundary with high CDV (purple). Colorbar (CDV_{cal}) ranges from 0 to 0.5. Blue dotted lines, coagulation zone. r, retina; c, choroid; s, sclera. Scale bars = 500 μm.

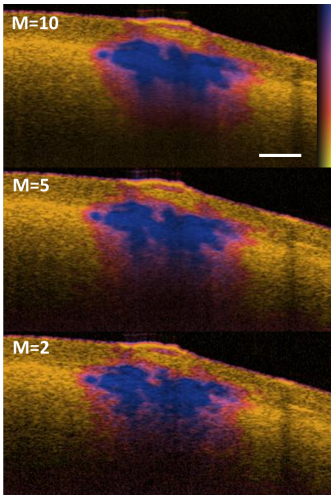

Figure 5.4: Impact of varying the averaging parameter ($\mathcal{M}$=10, 5, and 2 consecutive B-scans) on the overall ability to visualize the dynamics of the coagulation process (using the same dataset as Fig. 5.3 at t=2 s). Colorbar (CDV_{cal}) ranges from 0 to 0.5. r, retina; c, choroid; s, sclera. Scale bar = 500 μm.

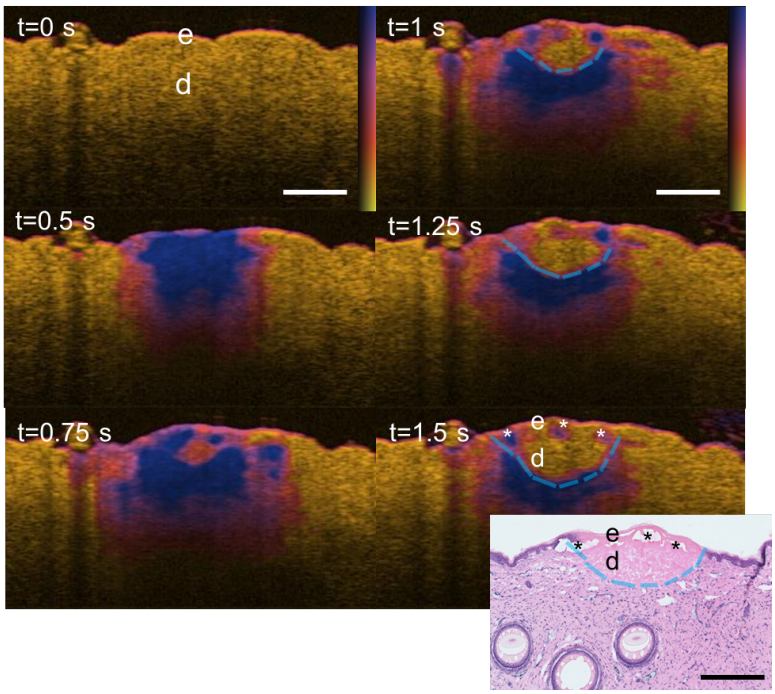

Figure 5.5: Laser therapy monitoring in porcine skin *ex vivo* at 300 mW (60 W/cm^2) for 1.5 s. NBTC histology with eosin counterstaining (inset) at treatment endpoint confirms that the extent and shape of thermal damage in the dermis (NBTC-negative region in pink) corresponds well with the expanding zone with reduced CDV (yellow) delineated by a boundary with high CDV (purple). Colorbar (CDV_{cal}) ranges from 0 to 0.5. Blue dotted lines, coagulation zone. e, epidermis; d, dermis. Asterisks (*), air bubbles. Scale bars = 500 μm.

the boundary of thermal coagulation, and the NBTC-negative region, indicative of thermal damage, corresponds well with the coagulation zone indicated by the CDV-based technique.

To further investigate this approach for delineating lesion boundaries in different tissue types and at different laser power settings, we performed another experiment in porcine esophagus *ex vivo* using laser power from 300 mW to 500 mW, corresponding to fluence rates of 60 W/cm² to 100 W/cm² (Figure 5). The lesion boundary was particularly well defined at the early phase (t=1-3 s), but became less clear as the thermal coagulation zone expanded, especially at the lowest fluence rate (60 W/cm²). Interestingly, at the highest fluence rate tested (100 W/cm²), a superficial layer with increased CDV was observed inside the therapy zone due to the formation of expanding air bubbles that eventually

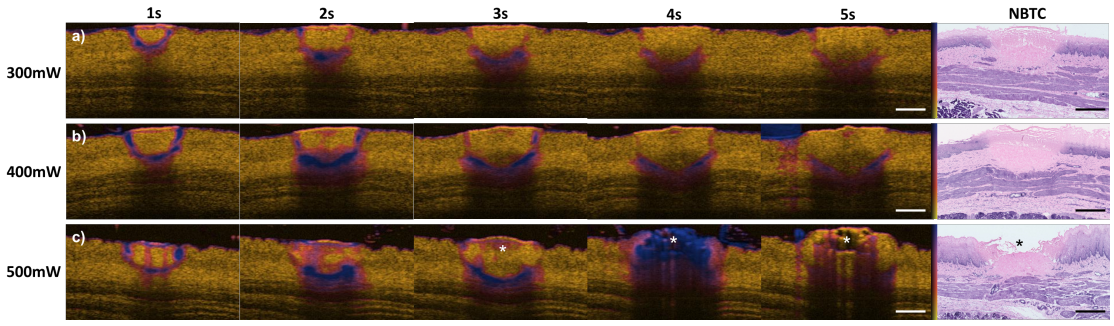

Figure 5.6: Effect of increasing output power of the thulium fiber laser in porcine esophagus *ex vivo*: (a) 300 mW [60 W/cm^2], (b) 400 mW [80 W/cm^2], and (c) 500 mW [100 W/cm^2]. NBTC histology with counterstaining was performed at the treatment endpoint (t=5 s), showing close correspondence between the NBTC-negative region (pink) and the zone with reduced CDV (yellow) delineated by a boundary with high CDV (purple). Colorbar (CDV_{cal}) ranges from 0 to 0.5. Asterisks (*), air bubbles. Scale bars = 500 μm.

burst with tissue vaporization (at t=4 s when the instantaneous CDV reached the maximum value) as confirmed by histology.

To better visualize the evolution of the coagulation zone over time, the history of CDV values was used to detect regions that have reached the coagulation threshold (Eq. 3), highlighted in purple and overlaid onto the intensity images (Figure 5.7). This visualization technique overcomes the limitation of displaying the instantaneous CDV, when the boundary becomes less visible with the expansion of the coagulation zone, especially at the lower power settings. Even at the highest power setting tested (when the tissue vaporization threshold was reached), this approach still provided a good estimate of the coagulation zone, as confirmed by NBTC histology.

Finally, histological validation with NBTC staining was performed at representative time points during laser therapy from 1s to 5s at 400 mW (80 W/cm²), showing that the coagulation zone delineated by the CDV approach corresponds well histologically to the NBTC-negative region and thermal damage (Figure 5.8). In particular, at the early phase of therapy (t=1 s), the CDV-based technique indicates an injury depth limited to the epithelium (reaching the lamina propria at t=3 s) while at the treatment endpoint (t=5 s), the injury depth has reached the muscularis mucosa, as confirmed histo-

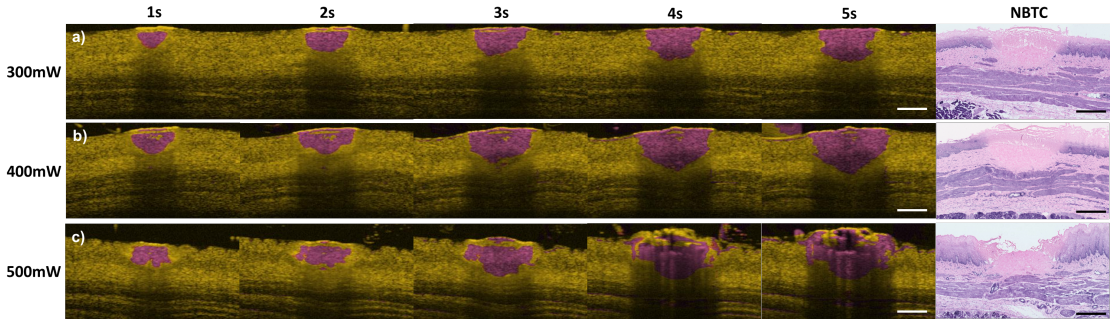

Figure 5.7: Visualization of the coagulation zone in porcine esophagus using the history of CDV values at different power settings: (a) 300 mW [60 W/cm^2], (b) 400 mW [80 W/cm^2], and (c) 500 mW [100 W/cm^2]. Purple color indicates regions that have reached the coagulation threshold defined by the cumulative CDV parameter and low instantaneous CDV (ξ =2 and ε=0.1), which provides an alternative way to more clearly delineate the thermal coagulation zone as confirmed by NBTC histology. Scale bars = 500 μm.

logically by NBTC staining. By contrast, the lesion boundary is difficult to delineate with the intensity OCT images alone despite the increased backscattering observed in the coagulated tissue, especially as the shadow below the coagulated zone expanded at later time points (Fig. 5.8c).

To further validate the findings systematically and quantitatively, three lesions were created for each therapy duration, and the depth of the coagulation zone (injury depth) was measured on corresponding CDV images and NBTC histology independently by three experts, showing good agreement between the CDV-based and NBTC-based measurements overall ($r^2 = 0.95$) (Figure 5.9). In cases where discrepancies were observed, the depth measured on NBTC histology was typically smaller than that measured using the CDV image (50-100 μm), most likely due to variability in tissue shrinkage during frozen section processing as well as instantaneous thermal expansion and bubble formation in the superficial layer during therapy.

5.4 Discussion

In this study, we demonstrated the use of dynamic OCT measurements based on complex differential variance to accurately delineate the coagulation zone in laser thermal therapy and validated this

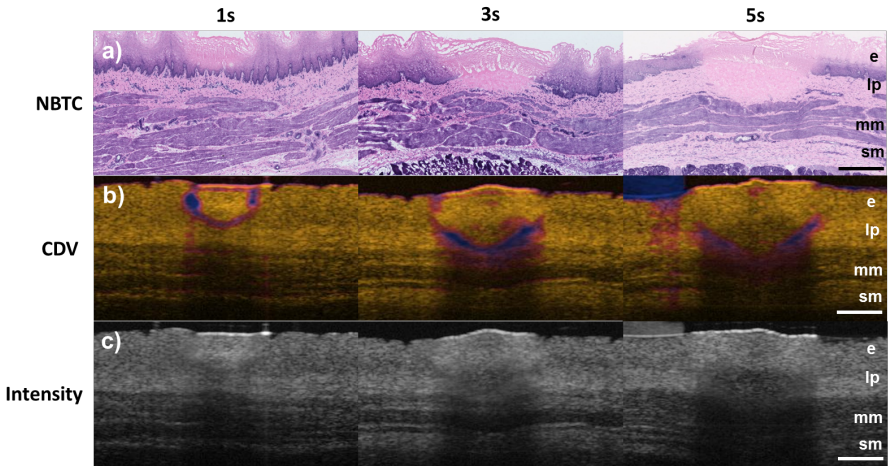

Figure 5.8: Histological validation of CDV-based coagulation zone monitoring in porcine esophagus *ex vivo* at 400 mW (80 W/cm^2) for 5 s. NBTC histology with counterstaining was obtained at each representative time point (1 s, 3 s, and 5 s), showing close correspondence between the NBTC-negative coagulation zone (pink) (a) and the region showing the transition from high to low CDV (purple to yellow) (b), which is difficult to delineate clearly using intensity images alone (c). e, epithelium; lp, lamina propria; mm, muscularis mucosa; sm, submucosa. Scale bars = 500 μm.

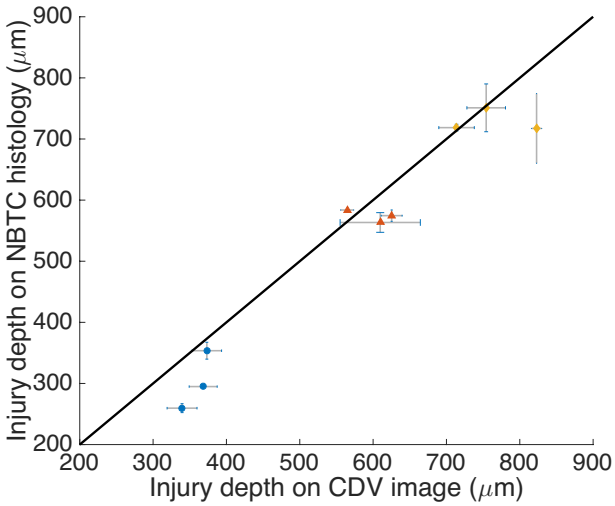

Figure 5.9: Quantitative validation of coagulation zone depth (injury depth) in porcine esophagus after laser therapy at 400 mW (80 W/cm^2) for 1 s, 3 s, and 5 s. Each data point represents the mean +/- SD of the injury depths on the OCT (CDV) image and corresponding NBTC histology measured independently by three experts. The solid line represents perfect correlation of OCT and histology measurements for comparison. Blue circles, 400 mW (80 W/cm^2) at 1 s. Red triangles, 400 mW (80 W/cm^2) at 3 s. Yellow diamonds, 400 mW (80 W/cm^2) at 5 s.

approach histologically in 3 different tissue types: skin, retina, and esophagus. By overlaying this information directly on intensity OCT images, the active treatment zone was visualized simultaneously with the underlying tissue architecture, which enables lesions to be targeted more precisely. Compared to previous work based on PS-OCT or polarimetry-based techniques[19,72,29,26], the current method is not limited to biological tissues with high birefringence at baseline (e.g, skin, muscle, and tendon) and has broader implications in a number of clinical applications.

However, there are several limitations to the current CDV-based approach. First, unlike PS-OCT where the thermal lesion can be readily imaged and visualized post treatment due to the loss of tissue birefringence, the CDV-based approach derives contrast from the real-time variations in phase and intensity signals that subside once the therapy beam is turned off. The need for real-time tracking also means that motion can lead to an artificial increase in CDV, although this can be mitigated with increased imaging speed or similarly by decreasing the number of B-scans (M) used to compute CDV in Eq. (1), as well as by various motion correction techniques[77,99,4]. Similarly, perfusion in living tissue can contribute to the CDV signal, but considering the time scale, the relative contribution will likely be smaller than the therapy-induced CDV signal. In addition, the active treatment zone boundary can become more difficult to delineate as the coagulation zone grows bigger and the CDV signal degrades as a function of depth. When the uncalibrated CDV values begin to saturate at depths approaching the noise floor (typically at a depth > 1-1.5 *mm*), the dynamics of the heating process becomes increasingly difficult to observe, especially at lower fluence rates. Therefore, we have performed an SNR-dependent calibration to enable more robust visualization at greater depths, which provides an accurate estimate of the lesion boundary at the different depths tested. However, the depth limitation is also a fundamental limitation of OCT imaging, which is difficult to overcome even with calibration for noise, due to inherent limits on system sensitivity and penetration depth of light. To further improve the visualization of the coagulation zone, we developed an alternative visualization method in which the history of CDV values is tracked and regions that have reached a cumulative CDV thresh-

old ξ and returned to an instantaneous CDV below ε (Eq. 3) are highlighted. While the coagulation threshold is likely different between tissue types, this visualization strategy provides a good estimate of the growing coagulation zone that would be more difficult to appreciate with the instantaneous CDV alone.

Compared to our earlier work on monitoring laser therapy with phase variations in M-mode imaging[88], the current CDV-based approach was developed to overcome small axial bulk motion and phase jitter from data acquisition synchronization through the use of a depth window (Eq. 1), which eliminates the need for a highly phase-stable OCT system or precise phase calibration[90]. We further demonstrated 2-D, cross-sectional therapy monitoring in different tissue types (with potential extension to 3-D) to enable simultaneous visualization of underlying tissue structures. It is interesting to observe in both our earlier study and the current study that the active treatment zone is marked by increased phase variation or CDV and the growing coagulation zone corresponds very well to the region where the phase variation or CDV has subsided.

5.5 Summary

In this chapter, we developed a generic framework for thermal therapy monitoring using complex differential variance, which maps the dynamic fluctations in the signal intensity and phase and can be applied to different tissue types such as retina, skin, and esophagus. By providing a framework for real-time therapy monitoring using the CDV-based technique, more targeted and personalized thermal therapy delivery can be achieved in dermatology, ophthalmology, gastroenterology, and beyond. An interesting opportunity provided by this promising therapy monitoring approach is the ability to precisely control various laser parameters, such as power, wavelength, and duration of therapy, to better tailor the therapy to the target lesion with immediate feedback[100]. For example, the current technology can be applied to tailor the laser treatment of hypertrophic scars[5], laser photocoagulation

in diabetic retinopathy especially in the sub-threshold regime[70], and more targeted thermal therapy of epithelial lesions such as Barrett's esophagus with high-grade dysplasia[88,100,4]. Using the current approach, more precise thermal therapy in epithelial lesions may be achieved by tailoring the thermal injury to the desired depth; for example, in the treatment of Barrett's esophagus, it is important to avoid excessive damage beyond the submucosa to reduce the risk of stricture formation[75]. The ability to delineate thermal lesions in different tissue types, at high spatiotemporal resolution, opens up the possibility of performing microscopic image-guided procedures in a vast array of epithelial applications in the future.

6

Balloon catheter-based radiofrequency ablation monitoring for clinical applications

This chapter discusses the development of an integrated balloon catheter, radiofrequency ablation monitoring system that enables simultaneous imaging and therapy monitoring based on the technique developed in Chapter 5. First, to develop a custom flexible radiofrequency ablation electrode array that can be integrated with the clinical balloon catheter, a finite element model was constructed to determine the optimal geometry of these electrodes. Based on these simulation results, a prototype integrated OFDI-RFA catheter was constructed and tested in porcine esophagus and duodenum *ex vivo*. The latter was used as a model of Barrett's esophagus which is characterized by intestinal metaplasia.

Therapy monitoring through a clinical balloon catheter gives rise to a set of new challenges, most notably the significant artifacts caused by the non-uniformity in circumferential scanning known as non-uniform rotation distortion (NURD) artifacts. To mitigate the NURD artifacts, image features in consecutive frames were analyzed using an accelerated version of the scale-invariant feature transform (SIFT) descriptors[51] to estimate the non-uniform motion and perform the necessary realignment between consecutive frames. The SIFT descriptor is commonly used in image stitching/panorama applications[12] to recognize features across images of the same scene at different angles so that the overlapping regions can be realigned and combined. Once the frames were correctly aligned through NURD correction, the CDV algorithm was applied and with proper calibration for SNR (as discussed previously in Chapter 5), the coagulation process was clearly visualized as validated histologically with NBTC staining.

6.1 Modeling of radiofrequency ablation

To facilitate the development of a custom RF bipolar electrode array that is compatible with the clinical OFDI balloon catheter, a finite element model was constructed using the Comsol Multiphysics modeling software (Burlington, MA) to explore the design space and constraints systematically, including the spacing of electrodes, width of each electrode, and duration of therapy with corresponding voltage requirements for simultaneous imaging and therapy delivery.

6.1.1 Finite element model

Figure 6.1 illustrates the finite element model geometry, which consists of a bipolar radiofrequency electrode array on top of a two-layer tissue slab. The bipolar electrode array consists of three sets of copper electrodes. Alternating electrodes (active and dispersive electrodes) are connected to two different rails/connectors – one serving as the ground and another as the RF voltage source. The

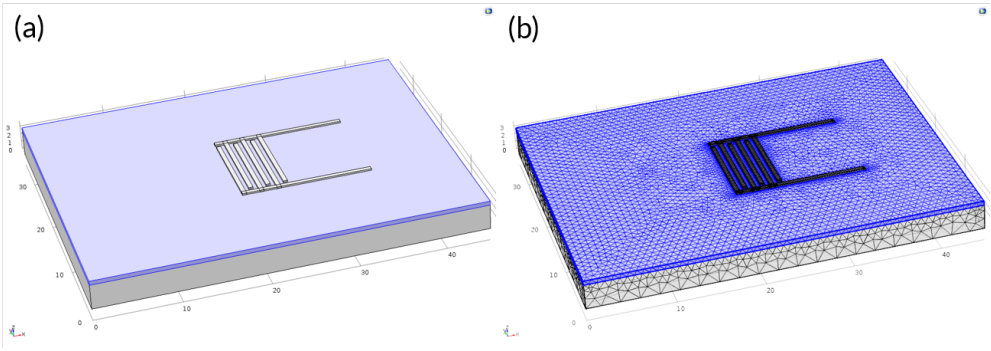

Figure 6.1: Finite element model of a bipolar radiofrequency electrode array consisting of 6 electrodes (500 μm wide and 10 mm long, with a 500 μm spacing) on top of a two-layer tissue slab (a), with corresponding finite element mesh showing a progressively finer tetrahedral mesh around the electrode area (b).

tissue slab is a simplified model of the esophagus consisting of the top epithelial layer (epithelium up to lamina propria) with a thickness of 500 μm and the remaining muscular layer (muscularis mucosa up to muscularis propria) with a thickness of 2.5 mm.

Using the Comsol Multiphysics software, the temperature field and resulting tissue damage over the course of the RF ablation procedure were simulated by solving the following set of equations in the FEM model.

First, the Pennes bioheat equation [65], which governs heat transfer in biological tissue, was solved to derive the temperature field:

$$\rho C\frac{\partial T}{\partial t} - \nabla(k\nabla T) = \rho_b C_b \omega_b (T_b - T) + Q_m + Q_e \quad , \tag{6.1}$$

where ρ is the density of the tissue (kg/m^3), C is the specific heat (J/kg·K), k is the thermal conductivity (W/m · K), T is the temperature of the tissue (K), T_b is the temperature of blood (K), ρ_b is the density of blood (kg/m^3), C_b is the specific heat of blood (J/kg·K), ω_b is the perfusion rate (1/s), Q_m is the metabolic heat source term (W/m^3), and Q_e is the heat from the external source (W/m^3). In the current model, the perfusion term and metabolic heat source term were assumed to be negligible. The density

ρ and specific heat C of the tissue were set at 1070 kg/m^3 and 3700 J/kg·K, respectively. The thermal conductivities of the mucosal layer of the esophagus and the muscular layer were set as 0.343 and 0.49 W/m · K, respectively[35]. The boundary conditions were set to an ambient temperature of 25 °C for all outer boundaries such as the tissue surface and $\vec{n} \cdot (k_1 \nabla T_1 - k_2 \nabla T_2) = 0$ for all interior boundaries.

To couple the bioheat equation to the RF ablation process, the heat from the external source Q_e was set to $\vec{J} \cdot \vec{E}$ where $\vec{J}$ is the current density (A/m^2) and $\vec{E}$ is the electric field intensity (V/m) or $Q_e = \sigma |\vec{E}|^2$ where $\vec{E} = -\nabla V$. The voltage distribution can be solved using Laplace's equation:

$$\nabla \cdot \sigma \nabla V = 0 \quad , \tag{6.2}$$

where V is the voltage and σ is the electrical conductivity (S/m) of the tissue. The electrical conductivities of the mucosal layer and the muscular layer of the esophagus were set as 0.1778 and 0.4459 S/m, respectively[6], and a downward ramp function was implemented between 95 to 100°C to account for the significant drop in electrical conductivity approaching zero once the tissue becomes dessicated as it approaches vaporization threshold at 100 °C[82]. Here, a quasi-static approach (the tissue is considered source-free and displacement currents are neglected) was employed since the biological tissue is purely resistive at the frequency typically used for RF ablation ($\sim$ 500 kHz) and the voltage was set as the root mean squared voltage of the applied RF voltage (V_{rms})[10]. The boundary conditions were set as follows: V=V_{rms} on active electrodes, V=0 on dispersive electrodes and outer domain boundary, and $\vec{n} \cdot (\vec{J}_1 - \vec{J}_2) = 0$ across all other boundaries.

The damage integral $\Omega(r, t)$, which defines the degree of tissue injury (dimensionless) based on the Arrhenius equation[40], is computed as follows:

$$\Omega(r, t) = ln\Big[\frac{C(r, 0)}{C(r, t)}\Big] = \int_0^t A e^{-\frac{E_a}{RT(r,\tau)}} d\tau \quad , \tag{6.3}$$

where $C(r, 0)$ refers to the initial concentration of tissue molecules in the native state, $C(r, t)$ is the

remaining concentration at time t after conversion to the damaged state, A is the frequency factor (s^{-1}), E_a is the activation energy (J/mol) and R is the universal gas constant (8.314 J/mol · K). Here, A was set to 2.88 x 10^{98} s^{-1} and E_a was set to 6.3 x 10^5 J/mol[40]. Note that $\Omega(r, t)$=1 is defined such that it corresponds to 63% tissue injury (necrotic tissue), which is when tissue coagulation first occurs.

Hence, the necrotic tissue fraction θ_d can be expressed as follows:

$$\theta_d = 1 - e^{-\Omega(r,t)} \quad . \tag{6.4}$$

6.1.2 Results and Discussion

Figure 6.2 shows the temporal evolution of the simulated temperature distribution on the tissue surface at an applied voltage of 20 V_{rms} using the 6-electrode bipolar RF array configuration (each with a width of 500 μm and evenly spaced at 500 μm) as illustrated in Fig. 6.1. The rise in temperature was most prominent during the initial phase of heating from ~0-6s, after which it began to plateau. Figure 6.3 shows the experimental surface temperature measurements of the same electrode design fabricated as a flexible circuit and applied on a piece of porcine esophagus *ex vivo*, demonstrating good agreement with the simulation results overall. Surface temperature was measured using the FLIR One infrared camera (FLIR Systems, Wilsonville, OR), calibrated using an emittivity of 0.95.

To validate these measurements further, the same experiment was repeated three times on porcine esophagus *ex vivo* and the average temperature was measured across the ablation region every 2 seconds. Figure 6.4 shows that the experimental results demonstrate generally good agreement with the simulated temperature in the first 2 to 4 seconds, and deviate more as the temperature reaches the coagulation threshold (50-60 °C). This is likely due to the change in tissue properties upon coagulation such as the increase in tissue impedance (namely a significant decrease in tissue electrical conductivity) upon coagulation of biological tissue[10].

Using the simulated temperature profile as a function of time, we can begin to evaluate the voltage

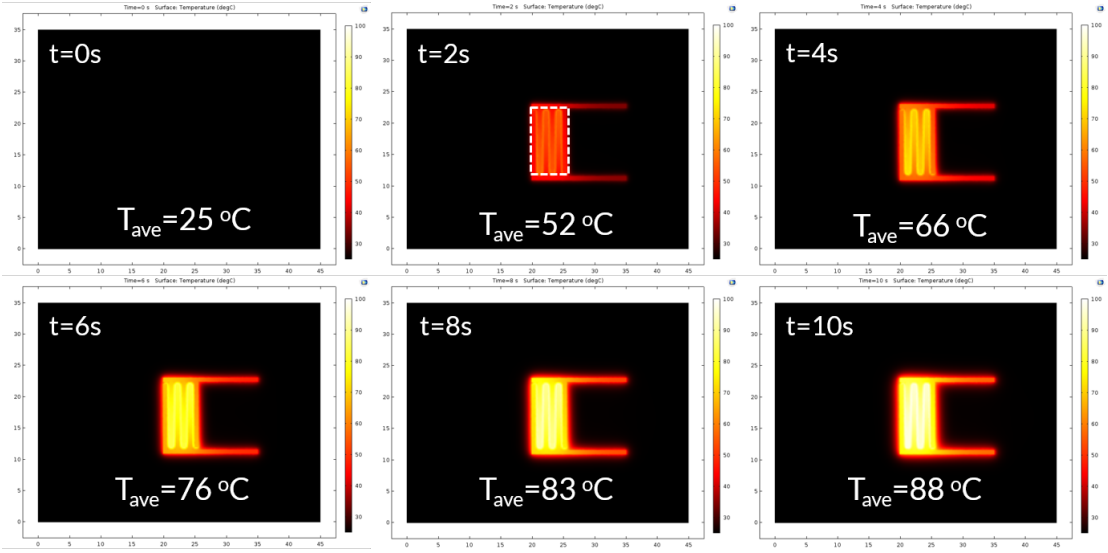

Figure 6.2: Simulated surface temperature distribution during RF heating with the 6-electrode bipolar RF array (20 V_{rms} applied for 10 s). The average temperature was computed across the region defined by the dotted rectangle. Colorbar ranges from 25 °C to 100 °C.

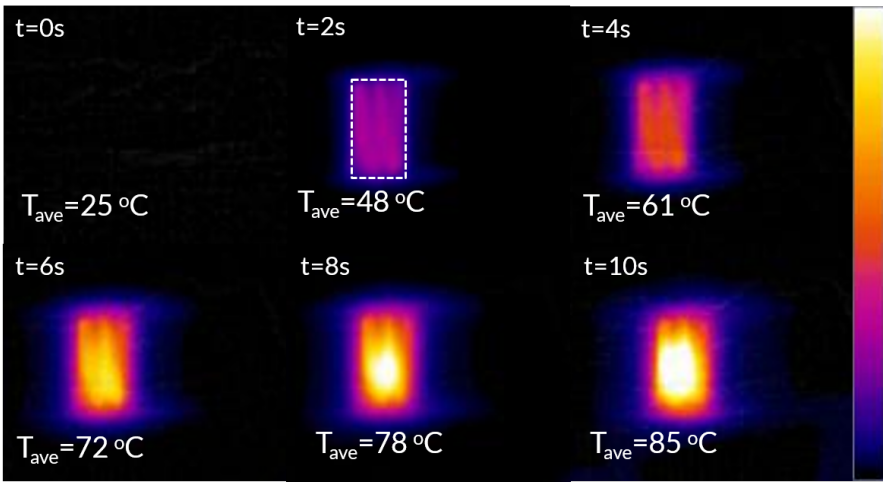

Figure 6.3: Measured surface temperature distribution during bipolar RF heating of porcine esophagus with the 6-electrode bipolar RF array *ex vivo* (20 V_{rms} applied for 10 s). The average temperature was measured across the region defined by the dotted rectangle. Colorbar ranges from 25 °C to 100 °C.

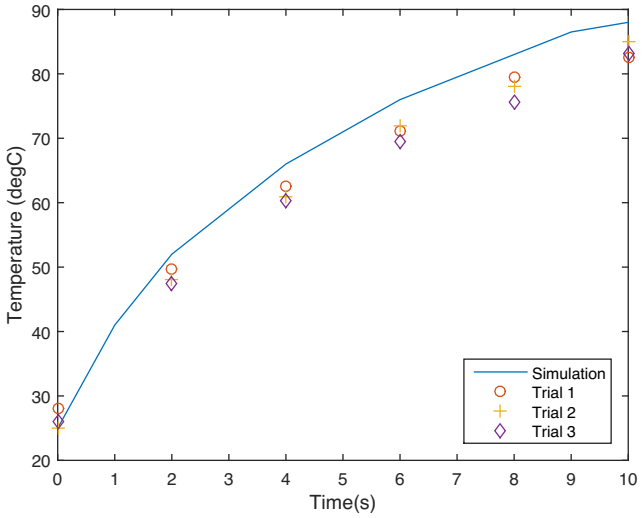

Figure 6.4: Experimental validation of the simulated average surface temperature across the bipolar electrode array (20 V_{rms}, 10 s). Average temperature values were computed across the region covered by the electrodes as illustrated in Fig. 6.3.

requirements for a specific electrode configuration. Figure 6.5 shows the effect of increasing the applied voltage on the time required to achieve the coagulation temperature. For example, it would take only $\sim$ 4 seconds to reach the same endpoint temperature at 25 V_{rms}, compared to 20 V_{rms}, but it would take significantly longer to achieve this temperature at 15 V_{rms}.

In addition to simulating the surface temperature, the cross-sectional temperature profile (cutting through the center of the electrode array) was also simulated using Comsol (Fig. 6.6a), which shows the propagation of the heat through the mucosal layer from 0 to 6 s and deeper into the muscle layer from 6 to 10 s. The corresponding necrotic tissue fraction analysis (based on Equations 6.3 and 6.4) shows a similar trend (Fig. 6.6b) and further suggests that the growth of the thermal lesion is minimal during the initial phase of heating and an RF ablation duration of at least 4-6 seconds is required to achieve a target depth beyond the mucosal layer at the current applied voltage (20 V_{rms}).

Figure 6.7 shows the cross-sectional temperature profile and necrotic tissue fraction between the electrodes at the center of the array as a function of time. Together with Fig. 6.6, these two sets

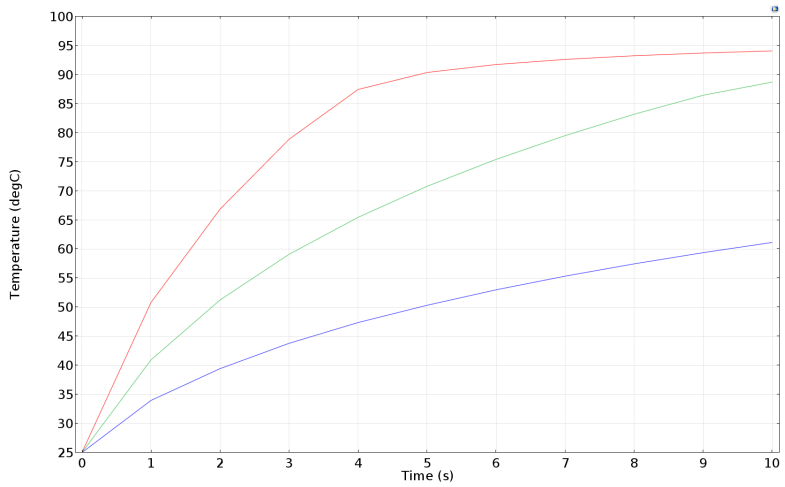

Figure 6.5: Simulated average surface temperature as a function of applied voltage (15, 20, 25 V_{rms} - bottom to top curves). The bipolar radiofrequency electrode array consists of 6 electrodes (500 μm wide and 10 mm long, with a 500 μm spacing).

of figures provide an idea of the three-dimensional temperature field across the lesion and the corresponding thermal lesion growth profile.

In the literature, the 50 or 60 °C isotherm is often used as a surrogate for the boundary of necrotic tissue given tissue coagulation occurs rapidly beyond these temperatures[21] . Figure 6.8 shows that, indeed, the 60 ° C isotherm corresponds well with the necrotic tissue fraction simulated at the end of the therapy (t=10 s). While the 50 °C isotherm is frequently used in RF ablation of liver tumors, it would overestimate the necrotic tissue fraction. This is likely due to the much longer ablation time (on the order of minutes) for the RF ablation of liver tumors.

The effect of varying the applied voltage was investigated further. Figure 6.9 shows the evolution of the temperature rise and corresponding necrotic tissue fraction for an applied voltage of 15 V_{rms}, demonstrating a much slower lesion growth rate. To achieve a similar thermal lesion as that seen with an applied voltage of 20 V_{rms} at 10 s, a therapy duration of $\sim$ 25 s is required. Figure 6.10 further illustrates the temperature profile and necrotic tissue fraction for a higher applied voltage of 25 V_{rms}. In this case, a similar thermal lesion can be achieved with a therapy duration of $\sim$ 6s.

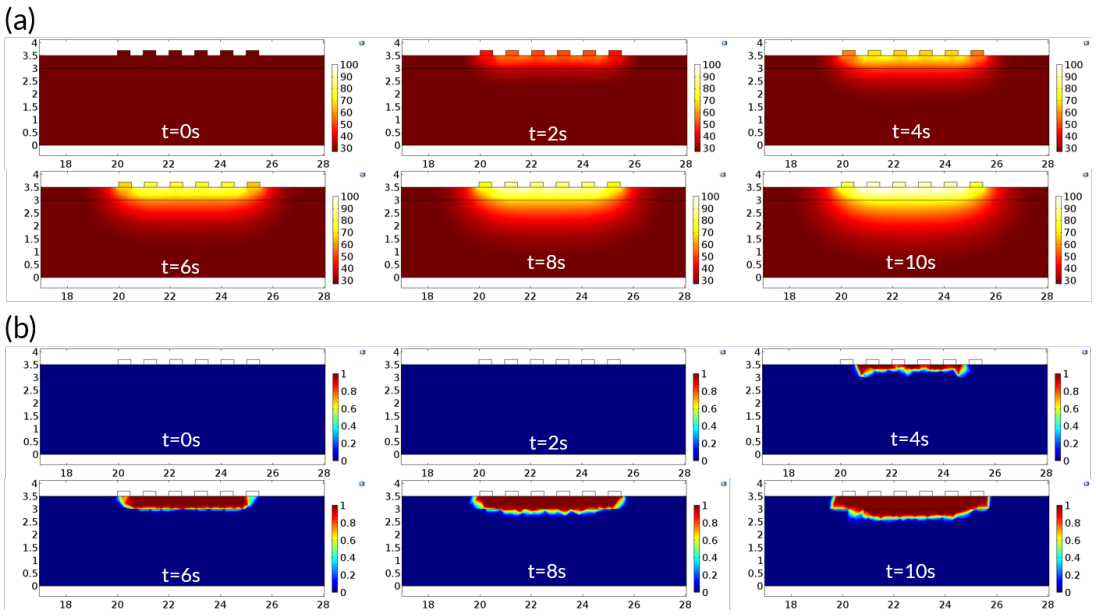

Figure 6.6: Simulated cross-sectional temperature profile and necrotic tissue fraction resulting from RF ablation with the 6-electrode bipolar RF array (20 V_{rms} applied for 10 s). Colorbar in (a) ranges from 25 °C to 100 °C; colorbar in (b) ranges from 0 to 1 (100% tissue damage).

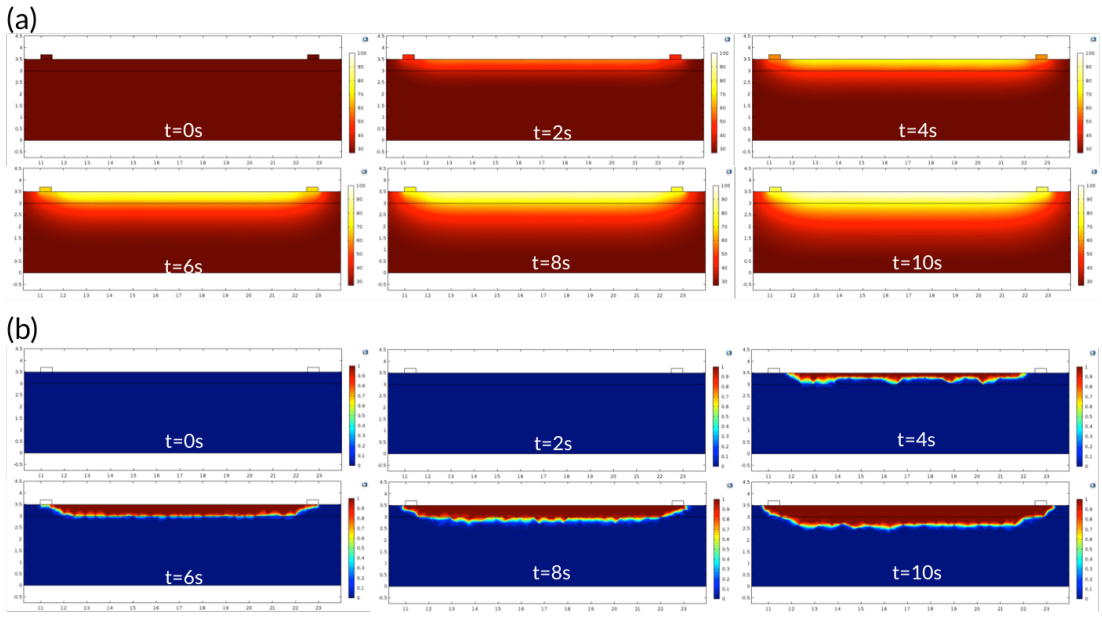

Figure 6.7: Simulated cross-sectional temperature profile and necrotic tissue fraction (between consecutive electrodes at the center of the array) resulting from RF ablation with the 6-electrode bipolar RF array (20 V_{rms} applied for 10 s). Colorbar in (a) ranges from 25 °C to 100 °C; colorbar in (b) ranges from 0 to 1 (100% tissue damage).

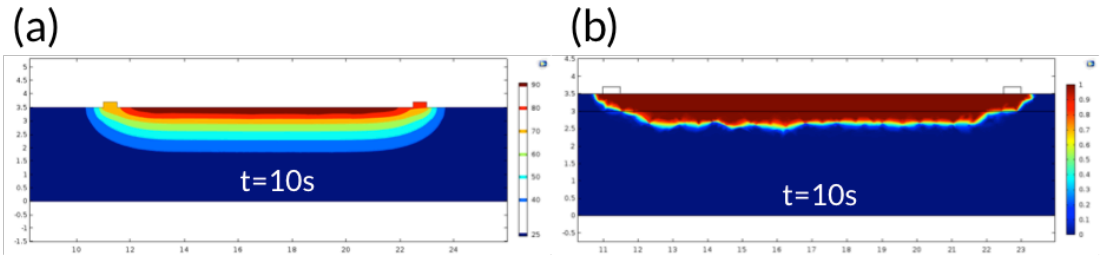

Figure 6.8: Simulated cross-sectional isotherms (40, 50, 60, 70, 80, 90 °C) and necrotic tissue fraction (between consecutive electrodes at the center of the array) resulting from RF ablation with the 6-electrode bipolar RF array (20 V_{rms} at t=10 s). The 60 °C isotherm (green) corresponds well with the necrotic tissue fraction simulated. Colorbar in (a) shows the discrete isotherm levels (40, 50, 60, 70, 80, 90 °C) ; colorbar in (b) ranges from 0 to 1 (100% tissue damage).

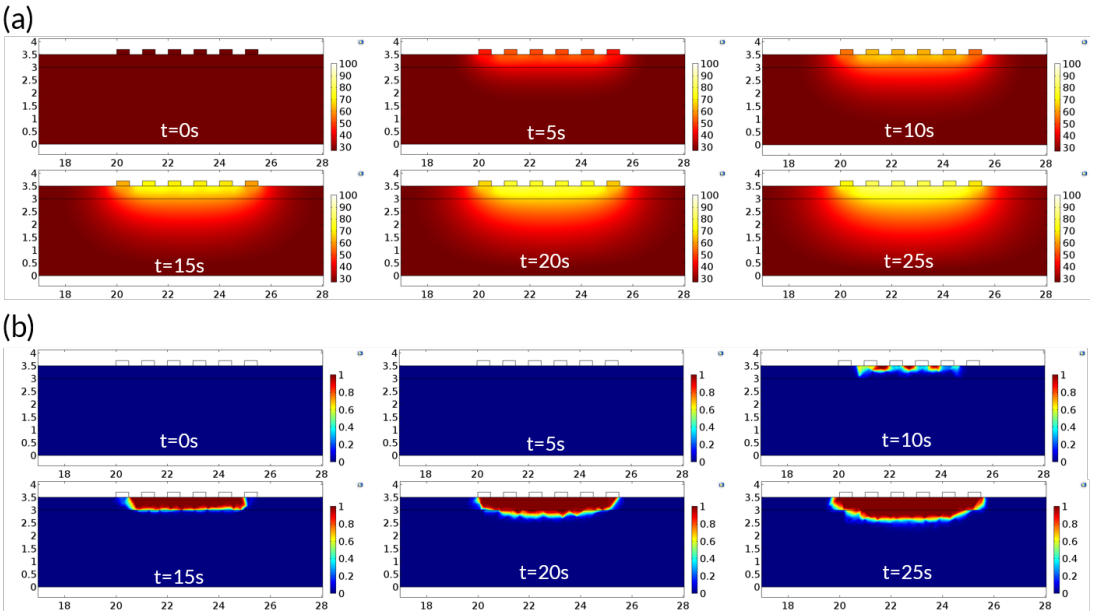

Figure 6.9: Simulated cross-sectional temperature profile (a) and necrotic tissue fraction (b) resulting from RF ablation with the 6-electrode bipolar RF array (15 V_{rms} applied for 25 s). Colorbar in (a) ranges from 25 °C to 100 °C; colorbar in (b) ranges from 0 to 1 (100% tissue damage).

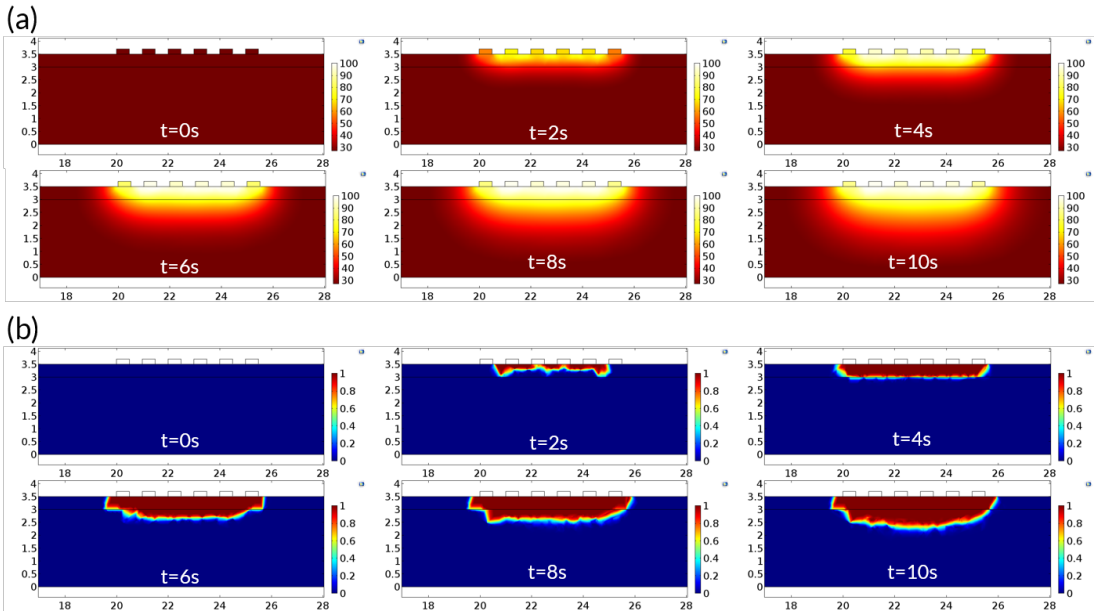

Figure 6.10: Simulated cross-sectional temperature profile (a) and necrotic tissue fraction (b) resulting from RF ablation with the 6-electrode bipolar RF array (25 V_{rms} applied for 10 s). Colorbar in (a) ranges from 25 °C to 100 °C; colorbar in (b) ranges from 0 to 1 (100% tissue damage).

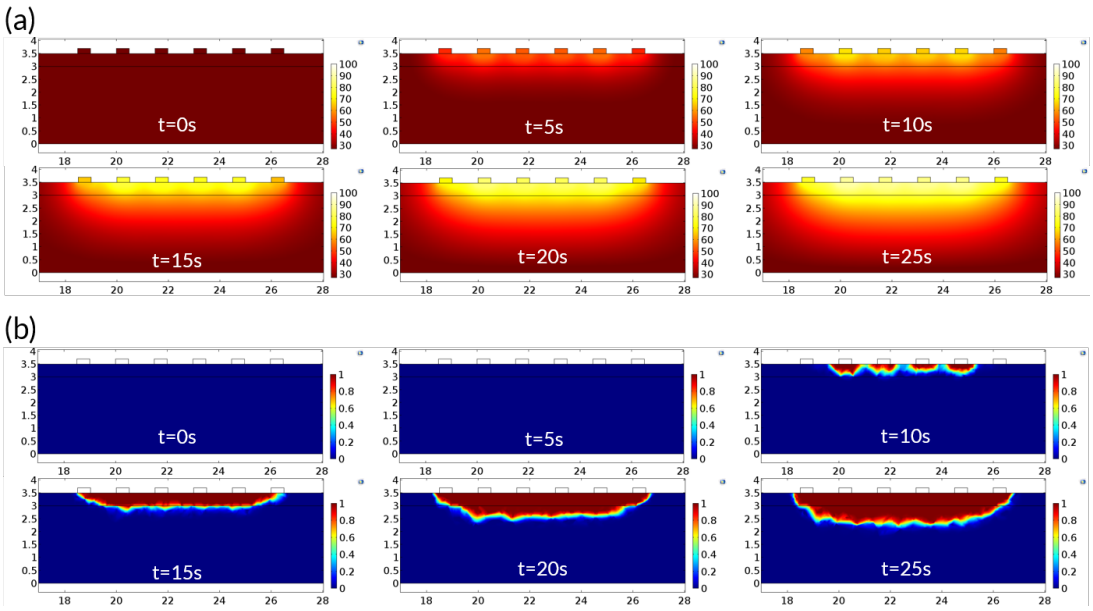

Figure 6.11: Simulated cross-sectional temperature profile (a) and necrotic tissue fraction (b) resulting from RF ablation with the 6-electrode bipolar RF array with increased electrode spacing of 1 mm (20 V_{rms} applied for 25 s). Colorbar in (a) ranges from 25 °C to 100 °C; colorbar in (b) ranges from 0 to 1 (100% tissue damage).

Next, the effect of increasing the electrode spacing was investigated. To illustrate this, the electrode spacing was increased from 500 μm to 1 mm, and a voltage of 20 V_{rms} was applied to the alternating active electrodes in the 6-electrode bipolar array. Figure 6.11 shows that the increase in electrode spacing led to a slower rise in temperature and tissue coagulation process. The temperature profile is further depicted in Fig. 6.12, which shows that an applied voltage of ~25 V_{rms} is required to achieve a similar temperature rise at an electrode spacing of 1 mm, compared to 20 V_{rms} at an electrode spacing of 500 μm (Fig. 6.5). The effect of changing the width of each electrode was also investigated. Here, the electrode width was modified from 500 μm to 250 μm, while keeping the spacing of electrodes at 500 μm. As shown in Figure 6.13, this has a minimal effect on the surface temperature (see Fig. 6.5), compared to the dramatic difference observed when the spacing of the electrodes was modified.

Finally, we modified the model geometry to a one-layer tissue slab with the following electrical

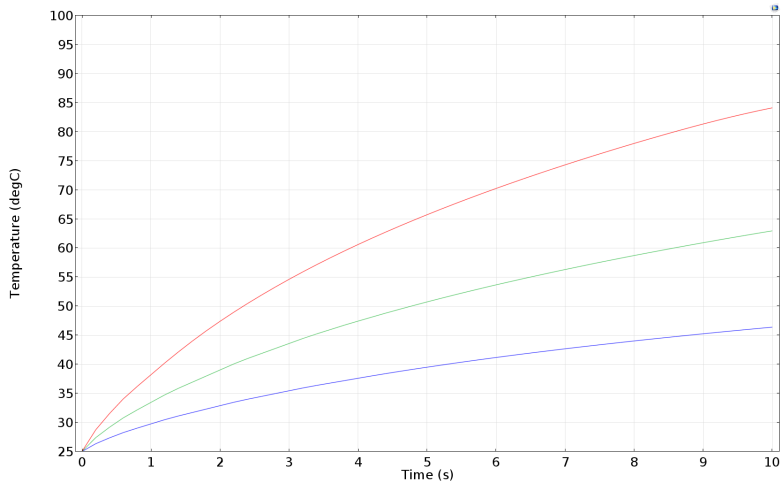

Figure 6.12: Simulated average surface temperature as a function of applied voltage (15, 20, 25 V_{rms} - bottom to top curves) with an increased electrode spacing. The bipolar radiofrequency electrode array consists of 6 electrodes (500 μm wide and 10 mm long, with a 1 mm spacing).

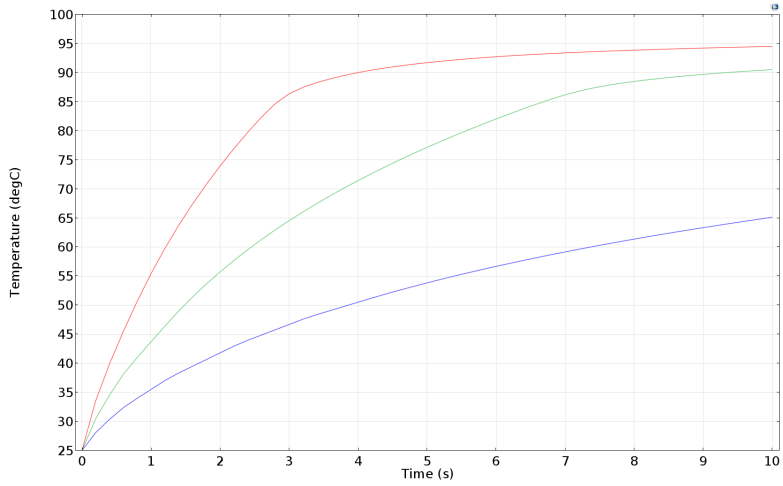

Figure 6.13: Simulated average surface temperature as a function of applied voltage (15, 20, 25 V_{rms} - bottom to top curves) with a smaller electrode width. The bipolar radiofrequency electrode array consists of 6 electrodes (250 μm wide and 10 mm long, with a 500 μm spacing).

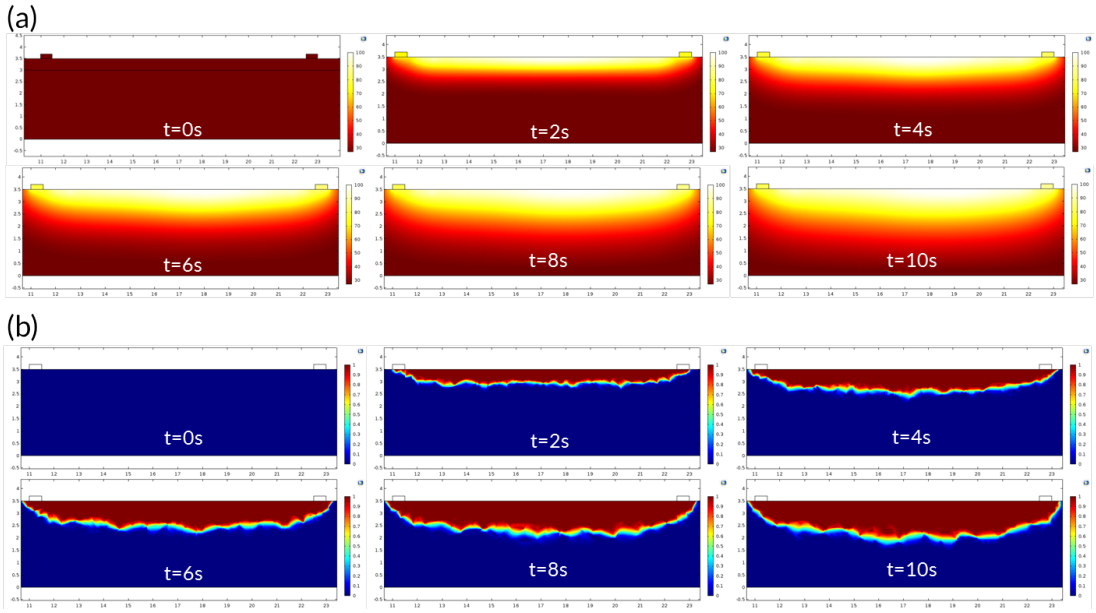

Figure 6.14: Simulated cross-sectional temperature profile (a) and necrotic tissue fraction (b) resulting from RF ablation with the 6-electrode bipolar RF array in the duodenum (20 V_{rms} applied for 10 s). Colorbar in (a) ranges from 25 °C to 100 °C; colorbar in (b) ranges from 0 to 1 (100% tissue damage).

and thermal properties: σ=0.55397 and k=0.49 (based on literature values for the small intestine[35,6]). Figure 6.14 shows that the temperature rise, as expected, was much faster due to the significant increase in electrical conductivity and the lesion growth rate was correspondingly much more noticeable within the first 2-4 s, compared to the case of the esophagus (Fig. 6.6) where the lesion was noticeable only after $\sim$ 5-6 s with the same set of ablation parameters.

Based on these set of simulation results, the final RF electrode prototype consists of 6 bipolar electrodes with a 500 μm spacing and 500 μm width to facilitate imaging between consecutive electrodes while enabling the generation of ablation lesions within a time frame of 5-10 s at an applied voltage of 20 to 25 V_{rms}. While an increased electrode spacing of 1 mm would further facilitate imaging, it would also necessitate greater driving RF voltage requirements to achieve the same ablation rate. Reducing the electrode width, however, has minimal advantages, given more electrodes, assuming the the same

spacing is used, will be needed to cover the same ablation area.

6.2 Balloon catheter RFA monitoring using CDV

Once the design of the prototype integrated therapy delivery and imaging device was validated, a catheter-based thermal therapy monitoring algorithm was developed to address the unique challenges in this setting. We developed a microscopic thermal therapy guidance platform that integrates a flexible bipolar radiofrequency ablation (RFA) electrode array around the clinical balloon OFDI catheter. Imaging was performed between consecutive electrodes in porcine esophagus *ex vivo*. We developed a therapy monitoring technique based on complex differential variance (CDV) that enables the direct, noninvasive visualization of the coagulation zone at high spatial resolution using real-time, dynamic fluctuations in the OFDI signals. This is contrary to conventional, temperature-based RFA monitoring techniques, which are often invasive and only provide an indirect measure of tissue injury, or emerging techniques (e.g., MR and US thermometry) limited by spatial resolution.

6.2.1 Experimental Setup and Processing Algorithm

Integrated OFDI-RFA balloon catheter

Figure 6.15 provides a schematic overview illustrating the design of the integrated OFDI-RFA balloon catheter used in this study, which incorporates a flexible bipolar RF electrode array around a clinical OFDI balloon catheter. The size of the balloon is 22 mm in diameter when inflated and the balloon catheter, which is approximately 2 m long, is connected to the optical system through a rotary junction on the proximal end. A bipolar RF electrode array, consisting of 6 electrodes in total (3 pairs of alternating electrodes in a bipolar RF configuration), was mounted on the outer surface of the balloon. Imaging was performed at the same location (without pull-back) between the consecutive electrodes at the center of the electrode array (electrodes 3 and 4 in the six electrode array).

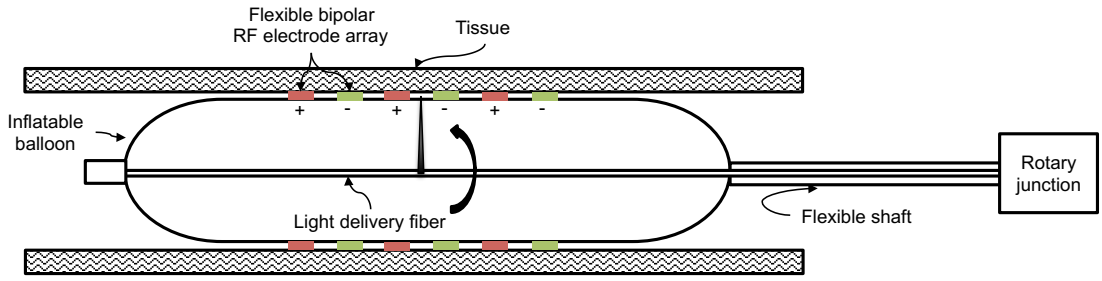

Figure 6.15: Integrated OFDI-RFA catheter with a bipolar radiofrequency (RF) electrode array on a flexible circuit around a clinical OFDI balloon catheter. Imaging is performed between alternating electrode pairs (+: active electrode, -: dispersive or ground electrode) to enable real-time microscopic image guidance.

The clinical OFDI system features an A-line rate of 50 kHz (3096 samples per A-line) and each B-scan consists of 4096 A-lines. This results in an effective imaging frame rate of 12.2 frames or B-scans per second at a rotation speed of 750 rpm. Porcine esophagus was used for the *ex vivo* experiments and NBTC histology (with eosin counterstain) was performed after embedding in optimum cutting temperature compound for frozen sections at 10 μm.

Processing Algorithm

Figure 6.16 shows the major steps in the processing algorithm needed to enable the visualization of the thermal coagulation zone in a clinical balloon catheter setting due to a series of challenges, most notably the non-uniformity in the rotation of the clinical OFDI catheter due to the use of a proximal scanning mechanism and a long flexible drive shaft. Due to the drift in the position of the first A-line in each frame, the first step requires the global registration across all frames using a fiducial mark on the surface on the balloon. In this case, one of the two rails connecting the alternating electrodes in the bipolar RF array on the surface (see Fig. 6.1), which conveniently casts a shadow on the sides of the electrodes in cross-sectional imaging, was used as the reference position across frames.

In step 2, once the frames were globally aligned using the fiducial mark, feature-based NURD correction (an extension of the earlier work on speckle-based NURD correction by Uribe-Pattarroyo et

al.[85]) was performed using the intensity OFDI tomograms to correct for misalignment between consecutive A-lines across frames due to the non-uniformity in the catheter rotation as follows:

1. SURF detection of features[8] in each frame (SURF is an accelerated variant of the SIFT feature descriptor[51])
2. KLT feature tracking algorithm across frames[52]
3. Median and spline filtering for smoothing the displacement vector *dx*
4. Interpolation of vector of *dx* from beginning to the end of each frame, with the boundary conditions that end points do not move (*dx* = 0 at edges of each frame)
5. Split complex tomogram in amplitude and phase and use the vector *dx* to interpolate each one to the corrected positions (to suppress the *dx* movement)
6. Merge amplitude and phase in a corrected complex tomogram for the subsequent calculation of CDV

In steps 3 and 4, the corrected complex tomogram was used to compute the CDV after calibration for SNR using a static region within the tissue of 40 x 20 pixels (depth and lateral dimensions) after downsampling the intensity image by 10 times in each dimension (or equivalently 400 x 200 pixels in the original intensity image of 2048 depth pixels x 4096 A-lines) using the same calibration technique presented in Chapter 5, M=2 consecutive B-scans, and a depth window size of 21 depth pixels (L=10). In each dataset, the initial 10 frames (when the RF energy source was off) were used for calibration purposes. The residual CDV noise was removed through background subtraction (which is estimated at around 0.1 in the air region) to improve the final calibration. Here, a lower number of consecutive B-scans was selected for the computation of CDV to maintain the temporal resolution given the clinical system only supports an A-line rate of 50 kHz (which results in an effective frame rate of 6 fps with 4096 A-lines/B-scan and M=2) and an averaging kernel was implemented across 4 adjacent frames (10 x 10 pixels x 4 frames) for each final CDV frame computed. Using the final CDV frames, the cumulative CDV was computed in Step 5, followed by the fusion of the CDV and cumulative CDV

with the intensity images and the circularization of the datasets for intuitive display in the clinical catheter setting.

6.2.2 Results

Figure 6.17 shows the ability to monitor the thermal coagulation process with calibrated CDV in the integrated OFDI-RFA catheter after correcting for NURD artifacts using the processing algorithm described previously. The rise in CDV was initially limited to the epithelium from t=7-8 s and reached the muscularis mucosa at the endpoint of the therapy at 10 s (with an applied voltage of 20 V_{rms} at 500 kHz). Upon cessation of therapy, the rapid drop in CDV was evident from t=10 s to 12s with some residual heating at t=11 s. The loss of the CDV signal shows one of the limitations of using the instantaneous CDV to visualize the coagulation zone. Hence, the cumulative CDV was also computed, as illustrated in Fig. 6.18, demonstrating the ability to more clearly visualize the evolution of the coagulation zone, especially after the RF energy was turned off at t=10 s.

To investigate the impact of the applied RF voltage on the time course of ablation, the RF voltage was increased to 25 V_{rms} at 500 kHz and the same experiment was repeated for an ablation time of 10 s. Figure 6.19 shows that the CDV signal became visible at $\sim$ 6-7 s, compared to $\sim$ 7-8 s at an applied RF voltage of 20 V_{rms}. The residual CDV was also slightly higher at t=11-12 s after the RF source was turned off at t = 10 s. The cumulative CDV (Fig. 6.20) further suggests that the thermal energy was deposited mostly in the epithelium up to $\sim$ 9 s and reached all the way through the muscularis mucosa by the end of the therapy (t=10-12 s).

Figure 6.21 shows the histological validation of the cumulative CDV maps for both power settings at 20 Vrms and 25 Vrms using NBTC staining, which demonstrates the accurate delineation of the thermal lesion using cumulative CDV. At 20 Vrms, the thermal coagulation zone extends beyond the lamina propria into the muscularis mucosa with a maximum lesion depth of $\sim$700 μm at the center, while at 25 Vrms, the coagulation zone extends all the way through the muscularis mucosa up to the

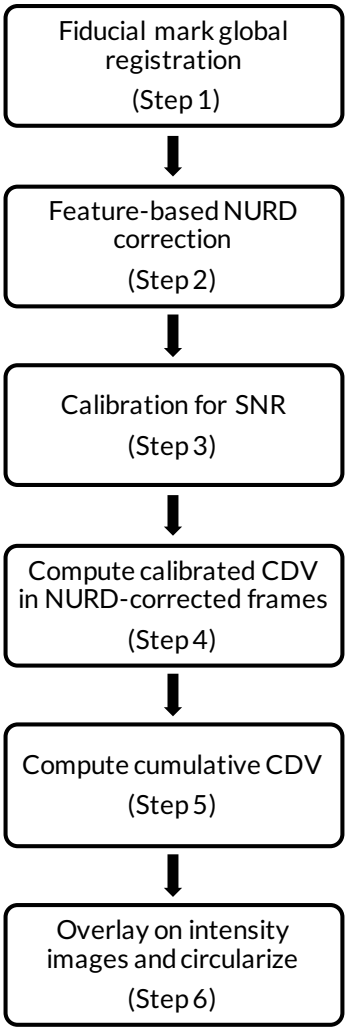

Figure 6.16: Overview of processing algorithm for monitoring the microscopic thermal lesion in a clinical catheter setting using calibrated CDV and feature-based NURD correction.

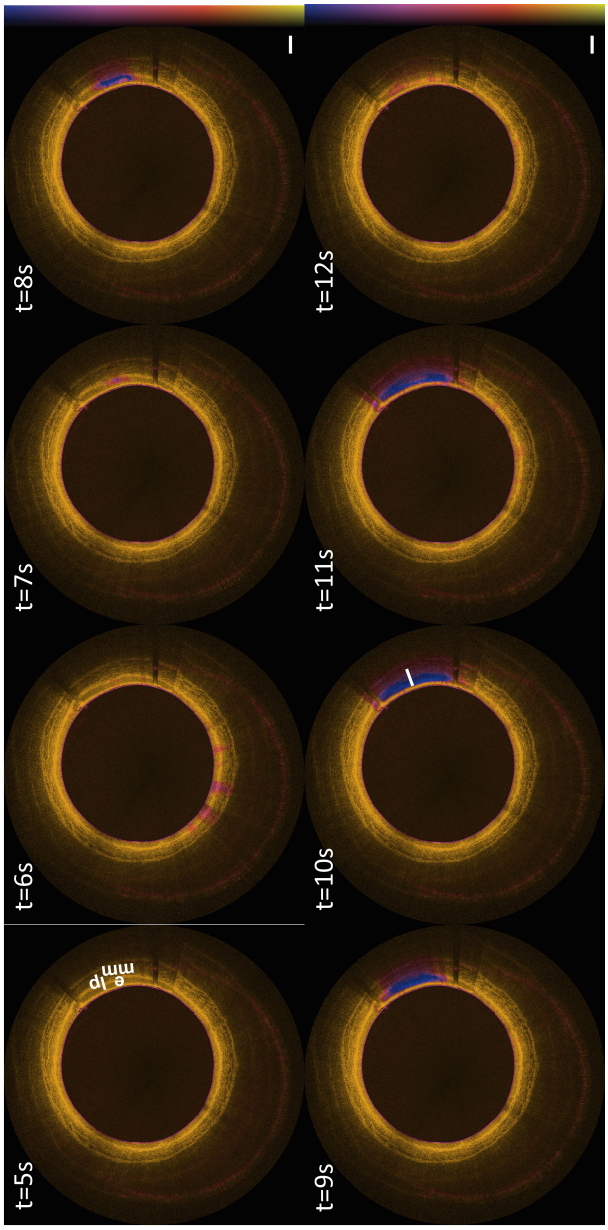

Figure 6.17: Radiofrequency ablation monitoring using calibrated CDV in a clinical balloon catheter, demonstrating the ability to clearly visualize the dynamics of thermal coagulation process in porcine esophagus *ex vivo*. Imaging was performed between the gaps of consecutive bipolar radiofrequency ablation electrodes (applied voltage = 20 V_{rms} at 500 kHz for 10 s) integrated around the OFDI balloon catheter. A region with increased CDV (purple) was observed at the center of the electrodes in the epithelium up to the lamina propria (t=7-8s) and eventually reaching slightly into the muscularis mucosa (t=9-10 s) . Imaging was performed until after the RF source was turned off (at t=10 s) to illustrate the rapid decrease in CDV. e, epithelium; lp, lamina propria; mm, muscularis mucosa. Color bars range from 0-0.5. Scale bars = 1 mm. The same scale bar is rotated and overlaid at t=10 s as a reference.

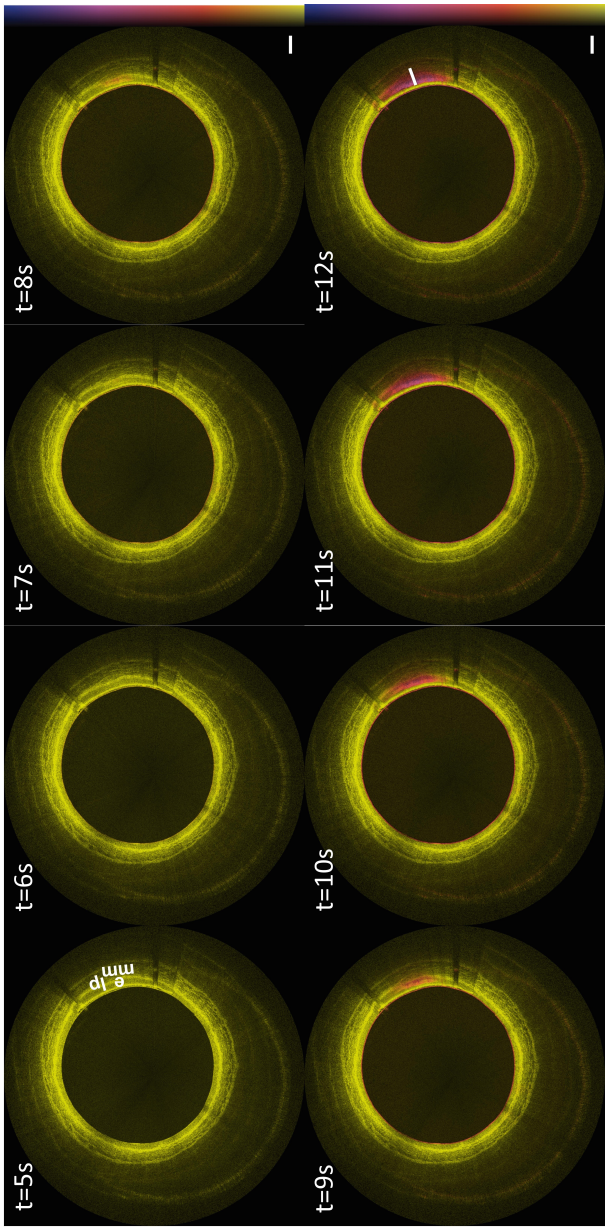

Figure 6.18: Radiofrequency ablation monitoring using cumulative CDV in a clinical balloon catheter, demonstrating the ability to more clearly visualize the evolution of thermal coagulation process in porcine esophagus *ex vivo*. Imaging was performed between the gaps of consecutive bipolar radiofrequency ablation electrodes (applied voltage = 20 V_{rms} at 500 kHz for 10 s) integrated around the OFDI balloon catheter. A growing region with increased cumulative CDV (purple) was observed in the epithelium and eventually reaching slightly into the muscularis mucosa. e, epithelium; lp, lamina propria; mm, muscularis mucosa. Color bars range from 0-20. Scale bars = 1 mm. The same scale bar is rotated and overlaid at t=12 s as a reference.

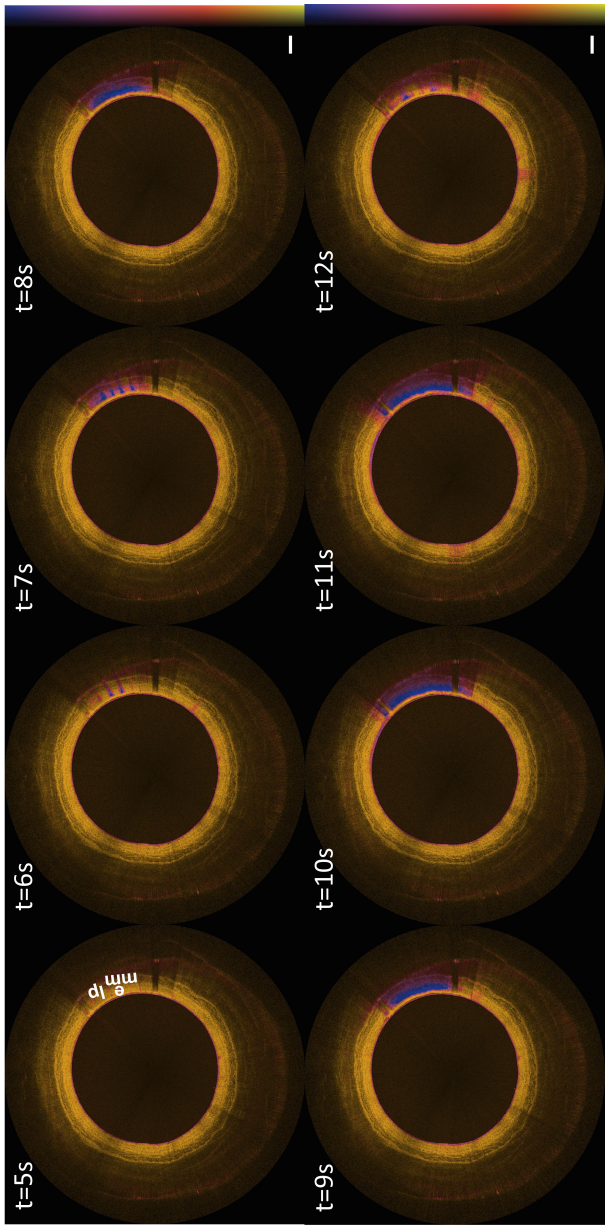

Figure 6.19: Radiofrequency ablation monitoring using calibrated CDV in a clinical balloon catheter, demonstrating the ability to clearly visualize the dynamics of thermal coagulation process in porcine esophagus *ex vivo*. Imaging was performed between the gaps of consecutive bipolar radiofrequency ablation electrodes (applied voltage = 25 V_{rms} at 500 kHz for 10 s) integrated around the OFDI balloon catheter. A region with increased CDV (purple) was observed at the center of the electrodes in the epithelium up to the lamina propria (t=6-7s) and eventually reaching all the way through the muscularis mucosa (t=8-10 s) . Imaging was performed until after the RF source was turned off (at t=10 s) to illustrate the rapid decrease in CDV. e, epithelium; lp, lamina propria; mm, muscularis mucosa. Color bars range from 0-0.5. Scale bars = 1 mm.

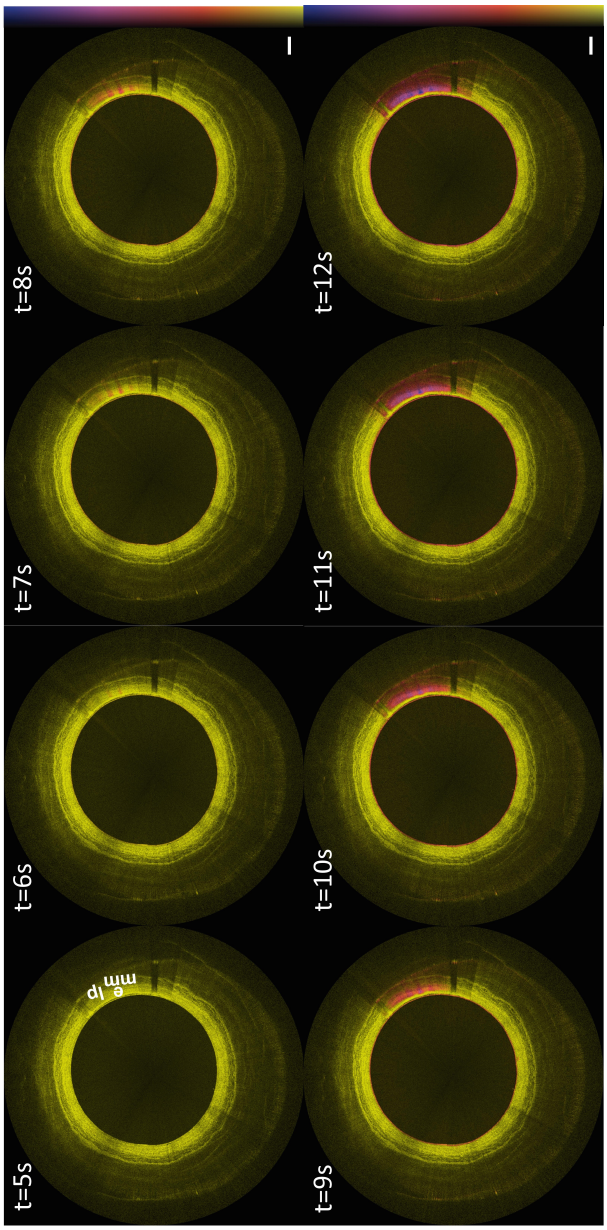

Figure 6.20: Radiofrequency ablation monitoring using cumulative CDV in a clinical balloon catheter, demonstrating the ability to more clearly visualize the evolution of thermal coagulation process in porcine esophagus *ex vivo*. Imaging was performed between the gaps of consecutive bipolar radiofrequency ablation electrodes (applied voltage = 25 V_{rms} at 500 kHz for 10 s) integrated around the OFDI balloon catheter. A growing region with increased cumulative CDV (purple) was observed in the epithelium and eventually reaching all the way through the muscularis mucosa. e, epithelium; lp, lamina propria; mm, muscularis mucosa. Color bars range from 0-20. Scale bars = 1 mm.

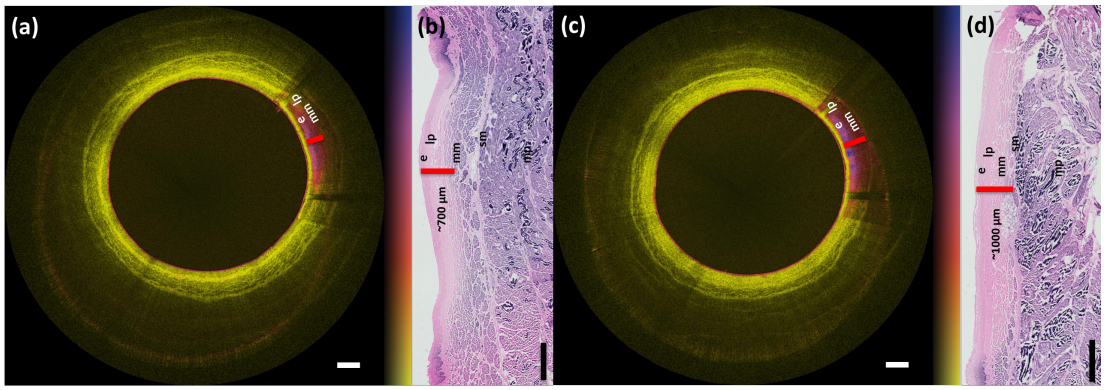

Figure 6.21: Histological validation of the coagulation zone delineated by cumulative CDV (a, c) at the treatment endpoint using NBTC staining (b, d). The estimated lesion depth (red bar; NBTC-negative region in pink) is $\sim$ 700 μm at 20 V_{rms} and $\sim$ 1000 μm at 25 V_{rms}. e, epithelium; lp, lamina propria; mm, muscularis mucosa; sm, submucosa; mp, muscularis propria. Scale bars = 1 mm.

submucosa with a lesion depth of $\sim$1000 μm.

Given our goal to apply this technique clinically to the treatment of Barrett's esophagus, which is characterized by intestinal metaplasia, we further tested the CDV-based technique in porcine duodenum *ex vivo*. Figure 6.22 shows the temporal evolution of the CDV in the duodenum, which is more rapid compared to the esophagus at the same applied voltage of 20 V_{rms} (Fig. 6.17). In the case of the duodenum, the rise in CDV was evident beginning at t=2-4 s, and spreading across the electrode surface by t=6 s. From t=6-10 s, the CDV remained high until the RF energy was turned off at t=10 s, after which a dramatically reduced CDV was observed with some residual heating from t=11-12 s. Figure 6.23 shows the growth of the thermal lesion using the cumulative CDV, which suggests a visible lesion after $\sim$ 6-8 s of heating and a stable lesion by t=10 s with minimal residual growth after the RF energy was turned off.

6.2.3 Discussion

Using our integrated balloon OFDI-RFA therapy delivery and guidance system, we demonstrated direct, label-free visualization of the thermal coagulation process during RFA ablation at high resolu-

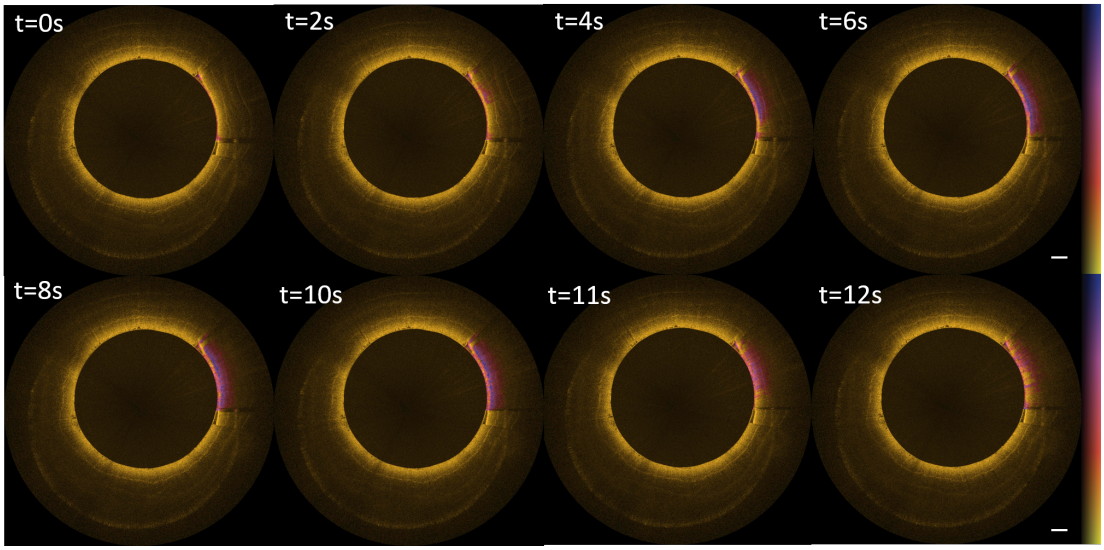

Figure 6.22: Radiofrequency ablation monitoring in porcine duodenum *ex vivo* using calibrated CDV in a clinical balloon catheter. Imaging was performed between the gaps of consecutive bipolar radiofrequency ablation electrodes (applied voltage = 20 V_{rms} at 500 kHz for 10 s) integrated around the OFDI balloon catheter. Imaging was performed until after the RF source was turned off at t=10 s. Color bars range from 0-0.5. Scale bars = 1 mm.

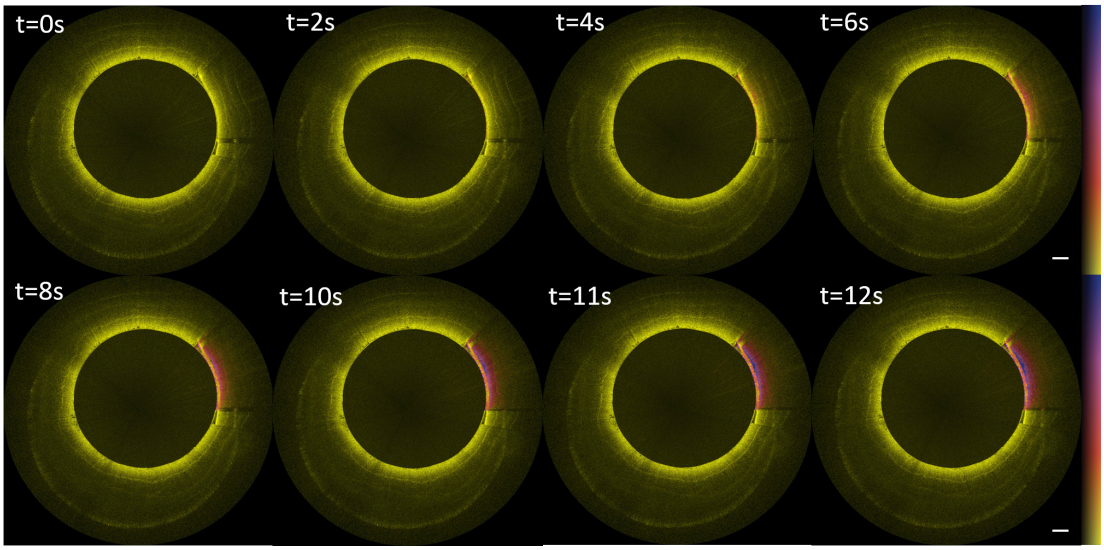

Figure 6.23: Radiofrequency ablation monitoring in porcine duodenum *ex vivo* using cumulative CDV in a clinical balloon catheter. Imaging was performed between the gaps of consecutive bipolar radiofrequency ablation electrodes (applied voltage = 20 V_{rms} at 500 kHz for 10 s) integrated around the OFDI balloon catheter. Color bars range from 0-20. Scale bars = 1 mm.

tion with the NURD-corrected, calibrated CDV as well as cumulative CDV metric in both porcine esophagus and porcine duodenum *ex vivo*. By imaging between the consecutive electrodes in a flexible RF bipolar array around the balloon OFDI catheter, we showed the ability to tailor the injury depth by varying the applied RF voltage. For example, by increasing the voltage from 20 V_{rms} to 25 V_{rms}, the injury depth was increased significantly from the epithelium (up to the lamina propria) to the muscularis mucosa (up to the submucosa) after an ablation time of 10 seconds, as validated by NBTC histology. We also investigated the effect of different tissue types on the ablation process by testing the same set of parameters (20 V_{rms} for 10 s) in porcine esophagus and duodenum, which showed a much more rapid response in the case of the duodenum. This is due to the significantly higher electrical conductivity of duodenum (0.55397 S/m) reported in the literature compared to the mucous membrane (0.1778 S/m) of the esophagus[6].

The ability to clearly visualize the evolution of the thermal lesion using the cumulative CDV metric also translates to the ability to control the RFA therapy depth with real-time imaging feedback. This is critical as tissue contact with the RFA electrodes can become variable in the clinical setting and the presence of mucus will likely change the electrical conductivity, both of which directly impact the actual therapy delivery and achieved therapy depth with any given set of ablation parameters. The current use of predetermined RF ablation energy in the clinical setting for the treatment of Barrett's esophagus with dysplasia, without any real-time monitoring or guidance beyond surface-based examination with conventional endoscopy, leads to significant variations in treatment outcomes, as evidenced by the range of stricture formation rates from 2 - 8 % reported in the literature[75]. The ability to delineate thermal lesions at high resolution opens up the possibility of performing microscopic image-guided procedures in numerous epithelial lesions, beyond Barrett's esophagus, where the precise delivery of thermal energy is critical.

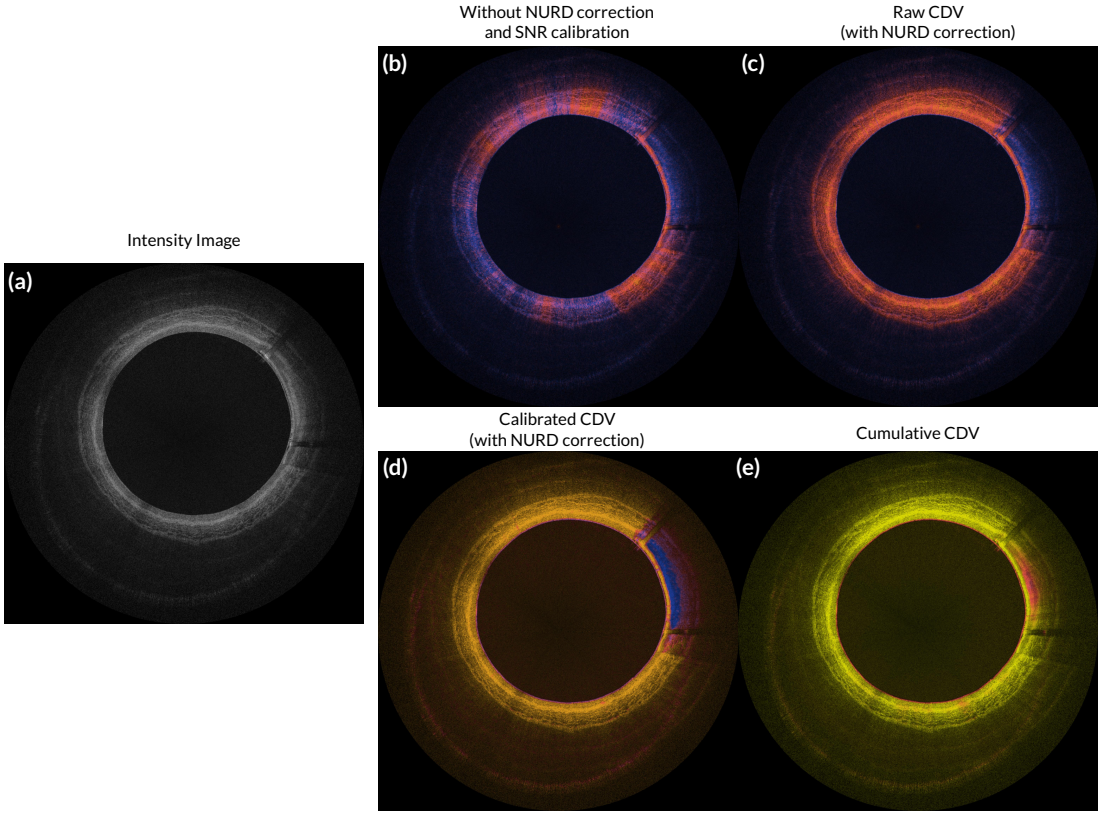

Figure 6.24: Impact of NURD correction and SNR calibration: (a) Intensity OCT image; (b) CDV computation without NURD correction and SNR calibration; (c) Raw CDV after NURD correction; (d) Calibrated CDV after NURD correction; (e) Visualization of the thermal lesion using cumulative CDV.

6.3 Summary

This chapter presented a framework for microscopic image guidance that has direct clinical translational potential. Through the construction of an FEM model, the effects of varying a set of important RF ablation parameters for a bipolar RF electrode array were investigated systematically, including the driving RF voltage and the spacing of electrodes on the ablation duration. The model also provided a convenient means to visualize the three-dimensional temperature profile as well as the necrotic tissue fraction as a function of time for different sets of parameters. Based on these simulation results, a six-electrode array with an even spacing of 500 μm was fabricated as a flexible circuit. Using this flexible bipolar RF array, the FEM model was validated by measuring the surface temperature profile with an infrared camera, showing close correspondence between the simulated average surface temperature and the measured surface temperature across the electrode array. Finally, the flexible bipolar RF array was integrated around a clinical OFDI balloon catheter for feasibility testing *ex vivo* and imaging was performed between the gap of consecutive electrodes at the center of the array. The significance of proper NURD correction and SNR calibration is clearly depicted in Fig. 6.24, which shows the results prior to and after these critical motion and noise compensation techniques to be able to visualize the thermal coagulation zone using the CDV-based algorithm. The final results were very promising for a series of parameters tested (including different driving RF voltage) in both porcine esophagus and porcine duodenum, demonstrating the ability to clearly visualize the progress of the therapy using the calibrated CDV after NURD correction and the ability to monitor the therapy depth using the cumulative CDV metric.

7

Conclusions

In this dissertation, two frameworks for enabling the notion of *microscopic image guidance* were introduced. The first conceptual framework, discussed in Chapter 2, presents a machine learning-based approach aimed to enable real-time navigational guidance through *laser-printed* patterns and subsequent *microscopic* examination of a suspicious target lesion through the co-registration of subsurface imaging datasets, such as OFDI datasets, with endoscopic image sequences. The successful implementation of such a framework would enable the concept of a virtual biopsy at any desirable location during video endoscopy procedures and more targeted biopsy and focal treatment of suspicious lesions. While a number of important challenges were addressed in Chapter 2, the practical, clinical implementation of this framework requires future work in areas discussed in the next section. The second framework, discussed from Chapters 3 through 6, presents an integrated *microscopic image guidance*

system that culminates into a clinical balloon-catheter based implementation in Chapter 6, which has very clear clinical translational potential based on promising *ex vivo* results. While our primary focus has been the treatment of Barrett's esophagus with dysplasia and the use of radiofrequency ablation as the thermal therapy modality, the interesting results from Chapters 3 to 5 suggest that this framework can be expanded to other clinical applications for the treatment of other epithelial lesions, such as hypertrophic scars or diabetic retinopathy, potentially with other thermal therapy modalities, such as laser thermal therapy, microwave ablation, and high-intensity focused ultrasound. A summary of the major contributions of this dissertation, along with ideas for future avenues of research, will be provided in the following sections.

7.1 Navigational guidance through laser painting and machine learning

The significant challenges in the endoscopic setting, such as the significant deformation of the esophagus, partial occlusion, and viewpoint changes during endoscopy, necessitated a very different approach to image registration. In Chapter 2, a potential solution to address these challenges during conventional endoscopy was implemented. This solution consisted of two components:

1. A noninvasive laser-printing technique: to create set of robust navigational landmarks
2. A machine learning algorithm: to classify these landmarks for localization

The noninvasive laser printing/painting approach involves the idea of photobleaching light-sensitive chromoendoscopy dyes used in Barrett's esophagus patients and the creation of a biodegradable, nontoxic spray-on PLGA-based substrate integrating these dyes to generate a water-resistant film. Through experimentation, it was found that many of these clinically used chromoendoscopy dyes, such as crystal violet, methylene blue or toluidine blue, can be readily photobleached with a low-cost, low-power diode laser at 635 nm. By focusing this laser beam on the tissue sprayed with the custom-made water-resistant PLGA-dye substrate, the ability to perform laser printing of an arbitrarily complex design

pattern, such as the MGH logo or HMS logo, was demonstrated *ex vivo* in a benchtop setup. A series of design patterns of navigational landmarks were generated and a dataset of over 1000 images representative of realistic endoscopic setting (simulating cases of deformation, partial occlusion and viewpoint changes) was created for subsequent algorithmic development and testing.

Two machine learning frameworks were investigated for the classification of the different navigational landmarks: 1) a bag of words model[17] in which a dictionary of visual words is constructed to train the computer vision algorithm to classify different navigational landmarks, 2) a simplified vectorized histogram of oriented gradient (HOG) approach. While both approaches provide a framework to classify between different landmarks tested and potentially enable navigational guidance using the classification results as demonstrated in a sample video sequence, a number of challenges remain to be solved to enable its use clinically as a robust navigational guidance platform:

1. Compact encoding of spatial location in a highly confined endoscopic setting
2. Improvement of classification accuracy as the number of classes (distinct navigational landmarks) increases
3. Catheter-based implementation of laser printing *in vivo*
4. Potential innovation in endoscopic probe design to minimize deformation of the esophagus during endoscopy

To address the compact encoding problem, in Chapter 2, I proposed a new design of navigational landmarks that contains a set of features: 1) orientation marker (to maximize the number of distinct combinations that can be encoded in the center of the pattern), 2) calibration marks around bounding region (to correct for affine transformation or deformation before classification to improve classification accuracy), 3) a binary location encoding scheme (in which a 3 x 3 grid would, for example, give rise to 2^9 combinations), 4) color encoding in addition to shape-based encoding (to greatly increase the number of combinations). An important advantage of the latter 2 approaches is the significant simplification of the classification algorithm. For example, using a binary encoding scheme, a machine

learning approach is likely unnecessary if one could properly correct for deformation using the calibration marker. However, the mode of operation would be different since the endoscopist must zoom into the region of interest so that the binary code can be "scanned" with the camera to retrieve the real-time location. In addition, color-based encoding would greatly simplify location tracking, serve as as a redundancy check, or provide a coarser, global location encoding followed by more precise localization using the binary code once the region is zoomed in. Unfortunately, to enable color encoding, the proposed laser printing approach by photobleaching light-sensitive dyes would likely not be feasible. Instead, the prefabrication of tracking patterns on a biodegradable tissue adhesive may provide a more flexible solution to integrate many colors in a more easily controlled environment prior to deployment in the esophagus.

An important advantage of a machine learning approach is that the computer vision algorithm can be trained to be increasingly intelligent through the expansion of the training dataset over time. In the current implementation, it was observed that classification accuracy deteriorates with design patterns that are too similar, which worsens as the number of classes (i.e. number of design patterns) increases. However, with the new compact encoding scheme discussed above, this problem may be mitigated.

To enable laser printing *in vivo*, a novel catheter design is also required. Chapter 2 depicted a double-balloon catheter design to enable high-speed, high-resolution laser printing *in vivo* where a focused light beam is delivered to the tissue sprayed with the chromoendoscopy dye-PLGA construct. Here, it is interesting to note that NURD artifacts may compromise high-fidelity printing in a catheter-based setting. Unlike the case of therapy monitoring, NURD correction is not feasible. The most viable solution is to construct a more stable catheter with a distal micromotor scanning mechanism[83]. Another interesting avenue of future work involves integrating a dual clad fiber to enable laser printing and imaging in one catheter[9].

Finally, while the focus thus far has been to overcome many of the clinical challenges associated with conventional endoscopy, innovation in the endoscopy hardware itself may provide the ultimate

solution. For example, if the deformation of the esophagus can be controlled more elegantly through modification of the hardware, the algorithmic/software problem would be significantly simplified. For example, a dual-balloon design in which the endoscopy camera is situated between two stabilizing balloons may enable endoscopic examination in a much more controlled setting while still enabling conventional procedures such as biopsy to be performed.

7.2 Balloon catheter-based RFA monitoring

It was interesting that concepts developed in the machine learning framework (e.g., feature tracking) also provided insights to one of the critical problems in the second, integrated framework for microscopic image guidance, where an integrated OFDI-RFA catheter was developed to enable the precise delivery of thermal energy to the target lesion. Here, the challenges associated with deformation were mitigated by inflating the balloon around the region to be treated, thereby stabilizing the instrumentation, but the non-uniformity in the rotation (NURD artifacts) of the catheter remains. In this section, the challenges and solutions in the development of the second framework, along with outlook for future work, will be summarized.

7.2.1 Laser thermal therapy and hypertrophic scar monitoring using PS-OFDI

In Chapters 3 and 4, polarization-sensitive optical frequency domain imaging (PS-OFDI) was first investigated as a technique for laser thermal therapy and hypertrophic scar monitoring. In particular, two metrics — local retardation and degree of polarization (DOP) — were demonstrated to correlate histologically with the disruption of the fibrillar collagen architecture. For example, thermal coagulation of collagen in the skin was characterized by a decrease in local retardation (due to the loss of tissue birefringence) and increase in DOP. In addition, in Chapter 4, PS-OFDI was demonstrated for the 3D,

longitudinal assessment of collagen remodeling in both an incisional HTS model for 1 month and excisional HTS model after 6 months. HTS was characterized by an initially low local retardation, which increased as collagen fibers remodeled, and a persistently high degree of polarization. Therefore, PS-OFDI serves a powerful tool to gain significant biological insights into HTS remodeling by enabling longitudinal assessment of collagen *in vivo* critical to elucidating HTS etiology and developing more effective HTS therapies.

7.2.2 Laser thermal therapy monitoring using CDV

While the results were very promising for dermatology applications, the use of PS-OFDI for the delineation of thermal lesions in diverse tissue types, such as the esophagus where the baseline tissue birefringence is low, remains challenging. Therefore, in Chapter 5, an approach to accurately visualize the thermal coagulation process at high resolution using complex differential variance (CDV) was developed to map the dynamic signal fluctuations induced by thermal therapy, which can be widely applied to different tissue types and different thermal therapies including laser therapy and radiofrequency ablation as demonstrated in this dissertation. The CDV-based technique was demonstrated for 3 different tissue types (skin, retina, and esophagus) using a thulium laser therapy monitoring setup in a benchtop configuration. This opens up the possibility of performing microscopic image-guided procedures in many clinical applications, ranging from photocoagulation in diabetic retinopathy, treatment of hypertrophic scars, to the oncologic treatment of numerous dysplastic lesions such as Barrett's esophagus with dysplasia.

An interesting avenue for future work that integrates principles from Chapters 3 to 5 is the combination of PS-OFDI based HTS monitoring with the CDV-based real-time therapy depth control to improve hypertrophic scar treatment. For example, the CDV-based technique can be used to accurately tailor the treatment depth in real-time during the treatment session to better account for inter-patient variability (given standardized treatment parameters are currently used) and PS-OFDI

can be used to monitor the collagen remodeling process longitudinally to assess treatment response over the course of the therapy.

7.2.3 Translation to clinical balloon catheter setting

The final translation of the CDV-based technique to the clinical balloon catheter setting required the integration of a number of principles developed throughout the dissertation as well as a number of additional innovations:

1. FEM-based RF ablation modeling
2. Design and fabrication of a custom bipolar RF electrode array on a flexible circuit
3. Feature-based NURD correction in the integrated OFDI-RFA catheter
4. SNR calibration for CDV computation
5. Histological validation of cumulative CDV metric

The construction of a finite element based model provided a convenient means to systematically study the impact of various design parameters, such as the spacing of electrodes, on the voltage requirements and anticipated duration of therapy. This model significantly simplified the validation stage in the final RF electrode design and significantly reduced the cost of the flexible circuit fabrication (which is on the order of several thousand dollars per design iteration). This simulation and modeling stage led to the design of a prototype bipolar RF electrode array that enabled simultaneous imaging between electrode gaps (500 μm) within a driving voltage of 20-25 V_{rms} for an ablation time of 5-10 seconds only.

The next major challenge involved solving the significant NURD artifacts due to the proximal scanning mechanism and long flexible drive shaft of the clinical OFDI balloon catheter. Feature-based tracking using SURF descriptors and the KLT feature tracking algorithm provided a framework for the estimation of the displacement of A-lines between frames induced by the non-uniformity of the

rotation. Combined with the SNR calibration technique introduced in Chapter 5, the thermal coagulation process was successfully mapped using the NURD-corrected, SNR-calibrated CDV processing algorithm in an *ex vivo* setting in both porcine esophagus and porcine duodenum. Histological validation using NBTC staining confirmed a coagulation zone consistent with the cumulative CDV analysis.

The results from the *ex vivo* demonstration provide the impetus for further *in vivo* testing in the future. To translate this microscopic guidance framework to the final clinical treatment of Barrett's esophagus patients, a number of future directions include:

1. Demonstration of integrated OFDI-RFA catheter in an animal model *in vivo*
2. Creation of more sophisticated RF electrode arrays enabling highly conformal therapy depth control
3. Treatment planning and ablation zone monitoring across a large treatment volume

The demonstration of the integrated OFDI-RFA catheter in a swine model *in vivo* is a major milestone to prove the clinical feasibility of the approach. A number of challenges may arise in this setting, including the presence of motion artifacts due to respiratory motion of the living animal and more severe NURD artifacts due to the bending and movements of the flexible drive shafts. To solve the first problem, the feature-based tracking algorithm can be extended to estimate motion beyond the displacement between A-lines (dx) across frames due to NURD to include bulk motion correction. The increased severity of NURD artifacts, if proven too severe for robust feature-based NURD correction, can be solved by redesigning the clinical catheter to incorporate a distal micromotor scanning mechanism[83] to increase the stability of the rotation.

In addition, to realize the vision of highly conformal RF therapy in BE patients, further work on custom electrode designs that enable individualized ablation zone control would be needed. One potential idea involves the design of concentric rings of bipolar RF electrodes with individually controlled zones, each of which can be tailored to a different driving RF voltage or duration to achieve the desired

ablation depth. By combining these variable ablation depths concentrically, a highly conformal dose contour could be achieved to optimally cover the dysplastic site.

Finally, a number of interesting future directions revolve around the treatment planning problem such as the segmentation of the BE with dysplasia regions and the planning of dose contours on the target volume as well as the determination of optimal margins. In addition, the ability to automate the therapy delivery, monitoring, and feedback mechanism across a large ablation segment would be greatly beneficial for the ultimate clinical adoption of this technology.

In the new era of precision medicine, the ability to tailor treatment at unprecedented levels of precision will open up many new clinical applications. While I have focused on one precancerous lesion called Barrett's esophagus with dysplasia (which leads to a highly lethal cancer in the esophagus) throughout this dissertation, the techniques and frameworks developed can be translated to other epithelial lesions, ranging from hypertrophic scars through precise fractional laser therapy guidance, lesions in the eye such as diabetic retinopathy where laser photocoagulation is used, to various high-risk lesions accessible by a catheter-based or needle-based approach in interventional oncology and beyond.

References

[1] Aarabi, S., Bhatt, K. A., Shi, Y., Paterno, J., Chang, E. I., Loh, S. A., Holmes, J. W., Longaker, M. T., Yee, H., & Gurtner, G. C. (2007). Mechanical load initiates hypertrophic scar formation through decreased cellular apoptosis. *The FASEB Journal*, 21(12), 3250–3261.

[2] Ahmad, I., Gribble, A., Ikram, M., Pop, M., & Vitkin, A. (2016). Polarimetric assessment of healthy and radiofrequency ablated porcine myocardial tissue. *Journal of biophotonics*, 9(7), 750–9.

[3] Alex, A., Považay, B., Hofer, B., Popov, S., Glittenberg, C., Binder, S., & Drexler, W. (2010). Multispectral in vivo three-dimensional optical coherence tomography of human skin. *Journal of Biomedical Optics*, 15(2), 26015–26025.

[4] An, L., Subhush, H. M., Wilson, D. J., & Wang, R. K. (2010). High-resolution wide-field imaging of retinal and choroidal blood perfusion with optical microangiography. *Journal of biomedical optics*, 15(2), 026011–026011.

[5] Anderson, R. R., Donelan, M. B., Hivnor, C., Greeson, E., Ross, E. V., Shumaker, P. R., Uebelhoer, N. S., & Waibel, J. S. (2014). Laser treatment of traumatic scars with an emphasis on ablative fractional laser resurfacing: consensus report. *JAMA dermatology*, 150(2), 187–193.

[6] Andreuccetti, D., Fossi, R., & Petrucci, C. (1997). An Internet resource for the calculation of the dielectric properties of body tissues in the frequency range 10 Hz - 100 GHz (based on data published by C.Gabriel et al. in 1996). *Website at http://niremf.ifac.cnr.it/tissprop/. IFAC-CNR, Florence (Italy).*

[7] Bao, A., Goins, B., Dodd, G. D., Soundararajan, A., Santoyo, C., Otto, R. A., Davis, M. D., & Phillips, W. T. (2008). Real-time iterative monitoring of radiofrequency ablation tumor therapy with 15O-water PET imaging. *Journal of Nuclear Medicine*, 49(10), 1723–1729.

[8] Bay, H., Tuytelaars, T., & Van Gool, L. (2006). SURF: Speeded up robust features. In *European conference on computer vision* (pp. 404–417).: Springer.

[9] Beaudette, K., Baac, H. W., Madore, W.-J., Villiger, M., Godbout, N., Bouma, B. E., & Boudoux, C. (2015). Laser tissue coagulation and concurrent optical coherence tomography through a double-clad fiber coupler. *Biomedical optics express*, 6(4), 1293–1303.

[10] Berjano, E. J. (2006). Theoretical modeling for radiofrequency ablation: state-of-the-art and challenges for the future. *Biomedical engineering online*, 5, 24.

[11] Bezerra, H. G., Costa, M. A., Guagliumi, G., Rollins, A. M., & Simon, D. I. (2009). Intracoronary optical coherence tomography: a comprehensive review: clinical and research applications. *JACC: Cardiovascular Interventions*, 2(11), 1035–1046.

[12] Brown, M. & Lowe, D. G. (2007). Automatic panoramic image stitching using invariant features. *International journal of computer vision*, 74(1), 59–73.

[13] Burschka, D., Li, M., Ishii, M., Taylor, R. H., & Hager, G. D. (2005). Scale-invariant registration of monocular endoscopic images to ct-scans for sinus surgery. *Medical Image Analysis*, 9(5), 413–426.

[14] Chang, K. J., Nguyen, P., Erickson, R. A., Durbin, T. E., & Katz, K. D. (1997). The clinical utility of endoscopic ultrasound–guided fine-needle aspiration in the diagnosis and staging of pancreatic carcinoma. *Gastrointestinal endoscopy*, 45(5), 387–393.

[15] Chen, G., Chen, J., Zhuo, S., Xiong, S., Zeng, H., Jiang, X., Chen, R., & Xie, S. (2009). Nonlinear spectral imaging of human hypertrophic scar based on two-photon excited fluorescence and second-harmonic generation. *British Journal of Dermatology*, 161(1), 48–55.

[16] Collins, F. S. & Varmus, H. (2015). A new initiative on precision medicine. *New England Journal of Medicine*, 372(9), 793–795.

[17] Csurka, G., Dance, C., Fan, L., Willamowski, J., & Bray, C. (2004). Visual categorization with bags of keypoints. In *Workshop on statistical learning in computer vision, ECCV*, volume 1 (pp.22̄).

[18] Dalal, N. & Triggs, B. (2005). Histograms of oriented gradients for human detection. In *2005 IEEE Computer Society Conference on Computer Vision and Pattern Recognition (CVPR'05)*, volume 1 (pp. 886–893).: IEEE.

[19] De Boer, J., Srinivas, S., Malekafzali, A., Chen, Z., & Nelson, J. (1998). Imaging thermally damaged tissue by polarization sensitive optical coherence tomography. *Optics express*, 3(6), 212–218.

[20] de Senneville, B. D., Mougenot, C., Quesson, B., Dragonu, I., Grenier, N., & Moonen, C. T. (2007). MR thermometry for monitoring tumor ablation. *European radiology*, 17(9), 2401–2410.

[21] Dewhirst, M., Viglianti, B., Lora-Michiels, M., Hanson, M., & Hoopes, P. (2003). Basic principles of thermal dosimetry and thermal thresholds for tissue damage from hyperthermia. *International Journal of Hyperthermia*, 19(3), 267–294.

[22] Durrant-Whyte, H. & Bailey, T. (2006). Simultaneous localization and mapping: part i. *Robotics & Automation Magazine, IEEE*, 13(2), 99–110.

[23] Ehrlich, H. P., Desmoulière, A., Diegelmann, R. F., Cohen, I. K., Compton, C. C., Garner, W. L., Kapanci, Y., & Gabbiani, G. (1994). Morphological and immunochemical differences between keloid and hypertrophic scar. *The American Journal of Pathology*, 145(1), 105–113.

[24] El-Serag, H. B., Sweet, S., Winchester, C. C., & Dent, J. (2014). Update on the epidemiology of gastro-oesophageal reflux disease: a systematic review. *Gut*, 63(6), 871–80.

[25] English, R. S. & Shenefelt, P. D. (1999). Keloids and Hypertrophic Scars. *Dermatologic Surgery*, 25(8), 631–638.

[26] Fleming, C. P., Quan, K. J., & Rollins, A. M. (2013a). Toward guidance of epicardial cardiac radiofrequency ablation therapy using optical coherence tomography. *Journal of biomedical optics*, 15(4), 041510–041510.

[27] Fleming, C. P., Quan, K. J., Wang, H., Amit, G., & Rollins, A. M. (2010). In vitro characterization of cardiac radiofrequency ablation lesions using optical coherence tomography. *Optics express*, 18(3), 3079–3092.

[28] Fleming, C. P., Wang, H., Quan, K. J., & Rollins, A. M. (2013b). Real-time monitoring of cardiac radio-frequency ablation lesion formation using an optical coherence tomography forward-imaging catheter. *Journal of biomedical optics*, 15(3), 030516–030516.

[29] Fu, X., Wang, Z., Wang, H., Wang, Y. T., Jenkins, M. W., & Rollins, A. M. (2014). Fiber-optic catheter-based polarization-sensitive oct for radio-frequency ablation monitoring. *Optics letters*, 39(17), 5066–5069.

[30] Gambichler, T., Orlikov, A., Vasa, R., Moussa, G., Hoffmann, K., Stücker, M., Altmeyer, P., & Bechara, F. G. (2007). In vivo optical coherence tomography of basal cell carcinoma. *Journal of Dermatological Science*, 45(3), 167–173.

[31] Gauglitz, G. G., Korting, H. C., Pavicic, T., Ruzicka, T., & Jeschke, M. G. (2011). Hypertrophic scarring and keloids: pathomechanisms and current and emerging treatment strategies. *Molecular medicine*, 17(1-2), 113–125.

[32] Geissbuehler, M. & Lasser, T. (2013). How to display data by color schemes compatible with red-green color perception deficiencies. *Optics Express*, 21(8), 9862–9874.

[33] Gong, P., McLaughlin, R. A., Liew, Y. M., Munro, P. R. T., Wood, F. M., & Sampson, D. D. (2014). Assessment of human burn scars with optical coherence tomography by imaging the attenuation coefficient of tissue after vascular masking. *Journal of biomedical optics*, 19(2), 21111.

[34] Götzinger, E., Pircher, M., Geitzenauer, W., Ahlers, C., Baumann, B., Michels, S., Schmidt-Erfurth, U., & Hitzenberger, C. K. (2008). Retinal pigment epithelium segmentation bypolarization sensitive optical coherencetomography. *Optics Express*, 16(21), 16410–16422.

[35] Hasgall, P., Neufeld, E., Gosselin, M., Klingenböck, A., & Kuster, N. (2015). IT'IS Database for thermal and electromagnetic parameters of biological tissues. *IT'IS Foundation Version 3.0 website: www.itis.ethz.ch/database*.

[36] Haynes, M., Stang, J., & Moghaddam, M. (2014). Real-time Microwave Imaging of Differential Temperature for Thermal Therapy Monitoring. *IEEE Transactions on Biomedical Engineering*, 61(6), 1787–1797.

[37] Hee, M. R., Izatt, J. A., Swanson, E. A., Huang, D., Schuman, J. S., Lin, C. P., Puliafito, C. A., & Fujimoto, J. G. (1995). Optical coherence tomography of the human retina. *Archives of ophthalmology*, 113(3), 325–332.

[38] Herovici, C. (1963). A polychrome stain for differentiating precollagen from collagen. *Stain technology*, 38, 204–206.

[39] Hill, D. L., Batchelor, P. G., Holden, M., & Hawkes, D. J. (2001). Medical image registration. *Physics in medicine and biology*, 46(3), R1.

[40] Jacques, S. L. (2006). Ratio of entropy to enthalpy in thermal transitions in biological tissues. *Journal of Biomedical Optics*, 11(4), 041108.

[41] Jun, C., Villiger, M., Oh, W.-Y., & Bouma, B. E. (2014). All-fiber wavelength swept ring laser based on fabry-perot filter for optical frequency domain imaging. *Optics express*, 22(21), 25805–25814.

[42] Junqueira, L. C. U., Bignolas, G., & Brentani, R. R. (1979). Picrosirius staining plus polarization microscopy, a specific method for collagen detection in tissue sections. *The Histochemical Journal*, 11(4), 447–455.

[43] Ke, H., Tai, S., & Wang, L. V. (2014). Photoacoustic thermography of tissue. *Journal of biomedical optics*, 19(2), 026003–026003.

[44] Khosla, A., Xiao, J., Torralba, A., & Oliva, A. (2012). Memorability of image regions. In *Advances in Neural Information Processing Systems* (pp. 305–313).

[45] Kim, K. H., Pierce, M. C., Maguluri, G., Park, B. H., Yoon, S. J., Lydon, M., Sheridan, R., & de Boer, J. F. (2012). In vivo imaging of human burn injuries with polarization-sensitive optical coherence tomography. *Journal of biomedical optics*, 17(6), 066012–066012.

[46] Konishi, K., Nakamoto, M., Kakeji, Y., Tanoue, K., Kawanaka, H., Yamaguchi, S., Ieiri, S., Sato, Y., Maehara, Y., Tamura, S., et al. (2007). A real-time navigation system for laparoscopic surgery based on three-dimensional ultrasound using magneto-optic hybrid tracking configuration. *International Journal of Computer Assisted Radiology and Surgery*, 2(1), 1–10.

[47] Krötzsch-Gómez, F. E., Furuzawa-Carballeda, J., Reyes-Márquez, R., Quiróz-Hernández, E., & de León, L. D. (1998). Cytokine Expression is Downregulated by Collagen-Polyvinylpyrrolidone in Hypertrophic Scars1. *Journal of Investigative Dermatology*, 111(5), 828–834.

[48] Kuo, Y.-R., Wu, W.-S., Jeng, S.-F., Huang, H.-C., Yang, K. D., Sacks, J. M., & Wang, F.-S. (2005). Activation of erk and p38 kinase mediated keloid fibroblast apoptosis after flashlamp pulsed-dye laser treatment. *Lasers in Surgery and Medicine*, 36(1), 31–37.

[49] Lazebnik, S., Schmid, C., & Ponce, J. (2006). Beyond bags of features: Spatial pyramid matching for recognizing natural scene categories. In *Computer Vision and Pattern Recognition, 2006 IEEE Computer Society Conference on*, volume 2 (pp. 2169–2178).: IEEE.

[50] Lillie, R. D., Tracy, D. R. E., Pizzolato, P., Donaldson, P. T., & Reynolds, C. (1980). Differential staining of collagen types in paraffin sections: A color change in degraded forms. *Virchows Archiv A*, 386(2), 153–159.

[51] Lowe, D. G. (1999). Object recognition from local scale-invariant features. In *Computer vision, 1999. The proceedings of the seventh IEEE international conference on*, volume 2 (pp. 1150–1157).: Ieee.

[52] Lucas, B. D. & Kanade, T. (1981). An iterative image registration technique with an application to stereo vision. In *Proceedings of the 7th International Joint Conference on Artificial Intelligence - Volume 2*, IJCAI'81 (pp. 674–679). San Francisco, CA, USA: Morgan Kaufmann Publishers Inc.

[53] Lyday, W. D., Corbett, F. S., Kuperman, D. A., Kalvaria, I., Mavrelis, P. G., Shughoury, A. B., Pruitt, R. E., Prevention, C., Therapy, N., & Hospital, S. M. (2009). Radiofrequency ablation of Barrett's esophagus : outcomes of 429 patients from a multicenter community practice registry. *Endoscopy*, 42(04), 272–278.

[54] Maes, F., Collignon, A., Vandermeulen, D., Marchal, G., & Suetens, P. (1997). Multimodality image registration by maximization of mutual information. *IEEE transactions on Medical Imaging*, 16(2), 187–198.

[55] Maintz, J. A. & Viergever, M. A. (1998). A survey of medical image registration. *Medical image analysis*, 2(1), 1–36.

[56] Maitland, D. J. & Walsh, J. T. (1997). Quantitative measurements of linear birefringence during heating of native collagen. *Lasers in surgery and medicine*, 20(3), 310–318.

[57] McNichols, R. J., Gowda, A., Kangasniemi, M., Bankson, J. A., Price, R. E., & Hazle, J. D. (2004). MR thermometry-based feedback control of laser interstitial thermal therapy at 980 nm. *Lasers in surgery and medicine*, 34(1), 48–55.

[58] Melodelima, D., Salomir, R., Chapelon, J. Y., Theillère, Y., Moonen, C., & Cathignol, D. (2005). Intraluminal high intensity ultrasound treatment in the esophagus under fast MR temperature mapping: In vivo studies. *Magnetic Resonance in Medicine*, 54(4), 975–982.

[59] Mogensen, M., Thrane, L., Jørgensen, T. M., Andersen, P. E., & Jemec, G. B. E. (2009). OCT imaging of skin cancer and other dermatological diseases. *Journal of Biophotonics*, 2(6-7), 442–451.

[60] Mountney, P., Stoyanov, D., Davison, A., & Yang, G.-Z. (2006). Simultaneous stereoscope localization and soft-tissue mapping for minimal invasive surgery. In *Medical Image Computing and Computer-Assisted Intervention–MICCAI 2006* (pp. 347–354). Springer.

[61] Nam, A. S., Chico-Calero, I., & Vakoc, B. J. (2014). Complex differential variance algorithm for optical coherence tomography angiography. *Biomedical optics express*, 5(11), 3822–3832.

[62] Neumann, R., Knobler, R., Pieczkowski, F., & Gebhart, W. (1991). Enzyme histochemical analysis of cell viability after argon laser-induced coagulation necrosis of the skin. *Journal of the American Academy of Dermatology*, 25(6), 991–998.

[63] Ozog, D. M., Liu, A., Chaffins, M. L., Ormsby, A. H., Fincher, E. F., Chipps, L. K., Mi, Q.-S., Grossman, P. H., Pui, J. C., & Moy, R. L. (2013). Evaluation of clinical results, histological architecture, and collagen expression following treatment of mature burn scars with a fractional carbon dioxide laser. *JAMA dermatology*, 149(1), 50–57.

[64] Park, B. H., Saxer, C., Srinivas, S. M., Nelson, J. S., & de Boer, J. F. (2001). In vivo burn depth determination by high-speed fiber-based polarization sensitive optical coherence tomography. *Journal of biomedical optics*, 6(4), 474–479.

[65] Pennes, H. H. (1948). Analysis of tissue and arterial blood temperatures in the resting human forearm. *Journal of applied physiology*, 1(2), 93–122.

[66] Pierce, M. C., Sheridan, R. L., Hyle Park, B., Cense, B., & De Boer, J. F. (2004a). Collagen denaturation can be quantified in burned human skin using polarization-sensitive optical coherence tomography. *Burns*, 30(6), 511–517.

[67] Pierce, M. C., Strasswimmer, J., Hyle Park, B., Cense, B., & de Boer, J. F. (2004b). Birefringence measurements in human skin using polarization-sensitive optical coherence tomography. *Journal of Biomedical Optics*, 9(2), 287–291.

[68] Pierce, M. C., Strasswimmer, J., Park, B. H., Cense, B., & de Boer, J. F. (2004c). Advances in optical coherence tomography imaging for dermatology. *Journal of investigative dermatology*, 123(3), 458–463.

[69] Pierce, M. C., Strasswimmer, J., Park, B. H., Cense, B., & de Boer, J. F. (2004d). Advances in Optical Coherence Tomography Imaging for Dermatology. *Journal of Investigative Dermatology*, 123(3), 458–463.

[70] Romero-Aroca, P., Reyes-Torres, J., Baget-Bernaldiz, M., & Blasco-Suñe, C. (2014). Laser treatment for diabetic macular edema in the 21st century. *Current diabetes reviews*, 10(2), 100–112.

[71] Sakai, S., Yamanari, M., Miyazawa, A., Matsumoto, M., Nakagawa, N., Sugawara, T., Kawabata, K., Yatagai, T., & Yasuno, Y. (2008). In vivo Three-Dimensional Birefringence Analysis Shows Collagen Differences between Young and Old Photo-Aged Human Skin. *Journal of Investigative Dermatology*, 128(7), 1641–1647.

[72] Schoenenberger, K., Colston, B. W., Maitland, D. J., Da Silva, L. B., & Everett, M. J. (1998). Mapping of birefringence and thermal damage in tissue by use of polarization-sensitive optical coherence tomography. *Applied Optics*, 37(25), 6026–6036.

[73] Seror, O., Lepetit-Coiffé, M., Le Bail, B., De Senneville, B. D., Trillaud, H., Moonen, C., & Quesson, B. (2008). Real time monitoring of radiofrequency ablation based on MR thermometry and thermal dose in the pig liver in vivo. *European radiology*, 18(2), 408–416.

[74] Shah, M., Foreman, D. M., & Ferguson, M. W. J. (1992). Control of scarring in adult wounds by neutralising antibody to transforming growth factor β. *The Lancet*, 339(8787), 213–214.

[75] Shaheen, N. J. & Frantz, D. J. (2010). When to consider endoscopic ablation therapy for barrett's esophagus. *Current opinion in gastroenterology*, 26(4), 361–366.

[76] Shaheen, N. J., Sharma, P., Overholt, B. F., Wolfsen, H. C., Sampliner, R. E., Wang, K. K., Galanko, J. A., Bronner, M. P., Goldblum, J. R., Bennett, A. E., Jobe, B. A., Eisen, G. M., Fennerty, M. B., Hunter, J. G., Fleischer, D. E., Sharma, V. K., Hawes, R. H., Hoffman, B. J., Rothstein, R. I., Gordon, S. R., Mashimo, H., Chang, K. J., Muthusamy, V. R., Edmundowicz, S. A., Spechler, S. J., Siddiqui, A. A., Souza, R. F., Infantolino, A., Falk, G. W., Kimmey, M. B., Madanick, R. D., Chak, A., & Lightdale, C. J. (2009). Radiofrequency ablation in Barrett's esophagus with dysplasia. *The New England Journal of Medicine*, 360(22), 2277–2288.

[77] Shemonski, N. D., Ahn, S. S., Liu, Y.-Z., South, F. A., Carney, P. S., & Boppart, S. A. (2014). Three-dimensional motion correction using speckle and phase for in vivo computed optical interferometric tomography. *Biomedical optics express*, 5(12), 4131–4143.

[78] Suter, M. J., Gora, M. J., Lauwers, G. Y., Arnason, T., Sauk, J., Gallagher, K. A., Kava, L., Tan, K. M., Soomro, A. R., Gallagher, T. P., Gardecki, J. A., Bouma, B. E., Rosenberg, M., Nishioka, N. S., & Tearney, G. J. (2014). Esophageal-guided biopsy with volumetric laser endomicroscopy and laser cautery marking: a pilot clinical study. *Gastrointestinal Endoscopy*, 79(6), 886–896.

[79] Suter, M. J., Jillella, P. A., Vakoc, B. J., Halpern, E. F., Mino-Kenudson, M., Lauwers, G. Y., Bouma, B. E., Nishioka, N. S., & Tearney, G. J. (2010). Image-guided biopsy in the esophagus through comprehensive optical frequency domain imaging and laser marking: a study in living swine. *Gastrointestinal Endoscopy*, 71(2), 346–353.

[80] Suter, M. J., Vakoc, B. J., Yachimski, P. S., Shishkov, M., Lauwers, G. Y., Mino-Kenudson, M., Bouma, B. E., Nishioka, N. S., & Tearney, G. J. (2008). Comprehensive microscopy of the esophagus in human patients with optical frequency domain imaging. *Gastrointestinal Endoscopy*, 68(4), 745–753.

[81] Thomsen, S., Pearce, J. A., & Cheong, W.-F. (1989). Changes in birefringence as markers of thermal damage in tissues. *IEEE transactions on biomedical engineering*, 36(12), 1174–1179.

[82] Trujillo, M. & Berjano, E. (2013). Review of the mathematical functions used to model the temperature dependence of electrical and thermal conductivities of biological tissue in radiofrequency ablation. *International journal of hyperthermia*, 6736(6), 1–8.

[83] Tsai, T.-H., Lee, H.-C., Ahsen, O. O., Liang, K., Giacomelli, M. G., Potsaid, B. M., Tao, Y. K., Jayaraman, V., Figueiredo, M., Huang, Q., Cable, A. E., Fujimoto, J., & Mashimo, H. (2014). Ultrahigh speed endoscopic optical coherence tomography for gastroenterology. *Biomedical Optics Express*, 5(12), 4387.

[84] Turner, N. J., Pezzone, M. A., Brown, B. N., & Badylak, S. F. (2013). Quantitative multispectral imaging of Herovici's polychrome for the assessment of collagen content and tissue remodelling. *Journal of Tissue Engineering and Regenerative Medicine*, 7(2), 139–148.

[85] Uribe-Patarroyo, N. & Bouma, B. E. (2015). Rotational distortion correction in endoscopic optical coherence tomography based on speckle decorrelation. *Optics Letters*, 40(23), 5518.

[86] Urioste, S., Arndt, K., & Dover, J. (1999). Keloids and hypertrophic scars: review and treatment strategies. *Seminars in cutaneous medicine and surgery*, 18(2), 159.

[87] Vakoc, B. J., Shishko, M., Yun, S. H., Oh, W. Y., Suter, M. J., Desjardins, A. E., Evans, J. a., Nishioka, N. S., Tearney, G. J., & Bouma, B. E. (2007a). Comprehensive esophageal microscopy by using optical frequency-domain imaging (with video). *Gastrointestinal Endoscopy*, 65(6), 898–905.

[88] Vakoc, B. J., Tearney, G. J., & Bouma, B. E. (2007b). Real-time microscopic visualization of tissue response to laser thermal therapy. *Journal of Biomedical Optics*, 12(2), 020501–020501.

[89] Vedaldi, A. & Fulkerson, B. (2010). VLFeat: An open and portable library of computer vision algorithms. In *Proceedings of the international conference on Multimedia* (pp. 1469–1472).: ACM.

[90] Villiger, M., Soroka, A., Tearney, G. J., Bouma, B. E., & Vakoc, B. J. (2011). Injury depth control from combined wavelength and power tuning in scanned beam laser thermal therapy. *Journal of biomedical optics*, 16(11), 118001–1180019.

[91] Villiger, M., Zhang, E. Z., Nadkarni, S. K., Oh, W.-Y., Vakoc, B. J., & Bouma, B. E. (2013). Spectral binning for mitigation of polarization mode dispersion artifacts in catheter-based optical frequency domain imaging. *Optics Express*, 21(14), 16353–16369.

[92] Vogler, N., Medyukhina, A., Latka, I., Kemper, S., Böhm, M., Dietzek, B., & Popp, J. (2011). Towards multimodal nonlinear optical tomography - experimental methodology. *Laser Physics Letters*, 8(8), 617–624.

[93] Wang, J., Yang, J., Yu, K., Lv, F., Huang, T., & Gong, Y. (2010). Locality-constrained linear coding for image classification. In *Computer Vision and Pattern Recognition (CVPR), 2010 IEEE Conference on* (pp. 3360–3367).: IEEE.

[94] Wang, K. K. & Sampliner, R. E. (2008). Updated guidelines 2008 for the diagnosis, surveillance and therapy of barrett's esophagus. *The American journal of gastroenterology*, 103(3), 788.

[95] Williams, D., Sahai, A., Aabakken, L., Penman, I., Van Velse, A., Webb, J., Wilson, M., Hoffman, B., & Hawes, R. (1999). Endoscopic ultrasound guided fine needle aspiration biopsy: a large single centre experience. *Gut*, 44(5), 720–726.

[96] Wolfram, D., Tzankov, A., Pülzl, P., & Piza-Katzer, H. (2009). Hypertrophic scars and keloids - A review of their pathophysiology, risk factors, and therapeutic management. *Dermatologic Surgery*, 35(2), 171–181.

[97] Xu, N., Yao, M., Farinelli, W., Hajjarian, Z., Wang, Y., Redmond, R. W., & Kochevar, I. E. (2015). Light-activated sealing of skin wounds. *Lasers in surgery and medicine*, 47(1), 17–29.

[98] Yang, S. Y., O'Cearbhaill, E. D., Sisk, G. C., Park, K. M., Cho, W. K., Villiger, M., Bouma, B. E., Pomahac, B., & Karp, J. M. (2013). A bio-inspired swellable microneedle adhesive for mechanical interlocking with tissue. *Nature communications*, 4, 1702.

[99] Yang, V. X., Gordon, M. L., Mok, A., Zhao, Y., Chen, Z., Cobbold, R. S., Wilson, B. C., & Vitkin, I. A. (2002). Improved phase-resolved optical doppler tomography using the kasai velocity estimator and histogram segmentation. *Optics Communications*, 208(4), 209–214.

[100] Yun, S., Tearney, G., de Boer, J., & Bouma, B. (2004). Removing the depth-degeneracy in optical frequency domain imaging with frequency shifting. *Optics Express*, 12(20), 4822–4828.

[101] Zhou, C., Tsai, T.-H., Lee, H.-C., Kirtane, T., Figueiredo, M., Tao, Y. K., Ahsen, O. O., Adler, D. C., Schmitt, J. M., Huang, Q., et al. (2012). Characterization of buried glands before and after radiofrequency ablation by using 3-dimensional optical coherence tomography (with videos). *Gastrointestinal endoscopy*, 76(1), 32–40.